Lu-177 Automated Quantification Capabilities of Siemens Symbia Intevo 16.

Lucy Joy Grigoroff

School of Physical Sciences

Master of Philosophy (Science)

University of Adelaide

July 2022

Table of Contents

Abstract

The use of Lu-177 to treat metastatic prostate cancer and neuroendocrine tumours was introduced to Sir Charles Gairdner Hospital (SCGH) in 2018. Along with its introduction came an interest in dosimetry using absolute quantification. The installation of a new SPECT/CT (Siemens Symbia Intevo) with automated quantification abilities for Lu-177 required investigation into the scope of its capabilities and comparison to manual quantification. While there are studies on automated quantification of Tc-99m, there is little on Lu-177. The aim was to determine which of automated and manual quantification is more accurate when considering Lu-177 in a clinical context as well as the optimal measurement conditions in a clinical context. To cover a wide clinically applicable patient uptake range, a NEMA phantom study was designed.

Prior to the phantom study, the accuracy of the dose calibrator and deadtime effects were addressed. Optimal measurement conditions for Lu-177 in a vial and syringe were determined; both are clinically relevant and applied to this study. The Lu-177 manufacturers' activity was used for comparison since their equipment is officially calibrated more frequently. No correction factor was necessary and approximately 10 cm from the base of the well was the optimal position for both vial and syringe measurements.

Deadtime effects are isotope, collimator and camera specific and can have a profound impact on quantification results. Traditional methods to determine deadtime effects were unsuitable due to the relatively long half-life of Lu-177. A new intrinsic method using multiple small sources of Lu-177 in the middle of the FOV facilitated collection of a large volume of data in a shorter period of time. A count rate threshold for deadtime was determined and applied to the extrinsically acquired phantom data. It was determined that no deadtime correction was necessary for this study.

Blood concentration and tumour/organ uptake were used as phantom study design guidelines. A literature review of blood concentration and tumour/organ uptake from 24 hours post therapy onwards was considered in the design. This is the earliest clinically applicable scan for patients at SCGH. Blood concentration was represented by phantom background activity concentration and tumour/organs by fillable spheres. Phantom acquisition occurred once per day for 20 days with the background concentration manually altered to create a range of background to sphere ratios. A clinically based scan protocol with MELP collimators, 208 keV photopeak and Triple Energy Window scatter correction was applied. Dual reconstruction, labelled XSPECT and 3D Flash for automated and manual quantification respectively, were used. Automated and manual quantification results were collected in Siemens software Syngo.Via using auto-contouring tool labelled Response Evaluation Criteria in Solid Tumors (RECIST). Data was collected using RECIST 10, 20, 30 and 40% thresholds of the maximum counts, with and without recovery coefficients for partial volume correction.

Automated XSPECT quantification improved accuracy compared to manual 3D Flash quantification. A 30% RECIST threshold without partial volume correction were the optimal measurement conditions, differing from the current clinical standard of 40% when considering Lu-177.

Declaration

I certify that this work contains no material which has been accepted for the award of any other degree or diploma in my name, in any university or other tertiary institution and, to the best of my knowledge and belief, contains no material previously published or written by another person, except where due reference has been made in the text. In addition, I certify that no part of this work will, in the future, be used in a submission in my name, for any other degree or diploma in any university or other tertiary institution without the prior approval of the University of Adelaide and where applicable, any partner institution responsible for the joint award of this degree.

I give permission for the digital version of my thesis to be made available on the web, via the University's digital research repository, the Library Search and also through web search engines, unless permission has been granted by the University to restrict access for a period of time.

I acknowledge the support I have received for my research through the provision of an Australian Government Research Training Program Scholarship.

Lucy Grigoroff

27/07/2022

Acknowledgments

I would like to acknowledge my University of Adelaide Supervisor Judith Pollard for her guidance and insight throughout this process. I acknowledge Alexander Santos for his assistance in procuring funding for the purchase of Lutetium-177.

I would also like to acknowledge my external supervisor Cameron Storm for his guidance, advice and encouragement throughout this process. Thank you for keeping me sane. I thank my advisor Steven Crossley for all his expert Nuclear Medicine knowledge and making the time to brainstorm and answer all my questions from using software and machines to forming new methodology. I thank Joe Ioppolo for his proof reading and willingness to assist me.

I acknowledge the Team in Nuclear Medicine at Sir Charles Gairdner Hospital. Without their cooperation and the use of their phantom, scanner and lab this project would not have been possible.

Glossary

Term	Definition
ANSTO	Australian Nuclear Science and Technology Organisation
AAPM	American Association of Physicists in Medicine
CF	Calibration Factor
CR	Count Rate
CT	Computed Tomography
DEW	Double Energy Window
DTC	Dead Time Correction
FOV	Field of View
FSH	Fiona Stanley Hospital
GEP	Gastroenteropancreatic
GMS	Global Medical Solutions
IEC	International Electrotechnical Commission
IQR	Interquartile Range
LEHR	Low-Energy High-Resolution
LINAC	Linear Accelerator
Lu-177	Lutetium isotope 177
LW	Lower Window
mCRPC	Metastatic Castration Resistant Prostate Cancer
MELP	Medium-Energy Low-Penetration
MIM	Medical Image Merge
MIRD	Medical Internal Radiation Dose
NEMA	National Electrical Manufacturers Association
NET	Neuroendocrine Tumour
NIST	National Institute of Standards and Technology
NM	Nuclear Medicine
OAR	Organ at Risk
PET	Positron Emission Tomography
PMT	Photomultiplier Tube
PSMA	Prostate Specific Membrane Antigen
PVC	Partial Volume Correction
PVE	Partial Volume Effect
PW	Peak Window
RC	Recovery Coefficient
RECIST	Response Evaluation Criteria in Solid Tumours
RMSE	Root Mean Square Error
ROI	Region of Interest
SCGH	Sir Charles Gairdner Hospital
SA	Surface Area
SD	Standard Deviation
SPECT	Single-Photon Emission Computed Tomography
SRM	Standard Reference Materials
SSTR	Somatostatin Receptors
TEW	Triple Energy Window
UW	Upper Window
VOI	Volume of Interest

XSPECT quant	Automated absolute quantification capability of the Siemens Symbia Intevo SPECT/CT

1 Introduction

Lutetium-177 (Lu-177) is an isotope with increasing use in therapy (Bailey et al. 2015b). It offers not only a therapeutic effect, it also has imaging capability that can be used to measure the uptake of the therapy. Lu-177 has multiple properties that make it suitable for therapy and imaging.

It emits high energy beta particles with an $E_{\beta\,max}$ = 497 keV (78.6 %), 384 keV (9.1 %) and 176 keV (12.2 %) (Talukdar, Dewhirst & Paulsen 2019). The average penetration range of the beta particles in soft tissue is 670 µm, making this radionuclide ideal for delivering energy to small volumes, including micro metastatic disease (Dash, Pillai & Knapp 2015). Its gamma photons have E_{γ} = 208 keV (11.1%) and 113 keV (6.6%), both of which can be utilised for diagnostic imaging in SPECT. Its half-life of 6.7 days facilitates longer delivery of its therapeutic effect to targeted tissue while allowing functional imaging, and so tracking, many days post therapy (Bailey et al. 2015b).

More specifically, Lu-177 has been used to treat Neuroendocrine Tumours (NETs), and more recently metastatic prostate cancer. Both use proteins that seek out receptors that are overexpressed by tumours, which may then internalise the lutetium complex, allowing the Lu-177 to enact its therapeutic effect. This selective delivery allows targeting of widespread tumours in a single treatment while sparing other tissue. Just as is the case with external beam radiation with a linear accelerator (LINAC), maximising dose to tumours, while minimising dose to normal tissue, is the ultimate aim. Unlike therapies such as external beam radiation, the target tissue is irradiated from the inside out and the beta radiation is short range and so better confined to the desired target. While there are some organs at risk (OARs, further discussed in chapter 4), they are either protected through other means and/or the applied therapies are still more specifically targeted than certain forms of chemotherapy that target all rapidly proliferating cells. At Sir Charles Gairdner Hospital (SCGH), Lu-177 therapy is delivered intravenously at regular intervals of 6 to 8 weeks for metastatic prostate cancer and 8 to 12 weeks for NETs. This continues for up to 6 cycles for metastatic prostate and 4 for NETs, so long as patients tolerate the treatment and receive the desired effect. Patients may complete the full course of treatment and be re-treated later on with the same therapy under the same provisos.

Prostate specific membrane antigen (PSMA) shows intense overexpression in the majority of prostate cancers. This makes PSMA targeting ligands, such as PSMA-617, ideal molecules for delivering Lu-177 to prostate cancer (Kratochwil et al. 2015). In Australia, prostate cancer is the second most common diagnosed cancer and third most common cause of cancer death. By age 85, 1 in 6 men are diagnosed and over 63% of diagnosed cases present in men over 65 years of age (CancerCouncilAustralia 2020). With such high incidence in the population, many trials using Lu-177 have been conducted, including *ENZA-p* (Emmett et al. 2021), *UpFront* (Dhiantravan et al. 2021) and *TheraP* (Hofman et al. 2019) that Sir Charles Gairdner has participated in. The therapy has also been used extensively for separate clinical patients since 2018.

While not as prevalent, metastatic NETs have also been treated using Lu-177. NETs, particularly gastroenteropancreatic (GEP) NETs, over-express somatostatin receptors (SSTRs) on their cell surface. There are 5 subtypes labelled SSTR1-5, of which the membrane bound SSTR2 prevails (Kwekkeboom, D. J., de Herder & van Eijck 2010). Octreotide is a synthetic peptide which mimics somatostatin pharmacologically and has a high affinity for SSTR2. Octreotate is a derivative of octreotide incorporating the DOTA macrocycle for complexing radiometals like Lu-177. GEPs are not the only type of tumour that overexpress SSTRs.

Meningiomas are brain tumours that often recur. A study from Silva et al. (2015) investigated expression of SSTRs in meningiomas. It showed in vitro and in vivo that meningiomas, regardless of histology and classification, express somatostatin receptors (SSTRs). A review paper by Zhao et al. (2018) revealed the crucial clinical significance of overexpression of SSTR2 in meningiomas, making Lu-177-octreotate a possible treatment option. Notably different to GEPs, this treatment has been delivered intra-arterially, as opposed to venously, in some cases. The same intra-arterial administration has been applied for liver NET metastasis in a study by Ebbers et al. (2020). This approach to the liver, is meant to treat one lobe intra-arterially (the "first-pass" effect), while the contralateral lobe will receive an intravenous treatment as a second-pass effect. The first pass effect is also desired for the meningioma and was applied in a case study by Braat et al. (2019). The patient displayed greatly increased uptake with intra-arterial versus intravenous administration. The patient had their first round of treatment intravenously and the subsequent 3 arterially so there was a small but direct comparison. As of early 2022, three patients have received intra-arterial Lu-177-octreotate for meningiomas at SCGH.

With the large Lu-177 patient volume at SCGH and the aim of having increased uptake for specific and complicated cases, absolute quantification is of interest as it plays an essential role in dosimetry.

Dosimetry plays an important role in radiopharmaceutical therapy. Estimates of activity are necessary for tumour and healthy tissue doses and the two may be weighed against each other. The MIRD (Medical Internal Radiation Dose) committee formalism relevant to therapy (rather than diagnostic scans) is **Equation 1-1**.

$$D(r_T, T_S) = \sum_{r_s} \tilde{A}(r_s, T_S)\, S(r_\tau \leftarrow r_s)$$

Equation 1-1

where $D(r_\tau, T_S)$ is the dose to a target organ or tissue, r_τ, during a defined dose integration period T_S, $\tilde{A}(r_s, T_S)$ is the time-integrated activity (or total number of disintegrations) in the source organ or tissue r_s during T_S and $S(r_\tau \leftarrow r_s)$ are S factors, which give the absorbed dose in the target per disintegration in each source organ (Bushberg 2012). The calculations are more involved, with complex time-activity curves and more widespread distribution of the radiopharmaceutical among different organs, but the simplified version in **Equation 1-1** allows a simple introduction of the importance of quantification.

To create a time integrated activity curve, a patient is imaged multiple times post therapy and the activity quantified in its various locations. Accurately determining the quantity of activity has been a subject of recent interest when considering SPECT.

For isotopes such as Lu-177, imaging is performed with a SPECT/CT hybrid scanner. Nuclear Medicine imaging studies have historically relied on qualitative assessment. The majority of clinical SPECT studies are not aimed at accurately quantifying activity distribution. Count rates of the gamma rays are recorded by the detector but not converted to absolute values of radioactivity concentration such as kilobequerels per millilitre (kBq/ml). This is changing, facilitated by improvements to reconstruction algorithms, attenuation and scatter corrections (Bailey et al. 2015b). Manufacturers of SPECT/CTs such as Siemens and GE have developed software for quantification calculations.

> "In June 2013, Siemens Healthineers Molecular Imaging (MI) introduced Symbia Intevo™ SPECT/CT and with it, xSPECT Quant, the first and only solution capable of delivering absolute quantification-paving the way for accurate, reproducible, and standardized quantitative clinical studies." (Vija, A, Von Gall, C & Ghosh, P 2018)

SCGH purchased and installed one such SPECT/CT in 2018, the Symbia Intevo, that has XSPECT quant as a feature.

Traditionally, a conversion method to change counts to Bq/ml is applied, such as a basic calibration factor post-reconstruction. A known source, measured in a reference device (dose calibrator), would be acquired in a phantom using the SPECT with the same protocol and reconstruction to determine the calibration factor. The assumption is that the calibration factor can be applied to patient scan data. Methods that rely on dose calibrators are limited to being as precise and accurate as the dose calibrator is. This has potential, and it may work well for a single site with a certain protocol. The bias in the dose calibrator is not relevant so long as the same one is used to determine the calibration factor and injected dose. However, this is difficult to apply to multiple sites as their dose calibrators will vary. If the desire is to assess a patient over a long period of time, compare between sites or to perform internal dosimetry estimations, a reference standard with small variability that allows for reliable measurements of absolute activity distribution in vivo is required.

Siemens XSPECT quant uses National Institute of Standards and Technology (NIST)- traceable sources to achieve accurate and reproducible quantification. This calibrated sensitivity source was intended to standardize the system sensitivity to allow quantitative results to be comparable across systems and time. The sensitivity sources are either Cobalt-57 (Co-57, for low energy) or Selenium-75 (Se-75, for medium energy), and both have NIST-traceable activity that deviates less than 3% from the known manufactured strength. These sources are used in a reproducible position in the field of view (FOV) once a month, to calibrate system-specific sensitivity variation. This is done using a dose probe that extends from the bed, as seen in **Figure 3-5A**. XSPECT is designed to estimate the activity concentration as part of the reconstruction, giving the image results in units of Bq/ml. The NIST-traceable source is suggested to be placed in the dose calibrator with reproducible geometry to allow for a cross-check between the system, dose calibrator and NIST-traceable source (Vija, A, Von Gall, C & Ghosh, P 2018). The calibration and reconstruction software for XSPECT attempts to correct for any non-uniformities caused by the variation in geometry and performance of each camera head, including the collimators used, and so corrections are specific to a particular system and collimator combination. Siemens also notes that conversion factors and dead time needs to be measured on site and are only valid on that machine.

Due to the role of the dose calibrator (well counter) in traditional quantification and its suggested use for XSPECT, conditions for its optimal accuracy are addressed in chapter 2. Additionally, Siemens guideline that deadtime is site and camera specific is addressed in chapter 3.

Following the hospital's purchase of the SPECT/CT with the XSPECT quant feature, this study was designed to compare traditional quantification methodology to XSPECT quant, specifically for Lu-177 with a range of clinically relevant activities. Current studies of Lu-177 quantification such as those listed in **Table 1-1** have used phantom studies to assess accuracy and precision, but for specific background to object ratios. If they do consider various ratios, they vary the objects of interest, rather than the background and only investigate the traditional form of quantification.

Table 1-1 *Phantom quantification studies of Lu-177 (Beauregard et al. 2011; de Nijs et al. 2014; Frezza et al. 2020; Hippeläinen et al. 2016; Johannes & Michael 2018; Marin et al. 2017; Peters et al. 2020; Sanders et al. 2014; Uribe, Esquinas & Tanguay 2017; Zhao et al. 2018).*

References	Phantom	Ratio	Total Activity	Quantification	Centers
Peters et al.	Modified cylindrical Jaszczak phantom	10:1	120 MBq	Automated +Traditional	4
Marin et al.	NEMA 2012/IEC 2008 phantom	5:1	7040-0.6 MBq	Traditional	1
Uribe, Esquinas & Tanguay	Eight phantoms containing inserts of different sizes and shapes placed in air, water, and radioactive background		1183-1.7 MBq 0.49 ± 0.03 MBq/ml background	Traditional	1
Beauregard et al.	Source without surrounding medium, source with surrounding medium of polystyrene containing 8 one-liter saline bags, Perspex cylindrical phantom with 3 cylindrical inserts.		90-12400 MBq	Traditional	1
de Nijs et al.	NEMA 2007/IEC2008 phantom	13:1	1.31 MBq/ml spheres	Traditional	1
Sanders et al.	Cylinder (6.2 L) uniformly filled with activity containing small spheres (0.5–16 ml)	8:1	307.5 MBq	Traditional	1
Hippeläinen et al.	Spheres (0.4-104.4 ml) in a torso phantom.	30:1	0.5-105.5 MBq	Traditional	1
Zhao et al.	Small containers in the large cylinder filled, in cold and hot background then large cylinders with no inserts, filled uniformly with activity.		11.7-2460 MBq	Traditional	1
Frezza et al.	1. Capillary tubes on a polystyrene foam board (minimal attenuation, thus considered “air equivalent”) 2. A cylindrical piece of polystyrene foam with nine holes with capillary tubes 3. Three polymethylmethacrylate cylindrical phantoms (diameters of 10, 16 and 32 cm, respectively), each with five holes for capillary tubes. 4. Jaszczak		Jaszczak; 18,535 MBq in background, 574 MBq in Spheres.	Traditional	1
Johannes & Michael	2-compartment kidney phantom, a sphere, and an ellipsoid of equal volumes all 3D printed.		2-compartment kidney 1.25 MBq/mL	Automated + Traditional	1

Additionally, each study in **Table 1-1** has different scatter corrections, reconstructions and various other corrections (such as that for deadtime) with SPECT/CTs from various manufacturers. For this reason, as well as site-specific differences in equipment and scan protocol, the phantom study in chapter 4 was designed. The goal of this study was to assess the accuracy of the automated quantification provided by Siemens, specifically in its application to Lu-177 in a clinical context and compare that to traditional quantification methods. The impact of the well counter accuracy and deadtime effects were isolated and considered prior to the phantom study.

2 Well counter

2.1 Background

The Nuclear Medicine Department in SCGH uses an AtomLab 500 from Biodex to calibrate radioisotopes. The chamber is an argon gas filled pressurized detector and activity is measured by a microprocessor-controlled electrometer in the chamber assembly. There is 6.3 mm of lead shielding on all sides and the bottom of the detector (Biodex Medical Systems 2016). This helps shield the user and prevent interference from surrounding sources found in a Nuclear Medicine facility. In order to prevent contamination to the well center, a removable plastic tube lines the detector. This set up, depicted in **Figure 2-1**, facilitates a measuring geometry close to 4π which would completely surround the source (SA = $4\pi r^2$ being the surface area of a sphere of radius r).

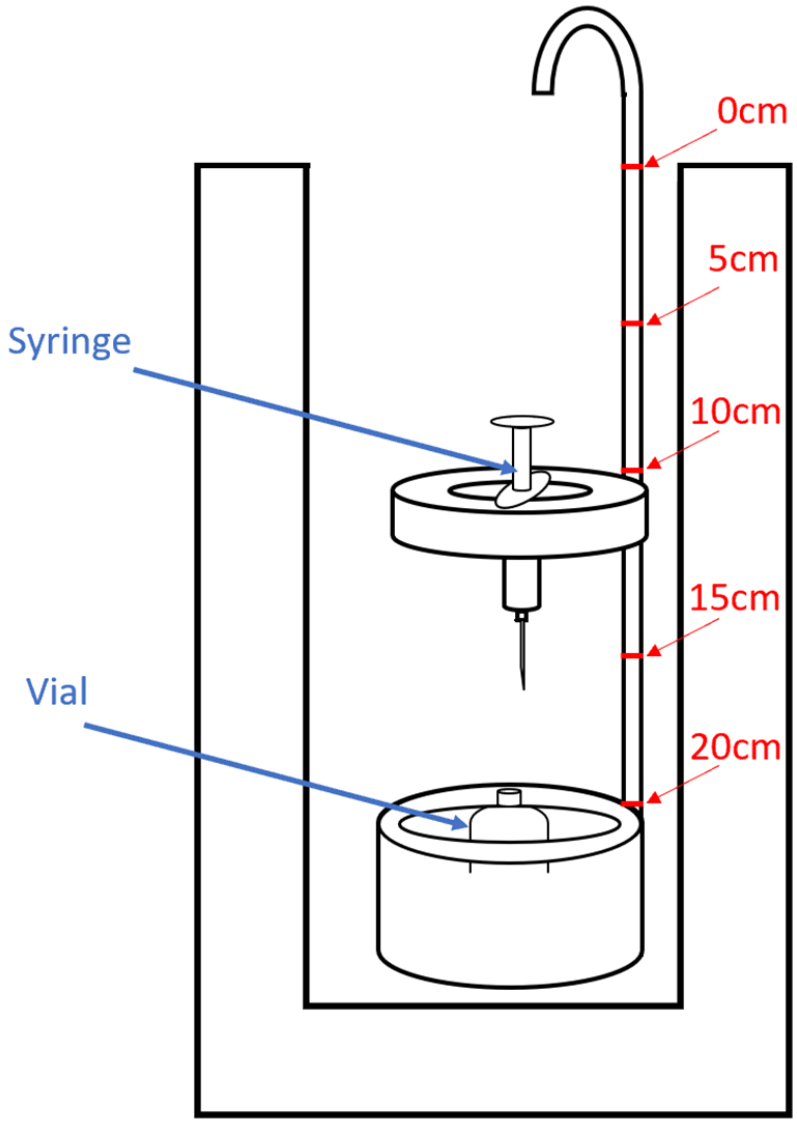

Figure 2-1 *Atomlab well counter set up with vial and syringe. The markings, when lined up with the top of the well counter, indicate how raised from the bottom the dipper is.*

All radioactive sources are inherently 4π, emitting radiation in all directions. Complete 4π measuring geometry allows activity measurement no matter the volume or shape of the source (S.E. International 2019). The detector depicted in **Figure 2-1** cannot intercept all radiation due to the opening of the well and its finite stopping power.

The SRM (Standard Reference Materials) program at the NIST (National Institute of Standards and Technology) provides a source of well-characterized materials certified for chemical composition or for some chemical or physical property. These materials are designated Standard Reference Materials (SRMs), and are used to calibrate measuring instruments.

NIST radioactivity SRMs represent the US national basis for accurate radioactivity measurements which is also utilised in Australia. Calibration factors for many radionuclides were established and retained on a stable and accurate ionization chamber at NIST. The response from argon gas filled pressurized detector ionisation chambers has been studied using such SRMs. The detector in Nuclear Medicine at SCGH was also calibrated with SRMs at NIST ((NIST) 2018).

The accuracy of the correction factors developed from NIST calibration, named Dial Values, depends on the accuracy of the sensitivity curve, the photon emission intensity data and sample configuration (Biodex Medical Systems 2016).

2.1.1 Sensitivity curve

The sensitivity of the Atomlab 500 detector as a function of photon energy is shown in **Figure 2-2,** which is from the manufacturer and was produced from measurements at multiple energies conducted at the NIST, combined with Monte Carlo modeling of the ion detector. The Monte Carlo simulation allowed improved interpolation to better determine the shape of the sensitivity curve between measured data points. The manufacturer used NIST calibrated isotopes of a multitude of photon energies were used for measurements to create **Figure 2-2**. Ga-67, Tc-99m, Mo-99, In-111, I-125, I-131, Xe-133, and TI-201 were provided from the NIST SRM program. All of these were 5 ml solutions (apart from Xe-133 being mixed with non-radioactive xenon gas) in sealed borosilicate glass ampoules. In addition to these, NIST traceable sources of the isotopes F-18, Co-57, Co-60, Ba-133, and Cs-137 were measured. The F-18 source was measured in a 10 ml BD plastic syringe while Co-57, Co-60, Ba-133, and Cs-137 sources were contained within epoxy sealed Type E-vials. Yearly calibration with NIST traceable Co-60, Ba-133, Co-57, and Cs-137 sources also occurs (Biodex Medical Systems 2016).

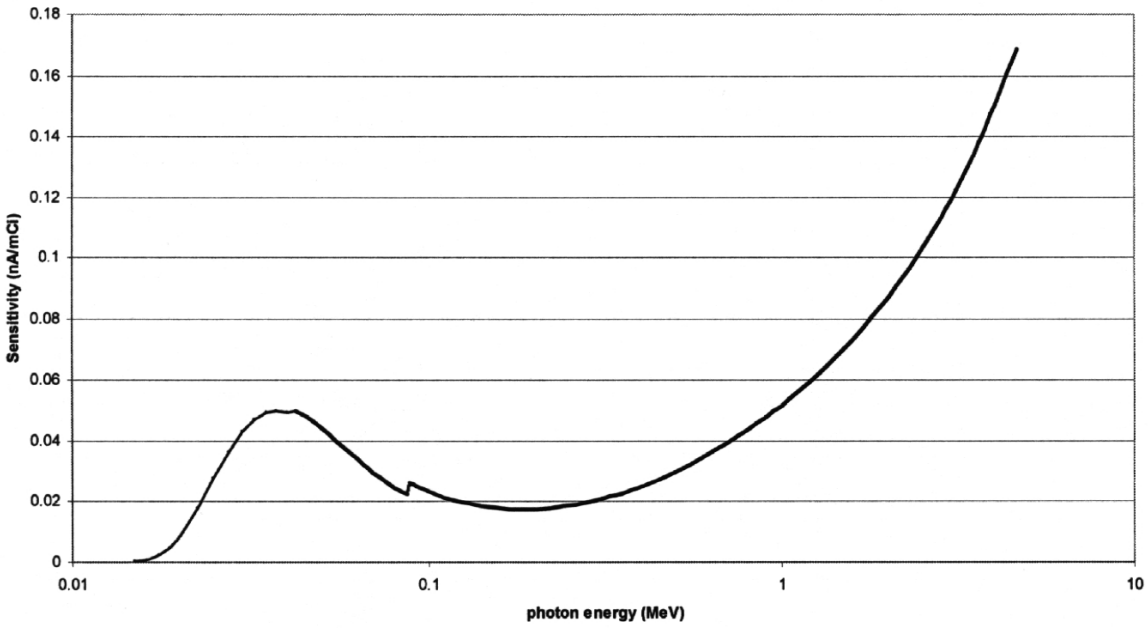

Figure 2-2 *Atomlab Photon Sensitivity Curve. The first peak at 88-200 keV range is due to back scatter from the lead shielding (Biodex Medical Systems 2016).*

Figure 2-2 is intended for sources with configurations similar to those NIST provided and this study used two different configurations that are used clinically (neither identical to NIST). To calculate doses for patients, a vial is measured before and after activity is drawn out and the calculated difference is the administered activity. Once the therapy has been administered, the syringe is measured for the residual. As Lutetium is a beta emitter, and not one of the NIST traceable sources used for calibration, measurements were more likely to be affected by change in container geometry (Biodex Medical Systems 2016). This is due to the short range of beta particles which affects the impact of self-shielding on measurements. For these reasons as well as the role of the dose calibrator discussed in the introduction chapter 1, conditions for optimal accuracy were determined (Biodex Medical Systems 2016).

2.1.2 Dial Values

The optimal measuring conditions gave consideration to the Isotope, container geometry and volume dependence. The Dial Value was initially tailored to Lu-177 upon introduction of its use at SCGH.

Dial Values (DV) are measurement calibration factors specific to each isotope necessary due to the different detector current each isotope produces. Detector response for a given isotope is defined as the amount of detector current produced by a given amount of Isotope activity, calculated using **Equation 2-1**.

$$R_{isotope} = \frac{Chamber\ current}{Isotope\ Activity}$$

Equation 2-1

where $R_{isotope}$ is the detector response for a specific isotope.

The current (detector response) produced from a Co-60 source is prescribed a nominal Dial Value of 5; all other isotopes are defined relative to this. DV for other isotopes is defined by **Equation 2-2**.

$$DV_{isotope} = 5 \times \frac{R_{Co-60}}{R_{isotope}}$$

Equation 2-2

where $R_{Co\text{-}60}$ is the detector response from a Co-60 source. Co-60 is the reference isotope due to its high energy photon emissions and a long half-life. Using high energy photons reduces the effect of container geometry, another reason more consideration was given to Lu-177 since it has lower energy and less abundant photon emissions (Biodex Medical Systems 2016).

The response of the detector can be calculated via **Equation 2-3**.

$$R_{isotope} = \sum_{e} S_e I_e$$

Equation 2-3

where I_e is the intensity of the photons of energy e and S_e is the sensitivity of the detector to photons of energy e in in nA/Bq given by **Equation 2-4**.

$$S_e = \frac{\text{Chamber current (nA)}}{A(\text{Bq}) \times \gamma_e}$$

Equation 2-4

where γ_e is the number of photons of energy *e* per disintegration and *A*(Bq) is the activity, or the number of disintegrations per second in Becquerels.

Adjustments to Dial Values are made using a sample of known activity to calibrate against using **Equation 2-5**.

$$CDV = \frac{DV \times A_{Syr}}{A_{fc} \times A_{ec}}$$

Equation 2-5

where *CDV* is Container Dial Value, *DV* is the current Dial Value, A_{fc} is the activity of the filled container under investigation, A_{ec} is the residual activity in this container when empty and A_{Syr} is the Syringe activity in a plastic syringe with nominal wall thickness 1mm.

Importantly for beta emitters, Dial Values should also be specific to container geometry. This has been done for Y-90, with specific Dial Values for vials and syringes, but was not previously performed for Lu-177 at SCGH.

Additionally, volume dependence (the effect of self-shielding), should be considered. The AtomLab had been tested for volume dependence for other beta emitters using Y-90, a worst case scenario being a pure beta emitter, and an error of 0.13%/ml was found (Biodex Medical Systems 2016). Again, this had not been investigated for Lu-177.

The aim of this experiment was to re-validate the Dial Value for Lu-177, find optimal measuring conditions for vial and syringe geometry and determine the effect of volume dependance.

2.2 Vial geometry

2.2.1 Vial Geometry Methods

Optimal measurement conditions were first established for vial geometry. Calibrated glass vials of Lu-177 were provided by ANSTO for labelling with the appropriate complexes for therapies on site at SCGH (PSMA or octreotate). ANSTO's calibration was used as the known activity for comparison with the well counter as their equipment is more regularly calibrated. While the Nuclear Medicine department performs a daily consistency check using Co-57, in addition to the more thorough and comprehensive annual calibration, ANSTO has their equipment thoroughly calibrated quarterly.

Four different vials, prior to preparation as a radiopharmaceutical, were measured. Each vial contained approximately 10 GBq and was placed in a dipper, as shown in **Figure 2-1**. It was important that the dose be unaltered (pre-labelling) so calibration could be compared to that from the manufacturer. Transfer between containers and the labelling process leave behind residual, altering the activity.

Results were time corrected to the same time as ANSTOs calibration using **Equation 2-6**.

$$A = A_0 e^{\frac{-ln2}{T_{\frac{1}{2}}}(t_m - t_0)}$$

Equation 2-6

where A is the Actual activity at time of measurement t_m, A_0 is the Stated activity at time t_0, $T_{1/2}$ is the Lu-177 half-life of 6.64 ± 0.01 days, and t_0 is the ANSTO calibrated time.

To determine the most effective conditions, each vial was measured at 0, 5, 10, 15 and 20 cm from the bottom of the well. The dipper was placed in the well and marked where it met with the top of the well counter. Marks were placed at 5 cm intervals from this first mark to denote the distance from the bottom of the dipper to the bottom of the well counter as shown in **Figure 2-1**.

A measurement was taken at each height as depicted in the example for 5cm from the bottom of the well counter in **Figure 2-3**.

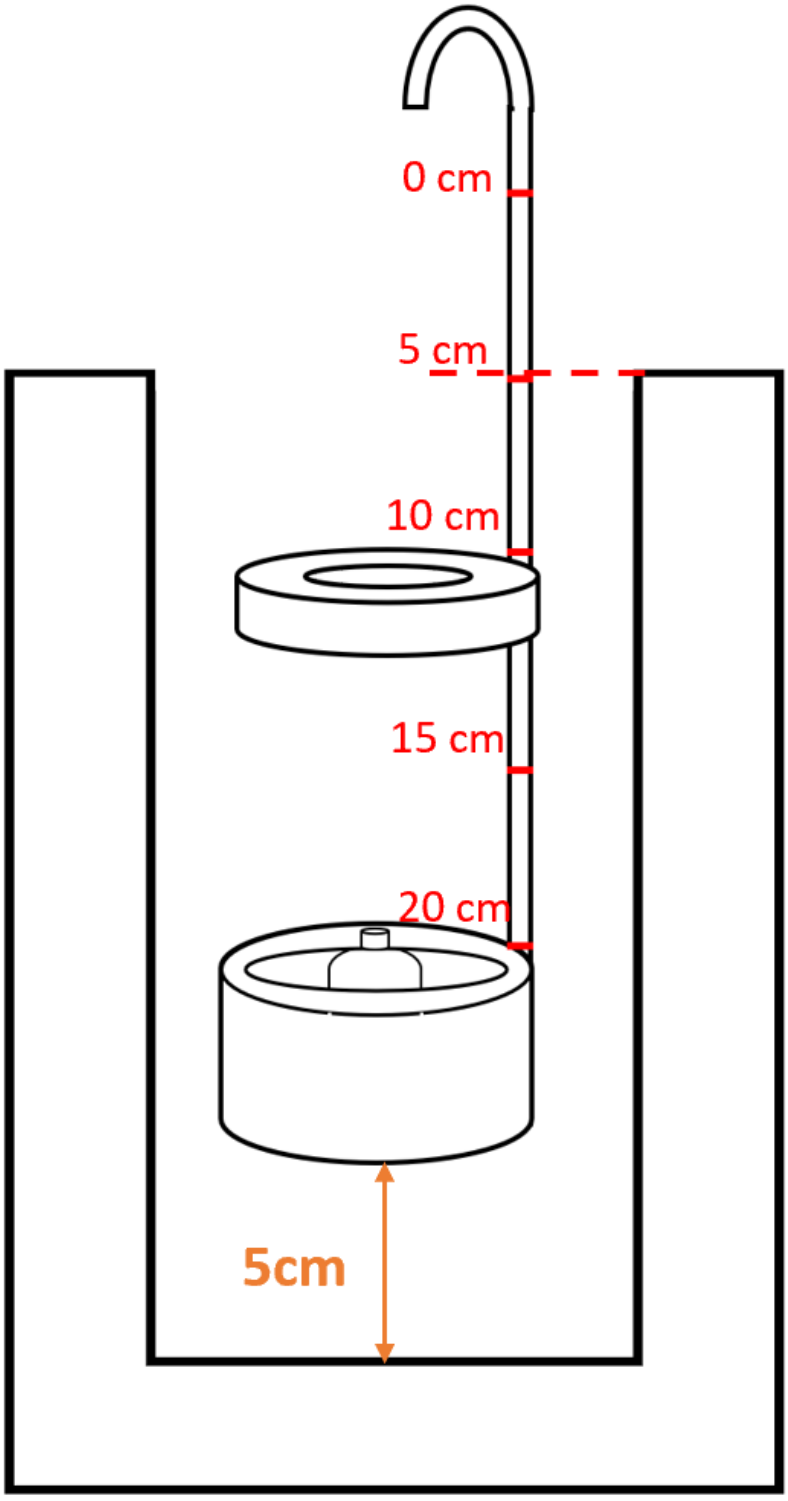

Figure 2-3 *Atomlab vial measurement with dipper 5cm from the bottom of the well, determined using markings placed upon the dipper.*

2.2.2 Vial Geometry Results

Decay corrected results were compared to ANSTOs provided calibration with the variation for each result displayed in **Figure 2-4**. The further the points deviate from 0, the larger the deviation from the desired ANSTO calibration. The average variation at each height is listed in **Table 2.1**.

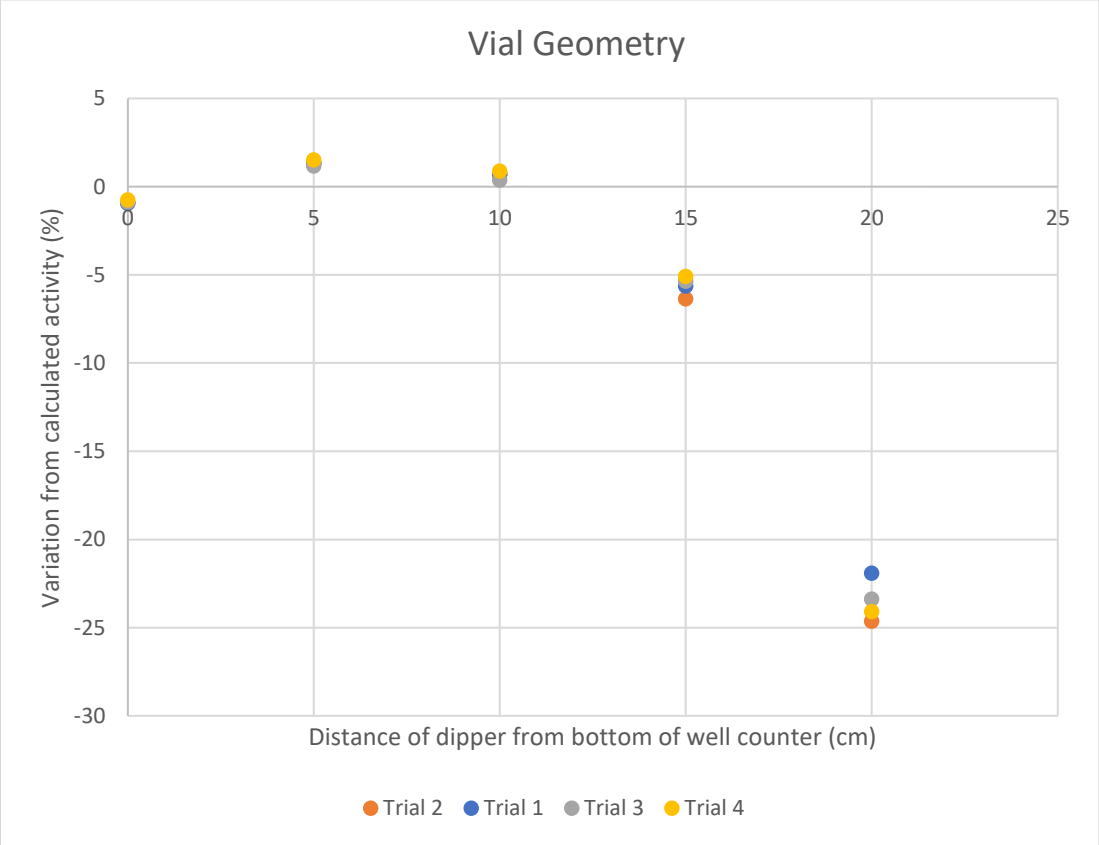

Figure 2-4 *Vial geometry results for all 4 vials.*

Table 2.1 *Average variation from calculated activity for vial geometry.*

Position relative to bottom of the well (cm)	Average Variation from calculated activity (%±SD)
0	0.87 ± 0.09
5	1.34 ± 0.14
10	0.66 ± 0.21
15	5.61 ± 0.54
20	23.5 ± 1.18

2.2.3 Vial Geometry Discussion

The trend between accuracy and depth within the well were consistent. 20 cm from the bottom is highly inaccurate due to the solid angle to the opening being so much greater than the other positions. In **Figure 2-1**, if the 20 cm demarcation were to be level with the top of the well, a larger portion of the 4π volume is not captured by the chamber.

Variations of less than 2% in **Table 1-1** occurred at distances 10 cm or less from the bottom of the well with the smallest at 10 cm. The well counter performs within acceptable limits up to 10 cm from the base of the well when measuring vials and so the Dial Value did not require adjustment. The 10 cm demarcation was established as optimal and was used for all vial measurements in this study.

2.3 Syringe Geometry

Vial stock before and after dispensing is used to calculate the activity that is drawn. For all clinical and experimental work, activity is transferred via syringes and their residuals measured to ensure accurate quantification. As a consequence, syringe geometry was investigated and could only be completed after optimal conditions for vials was established.

Accurate measurement of residuals is clinically relevant where quantification is desired. Fernandez, Allen and Lewington (2015) found residual activity ranging 1.21 to 11.1% of the administered activity. Raharja et al. (2018) recorded an average residual of 2.23% in a study spanning 3 years with average doses of 7497 ± 372 MBq. Additionally, use of Lu-177 with high specific activity in this study had the potential to increase the residual and have a larger impact on the accuracy of smaller activities used in this study.

Due to the short range of beta particles, self-shielding may vary with the volume the activity is prepared in. If the effect is large enough, appropriate correction factors must be established (Iaea & Bailey 2015). Due to ease of varying and measuring volume in a syringe, compared to a vial, this was simultaneously investigated while determining optimal conditions for the syringe geometry.

2.3.1 Syringe Geometry Methods

As per section 2.2.3, a distance of 10 cm from the bottom of the well yields the most accurate calibration for the vial geometry. This positioning was applied when measuring the known activity for the syringe calibration accuracy.

10 mL syringes, identical to those used in the phantom experiment discussed in chapter 4, were used. Unused activity of 0.38, 0.54, and 1.63 MBq remained after three therapies (each had different initial volumes) and were measured using the stock before and after of the vial. The selected activities are much smaller than the clinically expected residuals discussed in the literature. However, they were all that was available at the time of this study and best highlight any self-shielding effects that may have been present. The stock before and after of the vial was used as the comparison for the syringe results. This volume was then measured in the syringe and remeasured using each demarcation on the dipper, as it was for the vial geometry in section 2.2.1, but ceased at 15 cm. This was because the syringe holder is located higher on the dipper as seen in **Figure 2-1**. This meant at 20 cm, the syringe barrel containing the activity would be partially out of the well counter.

As discussed in section 2.1.2, volume dependence that may arise from internal shielding was a concern, so the volume was increased and the samples measured again. The solution was increased to 5 ml using saline and the measurements repeated. Thereafter, volume increments of 2.5 ml were applied as shown in **Figure 2-5**.

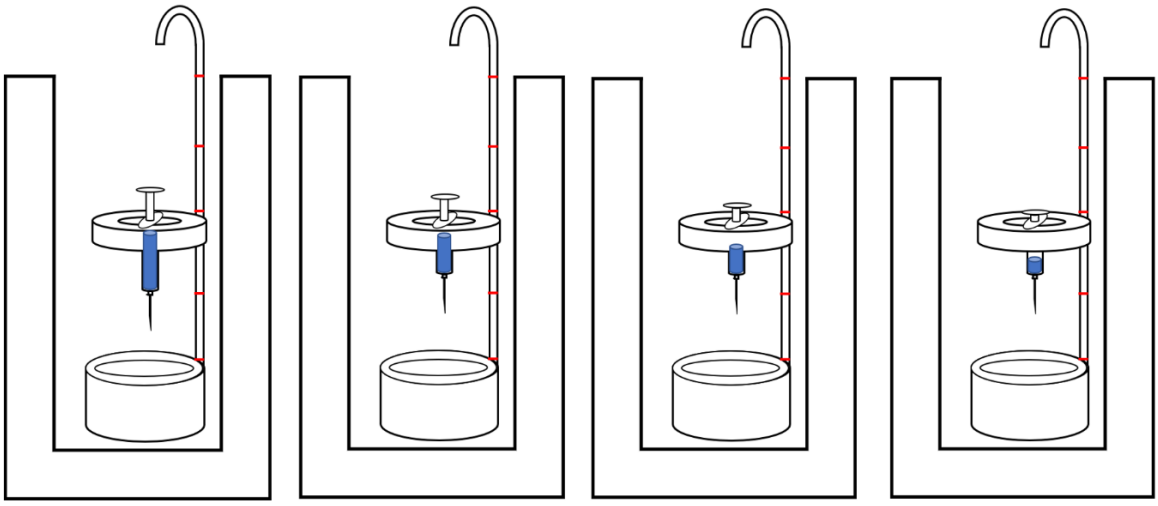

Figure 2-5 *Change in geometry of chamber of syringe with changing volume. From left to right; 10 ml, 7.5 ml, 5.0 ml and <5.0 ml.*

The needle on the syringe was not removed as it also contains residual.

2.3.2 Syringe Geometry Results

The variation from the vial calculated activity for each trial is displayed in **Figure 2-6** to **Figure 2-8**. The closer the points to zero, the better the accuracy. The average variation for each volume at the most accurate height above the base of the well counter is listed in **Table 2.2**.

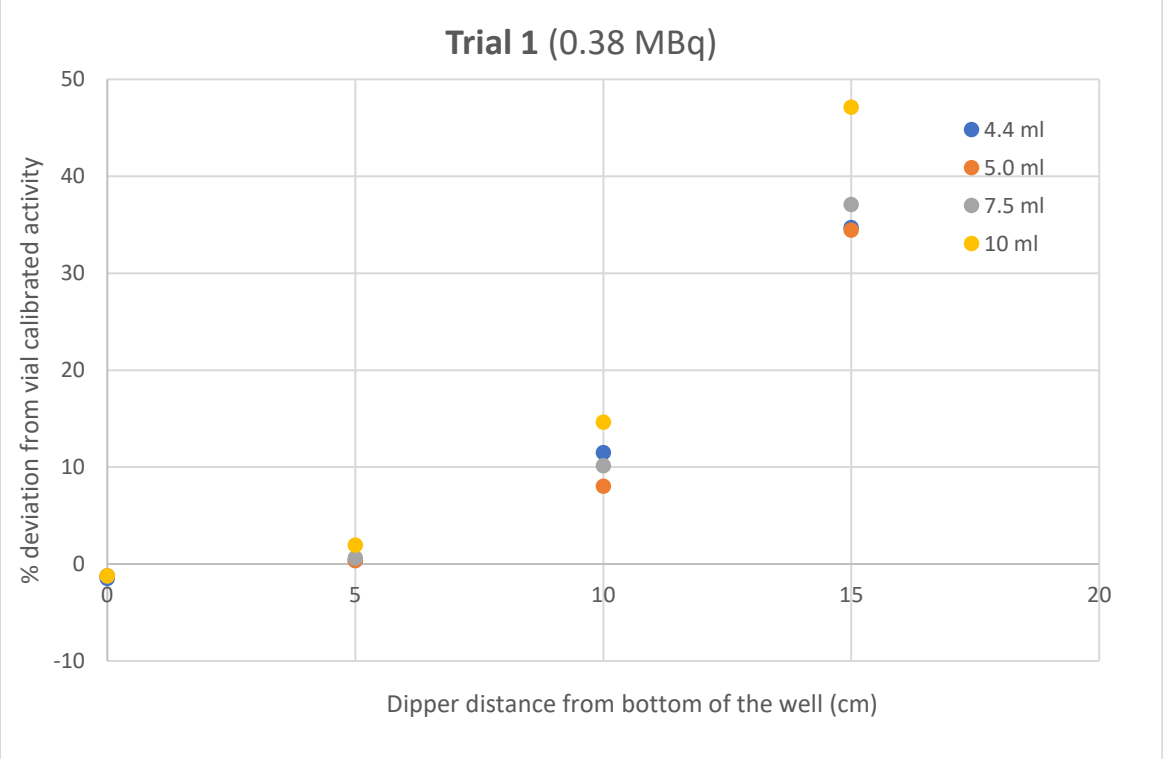

Figure 2-6 *Trial 1 (0.38 MBq) syringe results.*

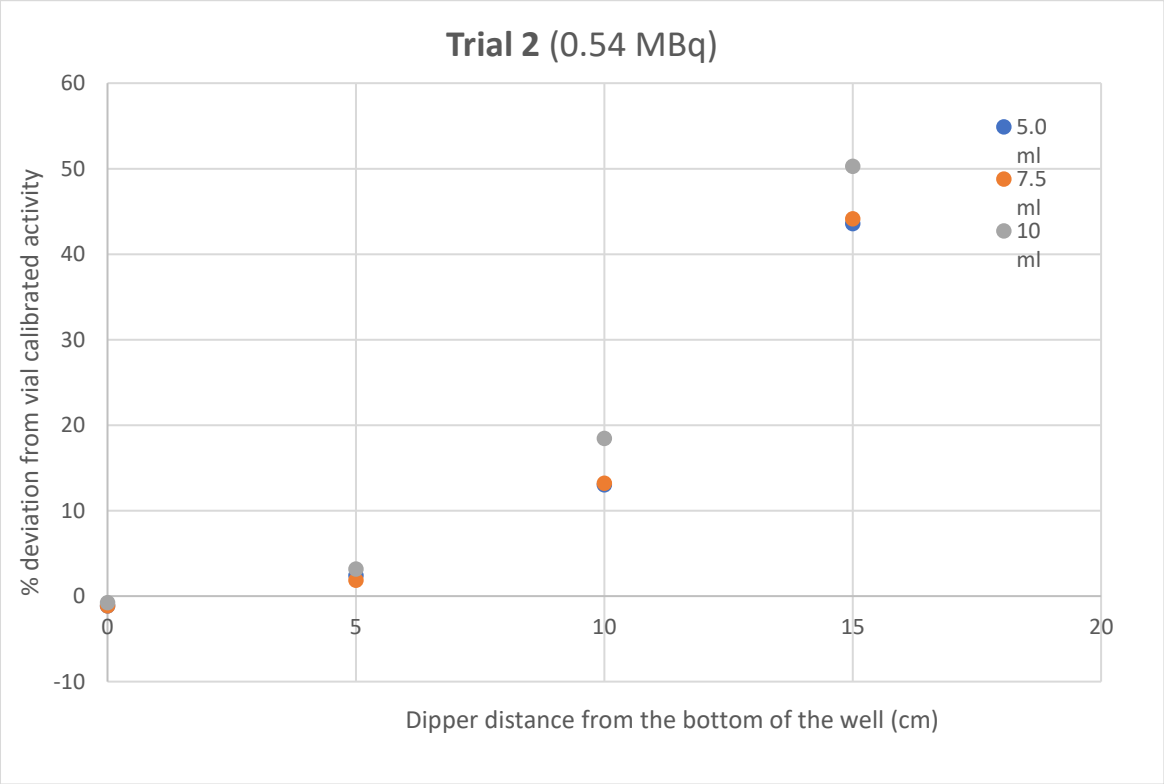

Figure 2-7 *Trial 2 (0.54 MBq) syringe results.*

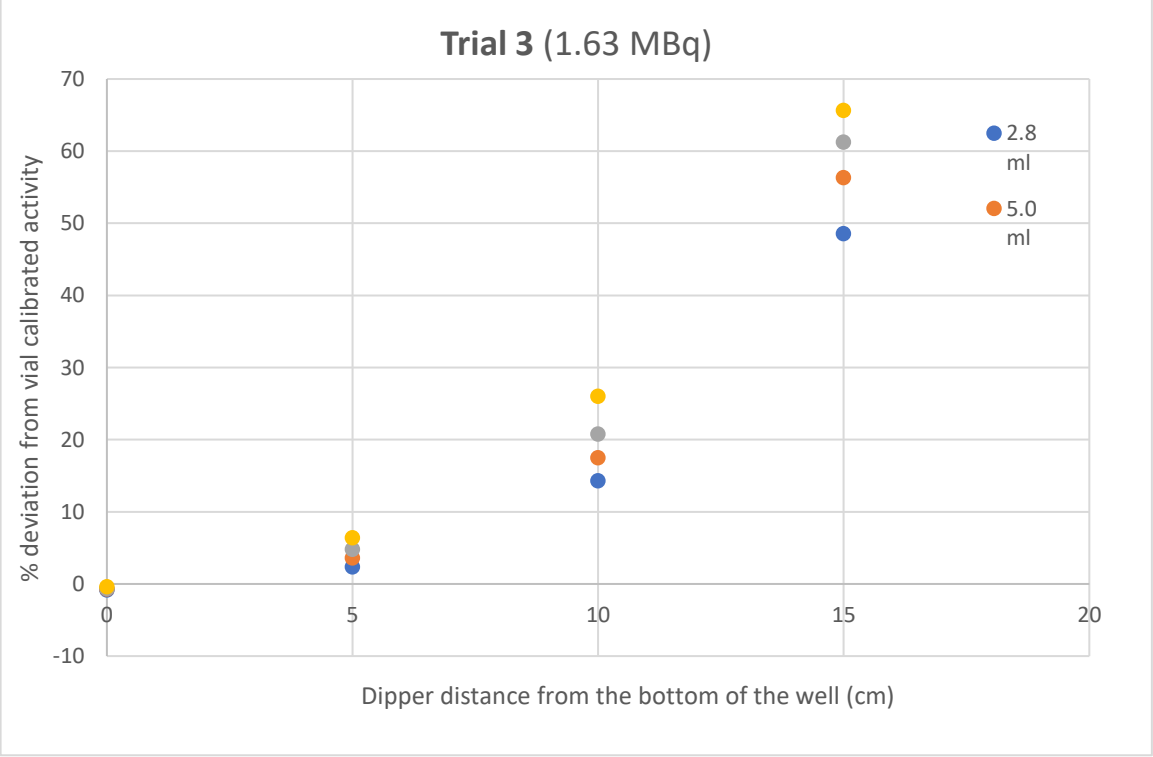

Figure 2-8 *Trial 3 (1.63 MBq) syringe results.*

Table 2.2 *Average variation from calculated activity for each volume of syringe.*

Volume (ml)	Average Variation from vial calculated activity (%±SD)
5.0	-1.02 ± 0.27
7.5	-1.00 ± 0.31
10	-0.79 ± 0.41

2.3.3 Syringe Geometry Discussion

The dipper being at the lowest point of the well (0 cm demarcation) yielded the most accurate measurement, independent of volume. All points with the dipper in this position are the closest to zero in **Figure 2-6** to **Figure 2-8**. This dipper position situates the barrel of the syringe containing the activity in the middle of the chamber, which also produced the best results for the vial geometry.

The vertical spread of the different volume points (different coloured points) at each position in the well in **Figure 2-6** to **Figure 2-8** does not appear dependent on self-shielding created by volume. This spread is related to the changing shape of the source and its effect on the measuring geometry. The less the measuring geometry resembles 4π, the larger the variation from the desired result. The closer the object being measured resembles a point source, the closer the measuring geometry resembles 4π. Increasing the volume in the syringe changes the shape of the source and moves a portion of it further away from the desired position in the well and closer to the opening of the well. While minor at lower volumes, the larger the volume, the further a large portion of activity moves from the 10 cm from the base of the well. As the dipper is raised, these portions are even further removed from the desired position and closer to the opening of the well.

Volume dependency caused by internal shielding of the dose was excluded. If this effect were significant, a large spread of the points for dipper placement at the bottom of the well would be present in **Figure 2-6** to **Figure 2-8**. Additionally, the spread would be more prominent for lower doses since self-shielding would have a larger effect. The spread is larger between volumes in **Figure 2-8** than **Figure 2-6** (1.6 and 0.38 MBq, respectively).

That the spread increases as the dipper is raised higher in all **Figure 2-6** to **Figure 2-8**, reconfirms the effect is due to the changing shape of the dose and the increased effect on where it is positioned in the well counter, rather than self-shielding.

2.4 Conclusion

To summarise, any volume dependence present did not require a correction factor and the Dial Value for Lu-177 did not require adjustment. The most accurate conditions to measure a vial result from the dipper being 10 cm from the base of the well. The syringe, while in its allocated slot in the dipper, yields best results with the dipper placed at the bottom of the well. Although adjustments were not required, it was important to have confidence that the onsite measured activities are reliable, particularly where quantification is desired. The discussed conditions were applied to clinical practice as well as this study.

3 Deadtime

3.1 Background and Literature Review

3.1.1 What is Deadtime

Electronic radiation counting systems exhibit a pulse resolving time, or deadtime, τ which is related to the time required to process individual detected events. The pulses produced by a radiation detector have a finite time duration, so if a second pulse occurs before the first has disappeared, the two pulses will overlap to form a single distorted pulse, as seen in **Figure 3-1**.

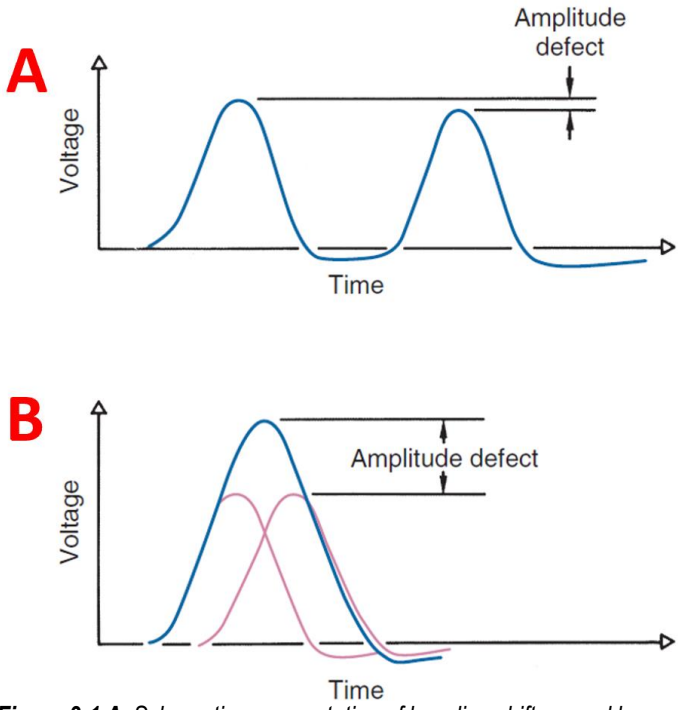

***Figure 3-1 A**. Schematic representation of baseline shift caused by a pulse riding on the tail of a preceding pulse. **B.** Pulse pile-up effects for two pulses occurring very close together in time.*

For SPECT cameras, which use scintillation crystals that are energy sensitive, the overlap in pulses often occurs in the pulse amplifier. This causes a pulse pile up which is a problem that occurs in all amplifiers at high counting rates. Baseline shift is caused by the negative component that occurs at the end of the amplifier output pulse. A second pulse occurring during this component will be slightly depressed in amplitude (**Figure 3-1A**).

At high counting rates, amplifier pulses can occur so close together that they overlap. This is referred to as pulse pile-up (**Figure 3-1B**). When this happens, two pulses sum together and produce a single pulse with an amplitude that does not accurately represent either. Pulse pile-up distorts energy information and contributes to counting losses (deadtime) of the detection system, because two pulses are counted as one. These shifted or overlapped pulse amplitudes may fall outside the selected analyser window, again resulting in a loss of valid events (deadtime losses). The shorter the deadtime, the smaller the deadtime losses.

Deadtime losses also occur in pulse-height analysers, scalers, computer interfaces, and other components that process pulse signals. For SPECT cameras the deadtime is given for the counting system as whole.

When considering the whole system, deadtime is considered as when, after a certain number of photons, the detector becomes overwhelmed and no longer accurately records the photons as counts anymore. Counting systems are classified as paralyzable or nonparalyzable. A *nonparalyzable system* is one for which, if an event occurs during the deadtime τ of a preceding event, then the second event is simply ignored, with no effect on subsequently occurring events. This creates an eventual plateau in the observed counts as seen in **Figure 3-2**.

A *paralyzable system* is one for which each event introduces a deadtime τ whether or not that event actually is counted. Thus, an event occurring during the deadtime of a preceding event would not be counted but still would introduce its own deadtime during which subsequent events could not be recorded. A paralyzable system may be thought of as one with an "extendable" deadtime. As the photons reach and overwhelm the detectors, they miss counts in the time it is taking them to process the photons they're already counting. In paralyzable deadtime, as the photons continue to hit the detector, they extend the deadtime, resulting in even more counts being missed. This results in an eventual decrease in the number of counts as the true count rate increases. This creates a curved shape in the observed counts as seen in **Figure 3-2**. Most radiation detectors behave as paralyzable systems.

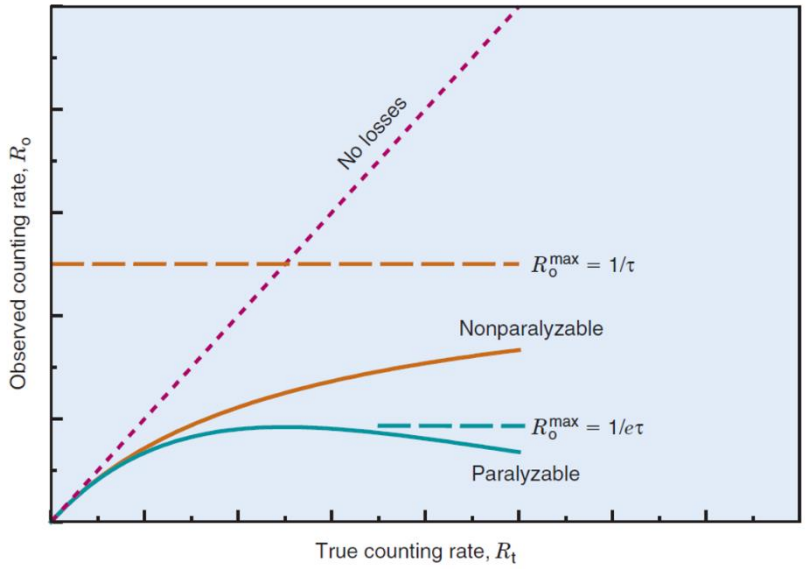

Figure 3-2 Types of dead-time.

The ideal relationship between true and observed count rates is demonstrated by the "No Losses" line in **Figure 3-2**; the higher the activity, the higher the counts should be with a linear relationship. Because of deadtime losses, the *observed* counting rate R_o (cps) is always less than the *true* counting rate R_t (cps), where the latter is the counting rate that would be recorded if $\tau = 0$. The relationship among R_o, R_t, and τ depends on the type of deadtime. For paralyzable systems, the relationship can be described by Sorenson's paralyzable model via **Equation 3-1**.

$$R_o = R_t e^{-R_t \tau}$$

Equation 3-1

It is possible to use this equation to determine τ by recording R_o and using a linear line of best fit to calculate R_t (Cherry et al. 2004).

3.1.2 The Importance of Deadtime

Most modern SPECT cameras, like the one this study focuses on, have a paralyzable deadtime. It is important to measure the deadtime where quantification will be applied (Desy et al. 2020). The deadtime will be specific to the camera, isotope, collimators and energy windowing applied, since all of these factors affect the counts recorded. Hence, the deadtime was measured before commencing the phantom study to ensure it would not interfere with the results.

When measuring deadtime an acceptable threshold is set, beyond which a correction should be considered. In principle, in radionuclide therapy imaging the count losses related to deadtime effects can be substantial, but in Lu-177 imaging, the deadtime effects are small (even for high activities). This is due to the low yield of photons emitted in the decay of Lu-177 and the very small bremsstrahlung contribution. For NET and mCRPC (metastatic Castration Resistant Prostate Cancer) patients, it is the scans obtained immediately after the therapeutic injection that can be affected by deadtime losses, since the patients will not have yet excreted any of the activity (and as there is little opportunity for isotope decay) the total activity would be at its highest (Ljungberg et al. 2016). Quantifying the deadtime is important to identify possible sources of error in quantification.

This study was designed to be clinically applicable, so the acquisition factors used were the same as those used to acquire patient images. That is, the same energy windowing, scatter correction and collimators. The manufacturer has specified that, to be compatible with the XSPECT Quant capabilities, the images must be acquired using Medium-Energy Low-Penetration (MELP) collimators (Siemens 2019). Low energy collimators generally refer to a maximum energy of 150 keV, whereas medium energy collimators have a maximum suggested energy of about 400 keV (Mettler & Guiberteau 2012). Clinically, only the 208 keV photopeak is acquired with Triple Energy Window (TEW) scatter correction applied. There is currently no deadtime correction (DTC) applied clinically at SCGH, likely due to the lack of immediate post infusion therapy scans.

The final methodology was aimed to be time and resource efficient so it could be repeated in any clinical environment. Challenges included limited time on a clinical scanner, and the high cost and limited availability of Lu-177 on the days required. These challenges could be partially addressed by utilising any residual Lu-177 after patients were administered, though at the time of this study the intake of NET and mCRPC patients was not consistent. These challenges could also be addressed by instead utilising Tc-99m where appropriate. For an isotope such as Tc-99m at SCGH, a generator is on site in the Nuclear Medicine department and supply is readily accessible.

Since there is currently no standardised method available for deadtime measurement of an isotope with a half-life as long as Lu-177, methods from other studies were examined and considered. The studies chosen bore similarities to the aforementioned acquisition parameters and assisted in forming the chosen methodology.

3.1.2.1 Energy Windows and Extrinsic Phantom Measurements

Uribe et al. (2018) used a phantom study to determine camera deadtime for Lu-177 using MELP collimators. They compared deadtime based on acquisitions using the full spectrum and the photopeak-only measurements. Specifically, the 113 and 208 keV photopeaks were investigated.

Their measurements were made extrinsically, which means the collimators were on. This requires a higher quantity of Lu-177 than if the measurements were intrinsic (collimators off), since the collimators prevent many of the photons from reaching the detectors. This means more activity is required to increase the number of counts reaching the detector to overwhelm it and cause a deadtime effect. They used a maximum of 9.12 GBq of Lu-177 in a phantom, acquired 26 planar images and fitted the Sorenson paralyzable model to measure the deadtime. They assumed deadtime losses were the same for each projection in SPECT, meaning the findings from planar acquitisions would be transferrable to SPECT (further discussed in section 3.1.2.3).

The true count rate was determined by the extrapolation method where, at very low count rates, there is assumed to be no deadtime and so this data is used to extrapolate the line of "no losses" from **Figure 3-2**.

They found the deadtime values were lower for the single 208 keV photopeak, and based on this they recommended that Lu-177 quantification should be based on acquisition of the 208 keV photons (Uribe et al. 2018).

This published method reconfirmed the use of the MELP collimators, use of the 208 keV photopeak and the use of low activity measurements to extrapolate the true count rate. However, this requires using a large quantity of Lu-177, making it difficult to apply clinically. Other studies have calculated deadtime using less activity on a case by case basis using three images: source alone, source + phantom, and phantom alone. This imaging technique is often named the monitor source method. A revised monitor source method was investigated in a study by Siman, Silosky and Kappadath (2015).

3.1.2.2 Deadtime Uniformity and the Monitor Source Method

Siman, Silosky and Kappadath (2015) used the monitor source method to measure deadtime. This uses three types of scans depicted in **Figure 3-3**.

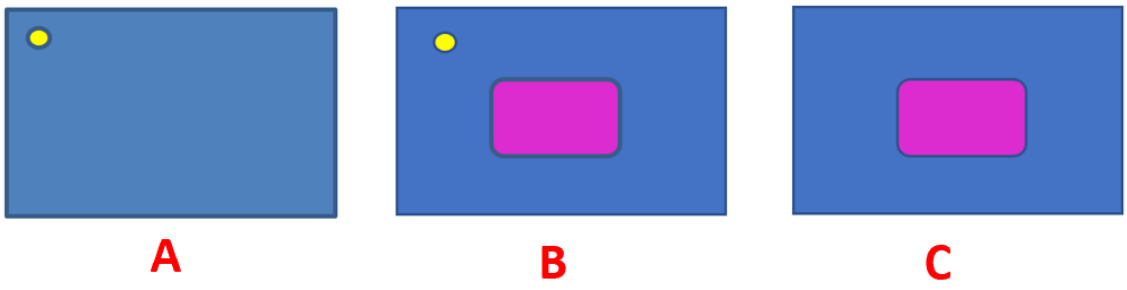

Figure 3-3 *Example FOV for one camera head using the monitor source method.* ***A****. Image with only the monitor source* ***B****. Image with the monitor source and the phantom* ***C****. Image with just the Phantom.*

This study used Tc-99m and Low-Energy High-Resolution (LEHR) collimators, but the method is still applicable. They made a calibration factor (CF), which was calculated as a ratio of the monitor source count rates with and without the phantom. The CF was applied to the phantom images without the monitor source.

They suggested the use of two monitor sources (one per detector) of low activity. **Figure 3-3A** displays the position of the monitor source on one camera head when imaged alone, attached to the corner of the detector's useful FOV. These were placed with a shield of lead encompassing them to exclude photons from the phantom in that part of the detector head when imagining both, as in

Figure 3-3B. This meant only the photons from the monitor source would reach that part of the detector while it would still be experiencing deadtime caused by the phantom. The phantom without the monitor sources was acquired as shown in **Figure 3-3C**.

Unlike the method described by Uribe et al. (2018), the deadtime loss was assumed different for each projection. They corrected each projection and the corrected projection set was used in the reconstruction.

The results of this method confirmed the deadtime to be uniform across the FOV. This means if the sources were arranged as they are in **Figure 3-4**, even if only the central source was inducing deadtime, the counting of the other sources would still be affected.

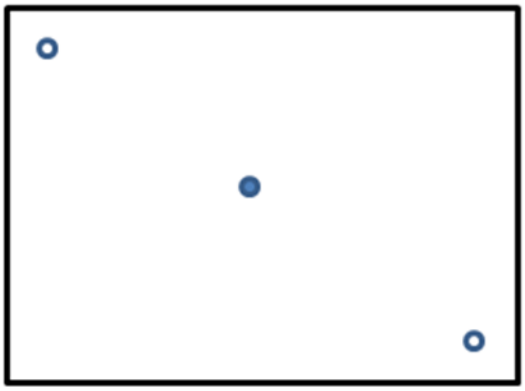

Figure 3-4 *The rectangle represents the FOV (field of view) of the gamma camera head and the circles represent the three sources. If the central source was the only one causing dead-time, the peripheral sources would still experience the same count rate loss since deadtime is uniform across the FOV.*

While a useful confirmation, the use of a shielded point source on each detector is not clinically applicable due to time constraints. This study also did not address the added complications of Lu-177 compared to Tc-99m (such as beta emissions, longer half-life etc).

3.1.2.3 Planar Acquisition and Bremsstrahlung

Celler et al. (2014) attempted to calculate deadtime using Lu-177 using Planar and SPECT imaging. Planar and SPECT imaging of a water phantom containing a small bottle of Lu-177 was acquired over 60 days with two small lutetium markers in all scans. The whole spectrum and singular use of the 113 keV photopeak with various combinations of energy windowing, marker positioning and ROI choices were investigated. The 208 keV photopeak was not considered because LEHR collimators were used.

Variation in the deadtime losses for SPECT angular projections were larger when the detector was closest to the source. However, the differences were much less pronounced when using the 113 keV photopeak. This suggested that with use of a single photopeak, individual projection deadtime loses need not be measured. This was reaffirmed in the good agreement between planar and SPECT measured deadtime results. This meant it was possible to use the planar acquisitions to measure deadtime and the results would still be relevant to SPECT.

Celler et al. (2014) also needed to consider bremsstrahlung from the betas emitted by Lu-177, since they complicate the lower part of the spectrum, including the 113 keV photopeak. The energy of the betas and how they are attenuated changes how they influence the lower range of the energy

spectrum. The use of MELP collimators eliminates the need to consider bremsstrahlung from the betas since the maximum energy of bremsstrahlung photons is relatively low with majority of the created photons below 50 keV a MELP collimator is sufficient to suppress the majority of septal penetration (Uribe 2016). This is not the case with LEHR collimators which prompt the need to account for higher scatter and septal penetration (Beauregard et al. 2011; Ogawa et al. 1991; Uribe et al. 2016).

This, along with advice from MIRD Pamphlet 26 (Ljungberg et al. 2016) reaffirms the use of one photopeak (preferably the 208 keV photopeak), and using MELP collimators, to fully eliminate the complications from beta emissions of the Lu-177. The introduction of a shorter planar acquisition to measure deadtime is also more appropriate give the limited time available in a clinical environment.

To summarise, all studies support the use of the 208 keV photopeak with MELP collimators, and Celler et al. (2014) further confirming it was possible to use planar data to determine the deadtime losses and confidently apply them to SPECT scenarios. This approach is less time consuming than acquiring images using SPECT. However, the studies outlined here used a high Lu-177 activity (> 5 GBq) and took measurements as it decayed over time. This does not fit the time and resource constraints in our clinical setting. To combat this, an alternative method was formulated where activity was added or subtracted before each scan.

3.2 Methodology

Due to the long half-life (6.7 days) of Lu-177 and the time constraints in a clinical department, methods that rely solely on decay were not applicable. Similarly, due to supply limitations, methods where very large quantities of Lu-177 were required were not suitable. Instead, an intrinsic methodology with adding and subtracting activity in planar scans on the same day was developed to combat the time and resource constraints. Section 3.1.2.3 also confirmed planar deadtime measurements are applicable to SPECT, which is the main focus of this study.

3.2.1 Intrinsic

The collimator does not affect *how* the counts are recorded; only how *many* counts reach the parts of the camera head that perform the counting. For this reason, intrinsic (collimator off) measurements were still considered applicable to extrinsic (collimator on) acquisitions if considering counts, not activity, to determine a deadtime threshold. When considering number of counts as a threshold for deadtime, rather than activity, the bremsstrahlung discussed in section 3.1.2.3 is not relevant.

The use of multiple sources was considered appropriate since deadtime is uniform across the FOV, as discussed in section 3.1.2.2. This meant no matter the chosen position of the sources, they could still induce deadtime that affects the whole gamma camera head. However, the position of the sources does have an effect on the number of counts reaching the detector, simply through geometry. This is why the multiple sources were placed as close to the centre of the FOV as possible, where the highest proportion of their counts are likely to reach the detector. This effect is discussed further in section 3.3.1.

The chosen intrinsic method bares similarity to the AAPM-TG177 (2019) report methods for deadtime, not using a collimator and using counts to calculate the threshold for deadtime. However, their recommended set up suggests the detector should be uniformly irradiated via the source being 5 times the length of the FOV away from the detector. This is not practical considering the size of the

scanning room. Uniform irradiation is recommended when establishing an activity threshold for deadtime to ensure placement of the source does not affect how much activity is required to overwhelm the detector. If the source is placed where a larger portion of its counts are not intercepted by the detector, this affects the determined threshold. By using a count threshold, this issue is circumvented.

3.2.1.1 Intrinsic Methodology

The half-life of approximately 6.7 days meant it was not possible to collect a large volume and spread of data in a few days if solely relying on decay of a single source. Instead, multiple sources were used to acquire multiple data points on the same day.

To eliminate risk of contamination with the use of an unsealed source, a small volume and activity of Lu-177 was placed into 9 separate v-vials. This allowed addition and subtraction of activity using sealed sources. Each vial contained between 9 and 10 MBq of Lu-177, the activity drawn in accordance with the methods described in chapter 2.

The SPECT/CT has a probe that extends from the bed to the middle of the gamma camera head's FOV, **Figure 3-5A**. To reduce inconsistencies that arise from positioning, the v-vial holder in **Figure 3-5B** was 3D printed. The plans for the holder were drawn on Tinkercad, which produces files in a format compatible with the 3D printer in the Nuclear Medicine Department at SCGH.

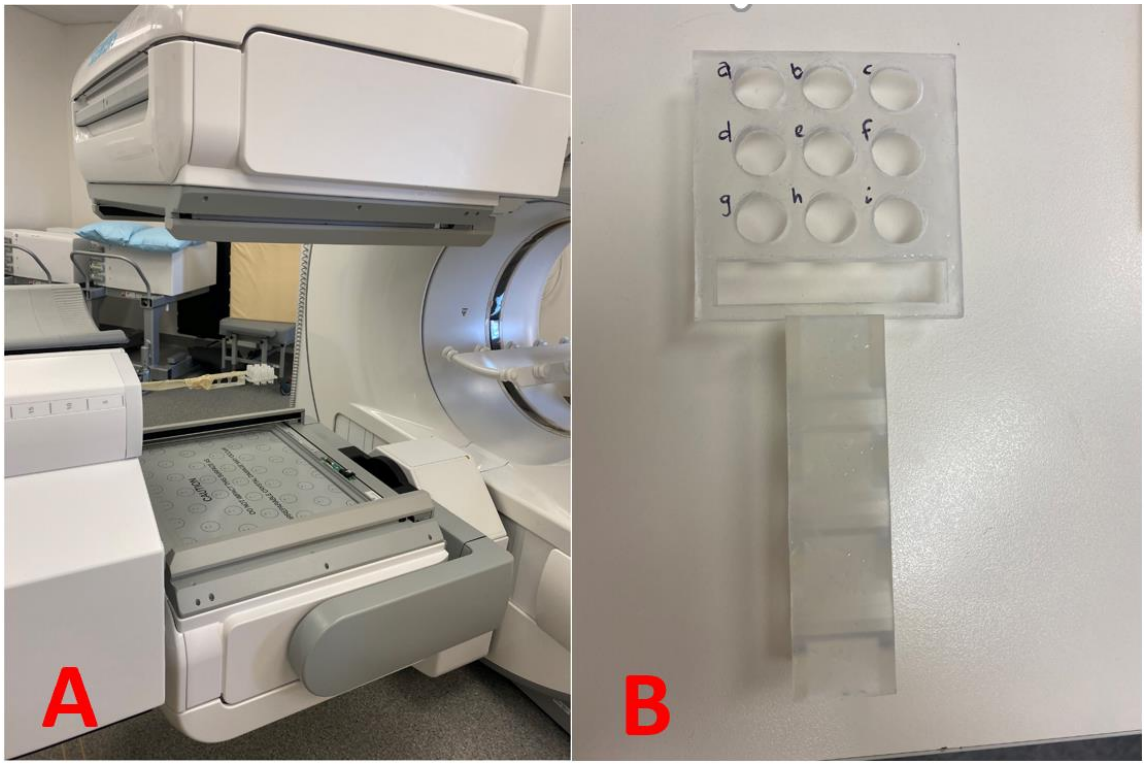

Figure 3-5 A *The probe extending from the bed to the middle of the camera FOV with the v-vial holder attached.* ***B.*** *3D printed v-vial holder close-up with slots to hold v-vials labelled 'a' through 'i'.*

Each slot, labelled 'a' through 'i', in **Figure 3-5B** corresponds to a specific v-vial, identically labelled 'a' through 'i'. This ensured consistent placement and record of exact activities for each v-vial. A bird's eye view of the initial configuration, containing all the v-vials, is displayed in **Figure 3-6A**.

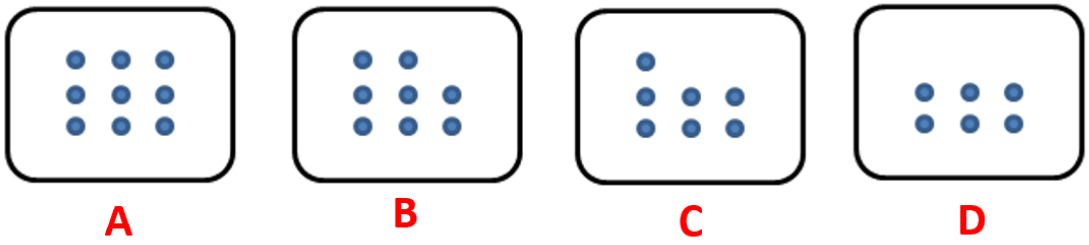

Figure 3-6 *Multiple v-vials (●) placed in the holder from bird's eye view.* ***A.*** *The initial configuration with all vials in the holder.* ***B-D*** *consecutive configurations, with one vial removed each time. Each configuration is individually imaged.*

A planar image of the source cluster in **Figure 3-6A** was taken, with subsequent acquisitions made after the removal of an individual v-vial. This process was repeated until only one v-vial remained. Imaging took place a minimum of once a week with these configurations. The camera was set up with the same distance to collimators and bed position each time. The objective was to obtain data that appeared as in **Figure 3-7**.

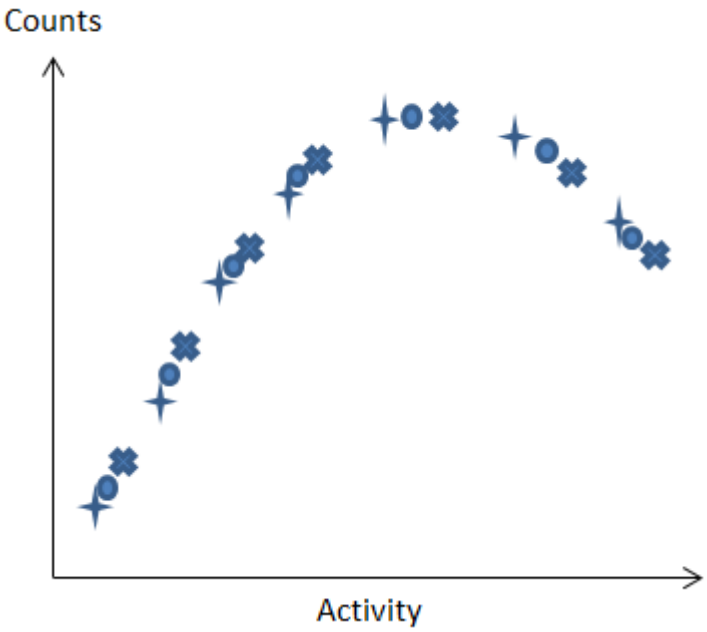

Figure 3-7 ✖ ● ✦ *are different days of data collection. Each day has multiple images taken with consecutively fewer v-vials, achieving a high volume and spread of data.*

Taking multiple images, each of a different activity, on the same day, allows collection of a higher volume and wider spread of data in a shorter time frame than a single source solely relying on decay. Since there are 9 sources, each day of imaging produces 9 data points. This process was repeated 9 times for a total of 81 data points for each camera head. This method also provides more data in the lower range of counts than the upper end as the sources decay. This was desirable considering it is the lower count data used to extrapolate the true counts graph in **Figure 3-2**.

3.3 Results

The resulting intrinsic data successfully resembles that shown in **Figure 3-7**. The results for camera head one shown in **Figure 3-8**.

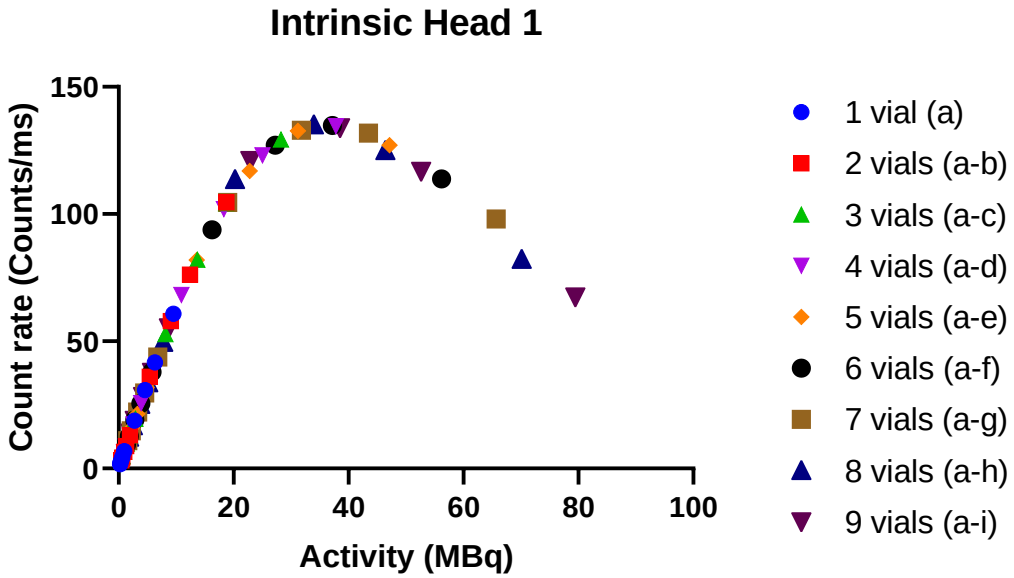

Figure 3-8 *Intrinsic measurements for camera head 1, using measurements of multiple vials on the same day. Results for camera head two can be found in Appendix A.*

3.3.1 Empirical Intrinsic Position Correction

While documents such as AAPM-TG177 (2019) suggest it is acceptable to use intrinsic methods, there was still a concern of positional dependence. The various positions of the v-vial sources affect how many of their counts reach the detector.

To observe this effect, each day the same v-vial 'a' was individually imaged in each position on the paddle in **Figure 3-5B**, and the count rate was recorded. The results were decay corrected using **Equation 3-2** .

$$ACCR = \frac{CR}{A_o e^{-\lambda t}}$$

Equation 3-2

where *ACCR* is the activity corrected count rate, *CR* is the count rate taken from the DICOM information of counts and length of acquisition, A_0 is the initial activity of the v-vial at calibration, λ is the decay constant for Lu-177 and *t* is the time difference between the initial calibration and scan time.

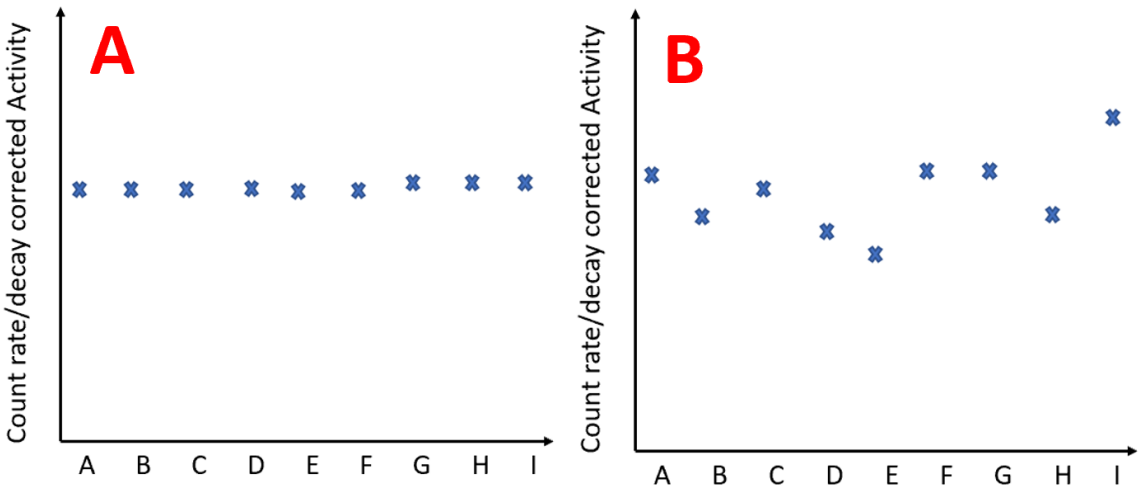

Figure 3-9 *If the decay corrected results of the single v vial had no positional dependence, the results would appear like either* ***A.*** *where all are approximately the same or* ***B.*** *a seemingly random distribution.*

If the position had no effect, the results would resemble **Figure 3-9A** where the results are all approximately the same, or **Figure 3-9B** where the results are randomly distributed. Results for camera head 1 are plotted in

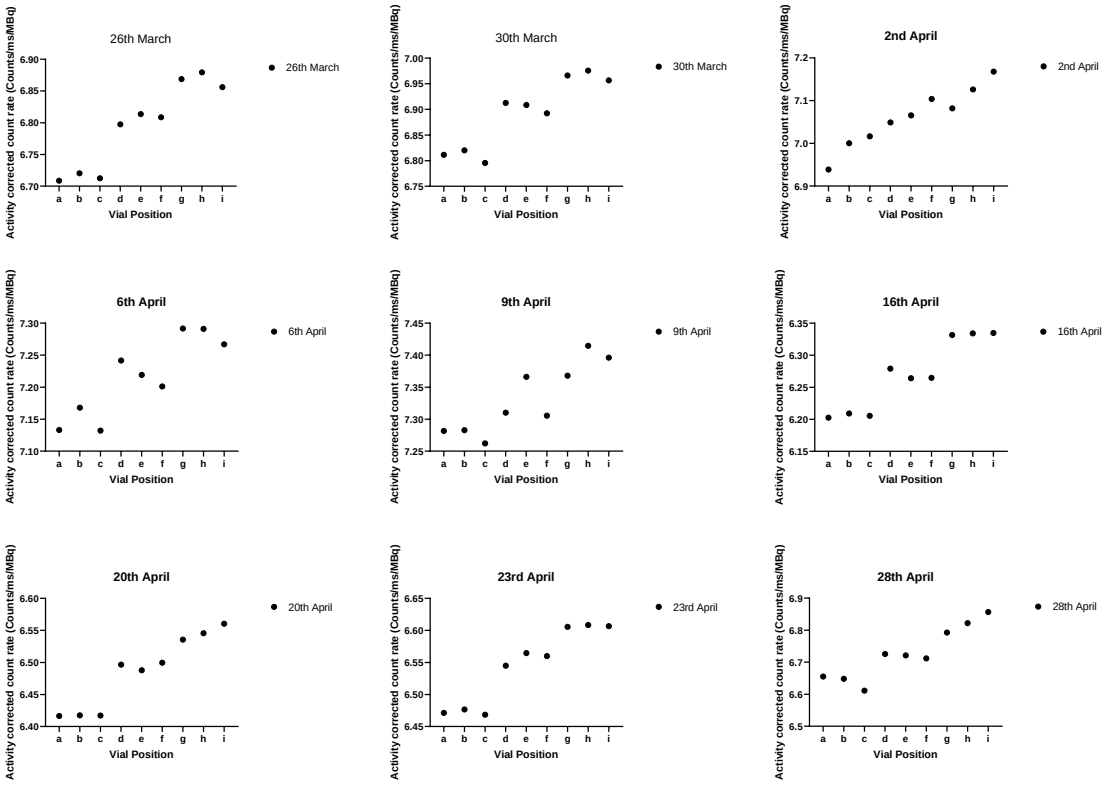

Figure 3-10. All camera head 2 results not displayed can be found in Appendix A and Appendix B.

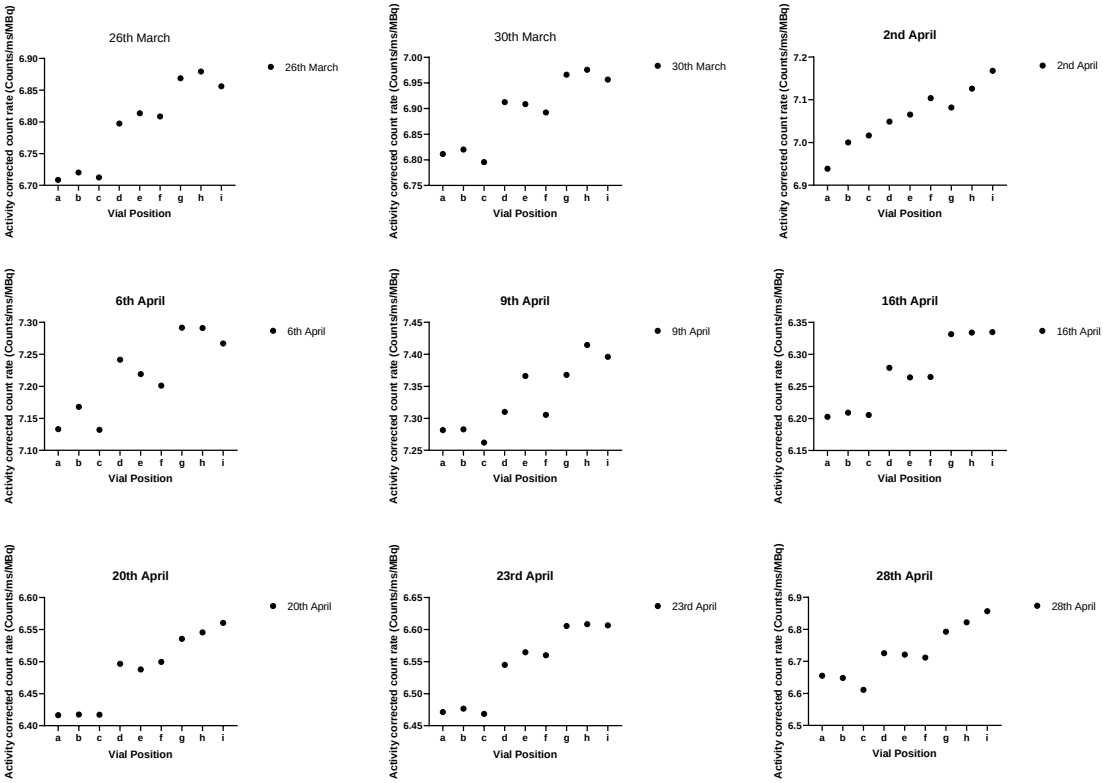

Figure 3-10 *Results for camera head 1, V-Vial-a imaged in every position, 'a' through 'i', in the holder on each day of imaging. The results are decay corrected.*

The resulting **Figure 3-10** does display a repeating pattern in the ACCR depending on the position of the vial. The row of 'g', 'h', 'i' is consistently the highest. That row is the closest to the centre of the camera and the placement of the sources where it is expected more of their counts will reach the detector.

Despite the cause being geometric, the correction applied was empirical. This is because the detector is not uniformly sensitive enough (even with uniformity corrections) to allow for this. Additionally, the setup of the camera head does not facilitate a geometric correction. In rudimentary terms, featured in **Figure 3-11**, the collimator holes are in a "honeycomb" pattern and each hole is hexagonally shaped. Once some of the photons pass through the collimator and reach the scintillation crystal (which is a slab) they produce light spread out which is then picked up by the photomultiplier tubes (PMTs) that are positioned over it.

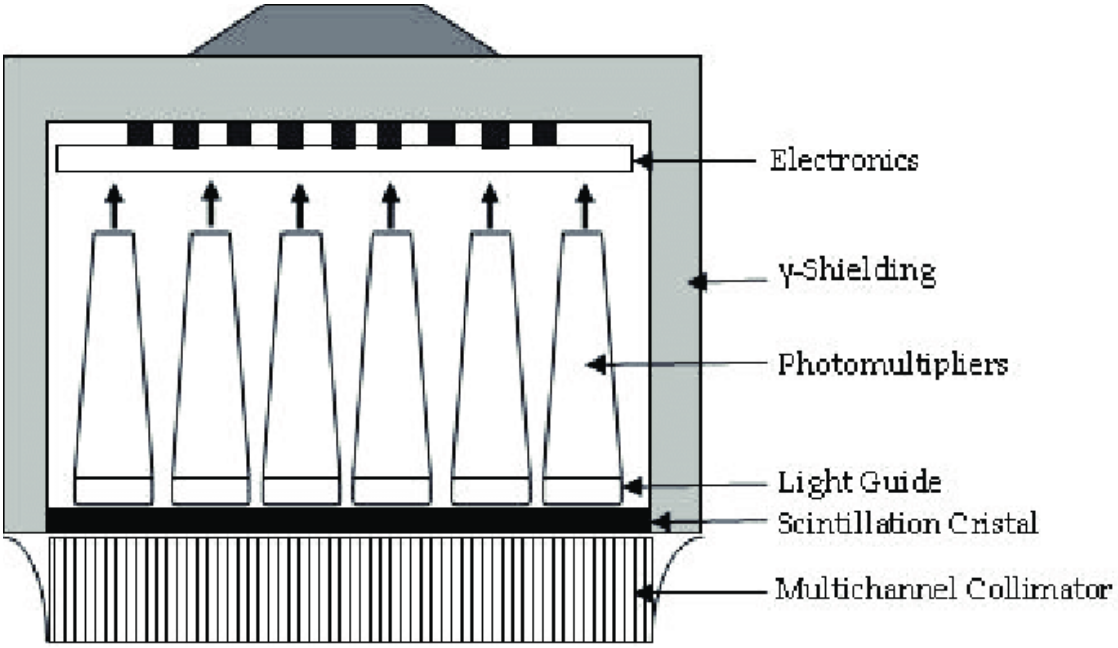

Figure 3-11 *Basic layout of a gamma camera head with collimators, scintillation crystal, PMTs and electronics.*

The distribution of light is picked up by multiple PMTs and the distribution of the signals these PMTs give is as in **Figure 3-12**.

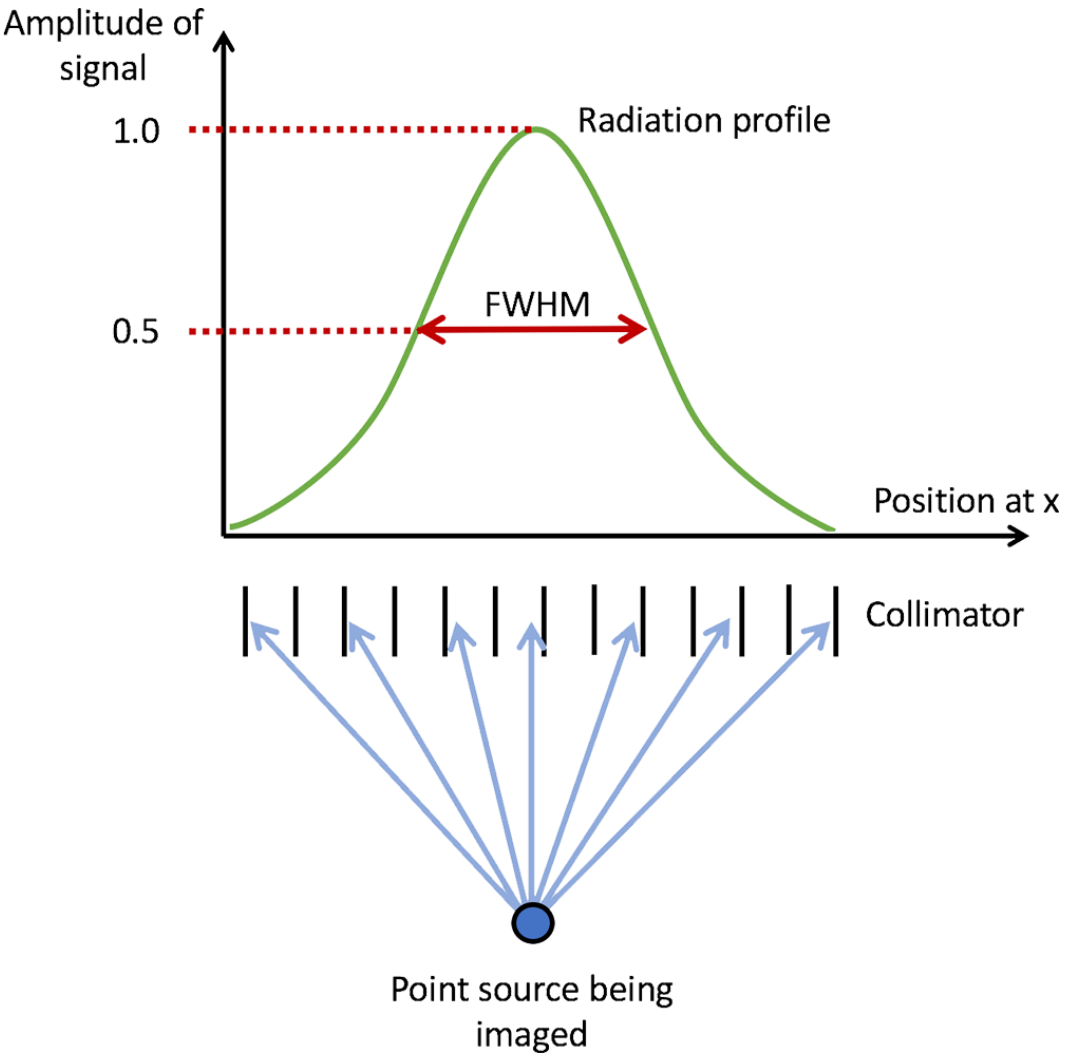

Figure 3-12 Distribution of signals produced by PMTs in a gamma camera head.

The peak in **Figure 3-12** is what is used to assume the position of the source (Cherry et al. 2004). A correction based on geometry would be complex and is beyond the scope of this study.

Instead, an empirical correction was applied using a correction factor to change the counts to what they would have been, had they been placed in the slot that allowed the most counts to reach the detector. This is the 'i' slot in **Figure 3-5B** as it was one of the most central to the camera heads. The correction factor was a ratio of the count rates of a chosen reference position to the position of interest using **Equation 3-3**.

$$CF_x = \frac{CR_x}{CR_i}$$

Equation 3-3

where CF_x is the correction factor for position x, CR_x is the raw count rate for position x and CR_i is the count rate for the reference position i.

This ratio in **Equation 3-3** was always determined from the positional data collected on the same day as the data it was applied to. An example of the full application of this correction is **Equation 3-4** where A_h is the activity of vial h and A_{hi} is the combined activity of vials h and i.

$$PCCR = \frac{A_h}{A_{hi}} \times CR_{total} \times CF_h + \frac{A_i}{A_{hi}} \times CR_{total} \times CF_i$$

Equation 3-4

where *PCCR* is position corrected count rate, *A* is the activity, *CR* is the count rate and *CF* is the correction factor, with the CF for position 'i' always equal to 1.

The Activities, *A*, were not decay corrected to the exact same time, as the total time to acquire all 9 data points took a maximum of approximately 20 minutes. With a half-life of approximately 6.7 days for Lu-177, a decay correction was concluded inconsequential (with 20 minutes producing a maximum change of < 0.02 MBq per vial).

The correction using **Equation 3-4** corresponds the vials 'h' and 'i' are being scanned. The activity in 'h' is divided by the total activity being used and multiplied by the total count rate so as to separate out the part being corrected to position 'i'. That part is then multiplied by the correction factor for that position using **Equation 3-3**, which is the ratio of the *AACR* for position 'h' and 'i', measured that day.

A different iteration of this correction is **Equation 3-5**, where it is for vials 'g', 'h' and 'i' being scanned.

$$PCCR = \frac{A_g}{A_{ghi}} \times CR_{total} \times CF_g + \frac{A_h}{A_{ghi}} \times CR_{total} \times CF_h + \frac{A_i}{A_{ghi}} \times CR_{total} \times CF_i$$

Equation 3-5

Again, each portion of the count rate to be corrected is separated out, corrected, then put back together again. **Figure 3-1** further illustrates the breakdown of **Equation 3-5**.

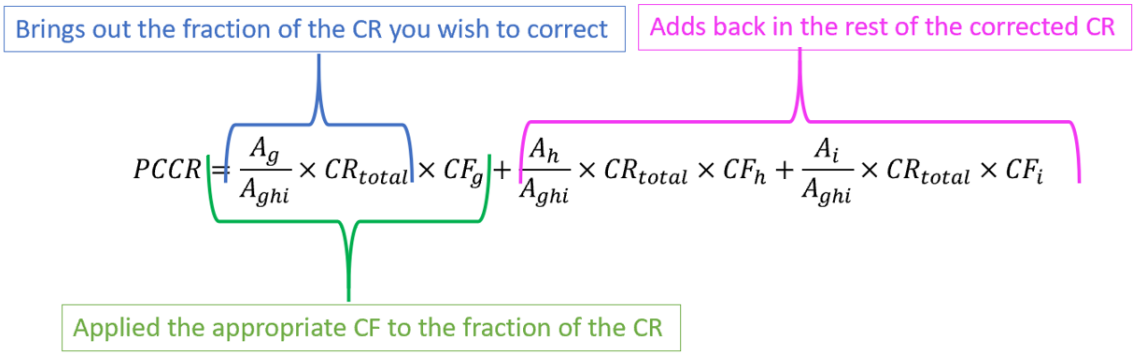

Figure 3-13 *A breakdown of* ***Equation 3-5****.*

The validity of this correction was tested statistically. The results for camera head 1 with and without the CF are plotted in **Figure 3-14**.

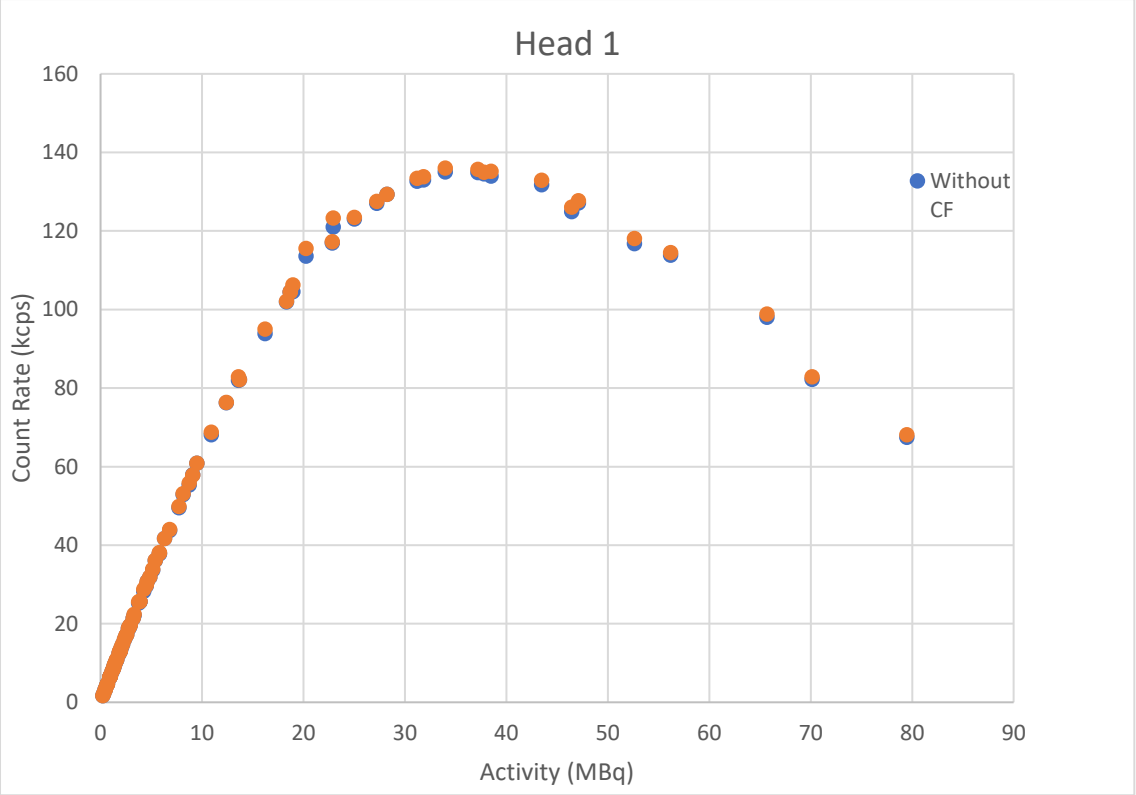

Figure 3-14 *The intrinsic deadtime results with and without the CF for camera head 1.*

The shift between *with* and *without* the CF in **Figure 3-14** did not seem visually significant, but it was tested for a statistically significant difference.

The **D'Agostino-Pearson** normality test was applied in *PRISM* to confirm the lack of normal distribution; the details of this test and its results can be found in Appendix B. Once lack of normality was confirmed, the Wilcox matched pairs test was employed to check for a statistically significant shift after the CF was applied. The resulting P-value is <0.0001 when <0.05 is required for a statistically significant difference. Further details of this test and its results can be found in Appendix B.

With the statistical significance confirmed, the corrected data was used in all future analysis.

3.3.2 Intrinsic True Count Rate

To determine the line of no losses for the intrinisic data with the CF, linear regression was applied. The data up to approximately 100 kcps (100 counts/ms) was plotted and fitted with a linear regression, after the highest count rate point was removed and another linear regression fitted. The process was repeated until a satisfactory correlation coefficient, root mean square error (Sy.x) and a consistent non-deviation from linearity were produced.

PRISM classifies deviation from linearity as a run test, which asks whether the curve deviates systematically from the data. *PRISM* help states:

"A run is a series of consecutive points that are either all above or all below the regression curve. Another way of saying this is that a run is a consecutive series of points whose residuals are either all positive or all negative. After fitting a curve, Prism counts the actual number of runs and

calculates the predicted number of runs (based on number of data points). The runs test compares these two values."

If data is randomly distributed above and below the regression, the number of expected runs can be calculated using **Equation 3-6**.

$$Runs = \frac{2\alpha\beta}{\alpha + \beta} + 1$$

Equation 3-6

where runs are the expected number of runs, α is points above the curve and β points below the curve. If the fit is poor, there is a tendency towards clusters of points on one side of the curve. This results in fewer runs than predicted from the sample size, and the runs test will produce a low P value.

The P value determines if the data are randomly scattered above and below the curve, what the probability is of observing as many runs (or less) than are actually observed in this analysis. If the P value is low, the curve poorly describes the data (GraphPad 2022b).

Sy.x can be an alternative or additional goodness of fit parameter to the correlation coefficient. It quantifies the standard deviation of the residuals. The mean of the residuals is always zero, so to compute the standard deviation, prism adds up the sum of the squared residuals, divided by the number of data points minus one as in **Equation 3-7**.

$$RMSE = \sqrt{\frac{\sum(residuals^2)}{n - 1}}$$

Equation 3-7

where *n* is the number of data points. Rather than report *RMSE*, Prism reports *Sy.x* as in **Equation 3-8**.

$$Sy.x = \sqrt{\frac{\sum(residuals^2)}{n - k}}$$

Equation 3-8

where *k* is the number of parameters fitted by the regression. The value *n-k* is the number of degrees of freedom of the regression. If only one parameter is fitted, *RMSE* and *Sy.x* are the same, which is the case here. If more than one parameter is used, *Sy.x* is larger and a better estimate of goodness of fit between the two parameters. Both are expressed in the same units as the y axis values and are interpreted as the typical deviation of the points from the line (GraphPad 2015).

A Sy.x less than one and the correlation coefficient greater than 0.999 were the thresholds. These and a consistent non deviation from linearity resulted in a linear trend determined with the data up to approximately 25 kcps for camera head 1 and 20 kcps for camera head 2. The results for the true count threshold for the line of no deadtime losses for each camera head are listed in **Table 3-1** with the full results in Appendix C.

Table 3-1 *True count rate results to determine threshold for deadtime for both camera heads.*

	Camera Head 1	Camera Head 2
Threshold Count Rate (kcps)	25.5	19.7
Correlation Coefficient	0.9995	0.9998
Sy.x	0.1471	0.07972
P-value	0.3630	0.7147

3.4 Extrinsic Activity for Deadtime

The count rate thresholds for deadtime were applied to the extrinsically acquired phantom data to determine if deadtime losses would have a noticeable impact.

At its highest activity, the total acquisition time was approximately 9 minutes. The acquisition parameters include 60 views with stop conditions of 40 kCts per view. This equates to a count rate of approximately 4.4 kcps. As this count rate is below both thresholds in **Table 3-1**, deadtime was not considered a significant source of potential error in this study.

The results may also be applied clinically since all that is required to determine if deadtime losses occur is the count rate. The use of count rate as a threshold is more reliable than activity as patients vary in size and weight distribution. The percentage of administered activity within the SPECT FOV depends on the distribution of activity in the patient, which can vary significantly, and also encourages the use of count rate as a threshold as opposed to activity. All these factors significantly impact the attenuation of the 208 keV photons used for imaging and therefore affect the correlation between activity and counts reaching the detectors.

4 Phantom

4.1 Background

4.1.1 Lutetium-177

The increased use and interest in dual imaging and therapy isotopes in the current Nuclear Medicine market has created a desire for increasingly accurate and fast quantification. Quantification plays a large role in dosimetry which can be applied to tumours as well as organs at risk (OARs). Companies such as Siemens and GE have produced SPECT/CTs with automated quantification abilities to try and meet this need. Siemens, for example, has a software feature XSPECT Quant which:

> "Uses a 3% National Institute of Standards and Technology (NIST) traceable precision source, which allows you to easily standardize uptake values across different cameras, dose calibrators, and facilities.
>
> Accurate to within 5%, xSPECT Quant is the industry's most precise and reproducible SPECT/CT quantitative solution. Available for 99mTc, 123I, 177Lu, 111In, and 131I imaging, xSPECT Quant enables clinical SPECT/CT quantification to more precisely detect disease and better manage therapy.
>
> The absolute quantification capabilities of XSPECT Quant are also a basis for Theranostics, the unique approach of combining diagnostics and therapy." (Siemens 2019)

While automated quantification has been examined for Tc-99m in current literature, there is a considerable gap where Lu-177 is concerned. This is of particular interest as Tc-99m is utilized for diagnostic purposes, where Lu-177 has therapeutic applications. Dosimetry, and so quantification, is a particularly desirable capability for therapeutic applications. Clinicians may wish to know the dose to the OARs that arise due to the specific ligand used in the therapy or that arise due to the patient's specific tumour burden, as well as dosimetry on the tumours themselves. Lu-177 has long-standing clinical use for treating neuroendocrine tumours, and more recently metastatic prostate cancer, making it an isotope of interest when considering quantification. While the automated quantification has well understood application for Tc-99m, the findings aren't directly transferable to Lu-177, as the image quality differs due to their different gamma emission energies and abundances.

In 2018 SCGH Nuclear Medicine department acquired a Siemens SPECT/CT with automated quantification capabilities. That year also saw the introduction of treatment of neuroendocrine and metastatic prostate cancer patients using Lu-177. The focus of this study was to address the capabilities and limitations of the Siemens automated quantification, XPSECT Quant, in a clinically relevant environment where Lu-177 is concerned. Which of manual and automated quantification is most viable for future dosimetry was also determined.

4.1.2 Phantom Choice

A National Electrical Manufacturers Association (NEMA) International Electrotechnical Commission (IEC) body phantom was selected for this study. It is a common clinically available phantom, which would allow this study to be replicated at other sites. It was preferable to other readily available phantom options due to its closer approximation to the shape of a human torso and fillable background body, allowing improved approximation of clinical scenarios. It consists of a fillable body phantom, a lung insert and an insert of six fillable spheres of ranging size as seen in **Figure 4-1**.

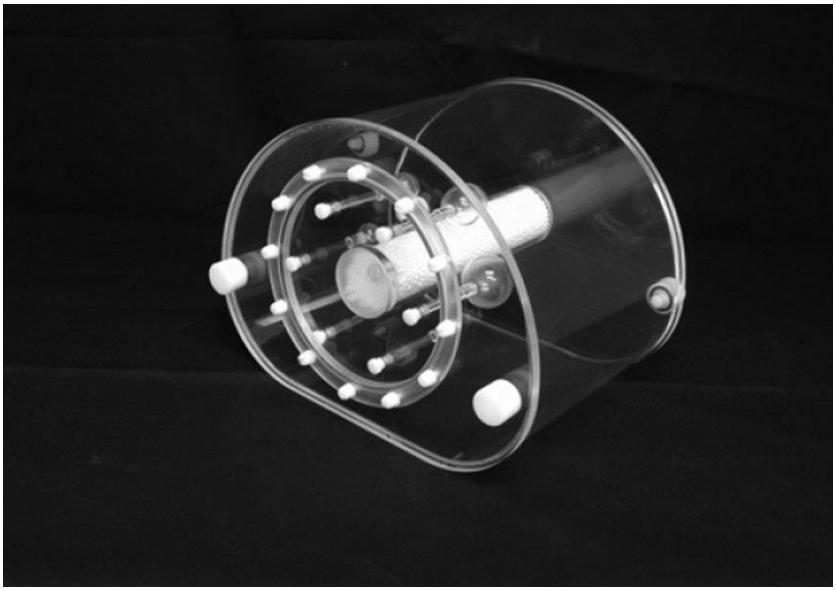

Figure 4-1 *NEMA PHANTOM with lung insert, fillable background and fillable spheres.*

The background volume is 9.7 L. The fillable sphere volumes range from 0.52-26.5 ml, based on the internal diameter of the spheres reported by the manufacturer (Imaxeon 2017). For the purpose of this study, the spheres are referenced as 'a' through 'f' with the smallest sphere 'a' and the largest 'f'. These sphere sizes are representative of smaller possible lesion sizes for neuroendocrine and metastatic prostate cancer and OARs such as salivary glands.

4.1.3 Activity of Lu-177

For clinical relevance, the activities chosen were based on a combination of a literature review and the imaging schedule at SCGH.

Optimal dosimetry requires wholebody SPECT/CTs at multiple time points post therapy. The time points range from 0-127 hours, 0 hours being directly post infusion, before the patient has voided their bladder. The choice of time points varies from centre to centre. At SCGH if multiple time point dosimetry is requested, it is often 24 and 96 hour scans. More common is a single time point, 24 hours post therapy, since the Nuclear Medicine physicians report on this image. At SCGH, if full a dosimetry scan regime is not adhered to, this scan is the minimum. Hence, retention at 24 hours or greater was considered in the literature review. A literature review was selected as the basis for chosen quantities as the available data from clinical patients was minimal at the commencement of this study.

4.1.3.1 Sphere Activity

Whole body retention of approximately 30% at 24 hours is most common for octreotate and PSMA therapies as demonstrated by Levart et al. (2019), Mair et al. (2018) and Nelson, KS, MA (2019). This excretion rate, combined with an administered activity of 8000 MBq, is typical for both categories of patient (Levart et al. 2019; Mair et al. 2018) and formed the maximum phantom activity. It was assumed the phantom represents the area of highest uptake for tumours and OARs, represented by the fillable spheres. Taking 30% of 8000 MBq results in 2400 MBq as the maximum activity contained in the spheres. While a conservative overestimation for an average patient, the desire was to cover a full range of tumour and OAR retention, using decay and other techniques to include much smaller retentions.

The range of activity covered was based on tumour and OAR specific uptake. Much of the literature reported grays per megabequerel (dose per unit activity administered, Gy/MBq) to specific OARs and tumours, rather than uptaken activity (MBq). Tumour burden and uptake also drastically vary, so what is clinically relevant is very broad for activities and tumour sizes. The literature review findings for absorbed dose per cycle are summarised in **Table 4-1**.

Table 4-1 *Absorbed dose per cycle for neuroendocrine cancer and metastatic castrate resistant prostate cancer (mCRPC) patients OARs and tumours (Barna 2020; Bodei et al. 2014; Cremonesi et al. 2006; Garkavij et al. 2010; Gupta et al. 2013; Kwekkeboom, Dik J. et al. 2001; Larsson et al. 2012; Loser 2018; Ozkan 2020; Sandstrom et al. 2013; Wehrmann et al. 2007).*

References	n	Disease	Kidney (mGy/MBq)	Liver (mGy/MBq)	Spleen (mGy/MBq)	Salivary (mGy/MBq)	Tumour (mGy/MBq)	Dose (GBq)
Loser et al.	49	Neuroendocrine	0.69 ± 0.29	0.61 ± 0.34	1.95 ± 1.21		4.25 ± 4.98	7.4
Bodei et al.	5	Neuroendocrine	0.92 ± 0.46					
Cremonesi et al.	10	Neuroendocrine	0.62	0.18	0.64		0.6-56	
Garkavij et al.	16	Neuroendocrine	0.97 ± 0.24				6.7	
Gupta et al.	61	Neuroendocrine	0.57 ± 0.09	0.27 ± 0.05	1.17 ± 0.14		3.41 ± 0.68	
Kwekkeboom et al.	5	Neuroendocrine	0.88 ± 0.19	0.21 ± 0.08	2.15 ± 0.39		3.9–37.9	
Larsson et al.	33	Neuroendocrine	0.8 ± 0.3					
Sandström et al.	24	Neuroendocrine	1.96 ± 1.26	0.59 ± 0.43	0.77 ± 0.44			
Wehrmann et al.	61	Neuroendocrine	0.9 ± 0.3		1.2 ± 0.5		9.7 ± 12.4	
Barna et al.	22	mCRPC	0.71	0.27		0.77 (Parotid)	4.38 (Bone) 5.47 (Lymph Nodes) 4.95 (Liver)	7.42 ± 0.22
Ozkan et al.	10	mCRPC	0.70 ± 0.24			1.34 ± 0.78 (Parotid) 0.94 ± 0.45 (Submandibular) 2.28 ± 1.29 (Lacrimal)		6.48 ± 0.55

The tumour uptake exceeds that for OARs, as observed in **Table 4-1**. While this is not surprising, as that is the desired effect in therapy, it does emphasise the need to cover a wide range of uptake. This is to represent a broad range of poor to exceptional uptake in tumours, and the average uptake to the OARs.

Tumour : background and OAR : background ratios were also considered. These were represented by the sphere : background ratio in the phantom. Due to the difference in uptake in OARs and tumours, there is a wide range of clinically relevant ratios. Even at 24 hour scans, the maximum background activity considered for this study, high tumour and low OAR uptake are possibly present.

4.1.3.2 Background Activity

Clinically relevant background quantities were determined with a literature review of blood concentrations post therapy. There is a greater volume of uptake data published for octreotate than PSMA due to its much earlier establishment.

A study by Abuqbeitah et al. (2018) compared Lu-177 blood clearance rates between therapies. These authors examined 31 neuroendocrine and 23 metastatic prostate cancer patients who had blood samples taken at 3, 10, 20, 40, 60 and 90 minutes as well as at 2, 3, 24, 48 and 72 hours post end of injection time. A Capintec dose calibrator was used to quantify the amount of Lu-177 and the measurements repeated 3 times in an attempt to reduce the relative statistical error. The raw counts were decay corrected from the time of sample measurement in the Capintec to the time the sample was drawn. These corrected counts and a calibration factor of the detector were used to derive the activity in the samples. The early elimination rate and effective half-life in blood were calculated in (mean ± SD) hours with (0.31 ± 0.13), (4.5 ± 1) for octreotate and (0.4 ± 0.1), (5 ± 1) for PSMA, respectively. This study supported the use of octreotate data to represent blood clearance rates for both therapies.

Bailey et al. (2015b) took octreotate patient venous blood samples after injection of the therapy and during each post therapy SPECT scan. There were 0.5, 4, 24, 96 and 120 hour post infusion scans. Each patient received from 2-4 cycles of therapy. Activity per cycle ranged from 6232 – 9096 MBq. The blood samples taken immediately after therapy administration ranged from 150 – 411 kBq/ml.

Forrer et al. (2009) examined bone marrow dosimetry using blood samples. The patients were administered with 7.26 - 7.75 GBq of octreotate and 15 patients had blood samples and bone marrow aspirates drawn simultaneously. 5 blood samples per patient were drawn between 0 - 168 hours post injection. The blood concentration ranged from 1.077 – 6.457 kBq/ml with an average 2.437 ± SD 1.324 kBq/ml.

Beykan et al. (2016) used an animal model to assess the biodistribution of Lu-177-OPS201, a novel somatostatin antagonist showing the highest SSTR2 affinity, the antagonists with superior tumor uptake neuroendocrine tumours. They used pigs for their similar biodistribution, physical properties and long-term follow-up times to humans and their sizes fit a human SPECT scanner. They observed the radiotracer's effect on the kidneys and other OARs. A mean activity of 105 MBq (97–113 MBq) Lu-177- OPS201 was injected into five pigs (three females and two males, age 3 months, weight 25–32 kg). Post administration, 12 arterial blood samples were taken at time points 0.5, 1, 2, 5, 10, 20, 30, 50, 75, 100, 200, and 300 min to determine the time-activity curve of the blood. Three venous blood samples were drawn at 2, 4, 6, and 10 or 12 days after injection. From the whole blood samples, 1 ml was transferred into a counting tube, and the rest was centrifuged to obtain plasma. From the plasma, 1 ml was transferred into a counting tube. Both sets of tubes (whole blood and

plasma) were analysed in a gamma counter normalized to measure Lu-177-OPS201. All samples were measured, and the activity decay corrected to the time of sampling.

These results were scaled to kBq/ml representative for a human. With human administered dose often 8500 MBq or below, and assuming an average weight of 70 kg, the results of this study were scaled. The scaling factor in **Equation 4-1** was applied.

$$Scalar = \frac{HD/_{PD}}{HW/_{PW}}$$

Equation 4-1

where Scalar is the scaling factor, *HW* and *PW* human and pig weight reported by Beykan et al. (2016) respectively, and *HD* and *PD* human pig dose in MBq, respectively.

The scaled results (Appendix D) at 100 and 148 hours were approximately 2 and 1 kBq/ml respectively.

The maximum background activity for the phantom was based on blood concentrations expected at 24 hours. It was assumed 400 kBq/ml at 0 hours, a conservative estimate based on Bailey et al. (2015a), with an effective half-life of 6 hours, the most conservative estimate based on Abuqbeitah et al. (2018) and Mair et al. (2018), resulting in 25 kBq/ml. From Forrer et al. (2009) and Beykan et al. (2016), a minimum of 1 kBq/ml, correlating to 168 hours, was determined to be clinically relevant. This indicated the desired range for this study at 1-25 kBq/ml.

4.1.3.3 Activity Sources

Once clinically representative background and sphere activity were established, consideration was given to the total required activity.

The Lu-177 supplier, the Australian Nuclear Science and Technology Organisation (ANSTO), only produces 5, 10 and 20 GBq vials. The University of Adelaide supplied funding for an initial 5 GBq. Any activity required thereafter was sourced from unused dose after therapies at SCGH. There was no guarantee of available dose after the initial 5 GBq. An agreement with Fiona Stanley Hospital (FSH) was drafted and signed (Appendix E) to supplement this.

4.2 Methodology

4.2.1 Phantom Methodology

As Lu-177 is costly and not as readily accessible as other radioisotopes such as Tc-99m, careful consideration was given to its use. Access to the required scanner in a clinical department is also limited. It was agreed that the imaging was to take place once per day, five days a week, for four weeks. This allowed for a total of 20 data points to be collected. These factors, combined with the desired broad range of data, played a pivotal role in determining the methodology.

Two methodologies were considered to allow a greater spread of sphere to background ratio data within the given constraints.

Sole reliance on decay in both the background and spheres, to achieve the broad spread of data, was ruled out due to the long half-life of Lu-177. This necessitated manually varying the background or sphere activity via dilution and/or concentration.

Varying the activity concentration in the spheres was considered undesirable. When filling a phantom, it is standard to do so with a solution of known activity concentration and to calculate activity in the volume of interest (VOI) using known concentration and known volume. As the volume of the smallest sphere is less than 1 ml, reliably varying its volume and activity would be prone to a high level of error.

In the selected method, on the first day of imaging, the spheres were filled with the highest activity concentration. The background was filled with the lowest desired concentration (1 kBq/ml) and the phantom scanned. The following day, additional activity was added to the background to increase its concentration. The spheres relied solely on decay for the duration of the study and so, were unchanged.

The process of increasing the background concentration was repeated until the fifth day of scanning. On this day, the majority of the background volume (9 L) was removed. It was replaced with water to dilute the solution down to 1 kBq/ml.

Increasing the background activity concentration would recommence the next day and begin the above-described cycle anew. This is illustrated in **Figure 4-2** and described in detail in sections 4.1.3.1 and 4.1.3.2.

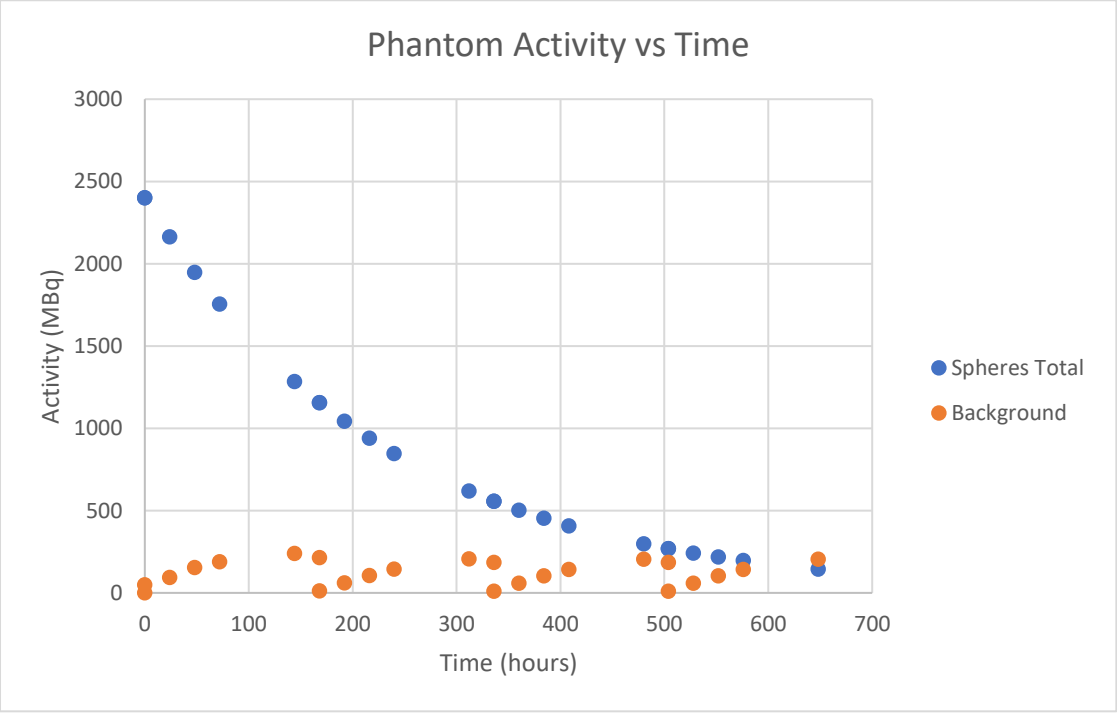

Figure 4-2 *Initial draft of Lu 177 activity in spheres and background of the NEMA phantom for the duration of the study. Sphere activity is the total activity contained in all spheres.*

4.2.1.1 Sphere Solution

The vial of Lu-177 from ANSTO contained a volume of 0.5 ml. This was diluted to a larger volume of 5 ml to increase feasibility of accurately drawing up specific quantities.

A solution of approximately 50 MBq/ml ensured a total of approximately 2400 MBq would be contained in the spheres. As in section 4.1.3.1, this is the highest chosen retention of a 24-hour post therapy scan. The activity was drawn into a 50 ml syringe and the volume increased with water to achieve the desired concentration. The use of the syringe to create the solution allowed ease of

mixing to create homogeneity while minimising the risk of contamination. The volume and activity drawn were recorded.

Filling the spheres required a blunt reusable wide gauge syringe tip. As each sphere was filled, a thick terry towel was placed around the aperture to prevent contamination. This was changed between spheres.

4.2.1.2 Background Solution

For reference, the weekly cycle of scanning began on a Tuesday. On the first Tuesday of scanning, the background was injected with enough activity to create a concentration of approximately 5 kBq/ml using methods described in chapter 2. Prior to each scan, the phantom was spun and shaken to create a homogeneous background solution.

On Wednesday, Thursday, Friday and Monday activity was added to the background. This varied the background concentration between 5 and 25 kBq/ml. Increments of approximately 5 kBq/ml were chosen. The technique employed was identical to that of the first Tuesday. Each subsequent Tuesday was used to dilute the activity back down to approximately 1 kBq/ml, the minimum clinically relevant amount chosen.

Dilution required removal of 9 L of the background volume and replacing it with water. A 500 ml syringe with accompanying tubing was used to extract the volume in a more controlled and measurable manner. The volume of this syringe was verified with a measuring cylinder.

As pictured in **Figure 4-3**, the tubing was secured with a piece of metal bent into an L shape for rigidity. This ensured the solution could still be extracted effectively when the remaining volume was lower. The removed solution was stored in a 30 L water drum.

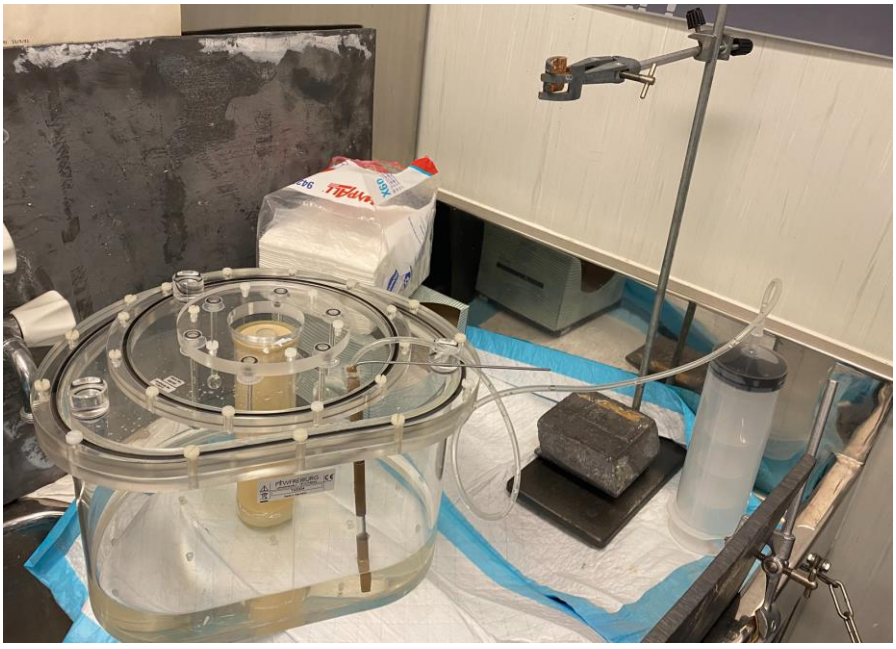

Figure 4-3 *Drainage of the NEMA phantom background in shielded sink using plastic tubing, 500 ml syringe and metal L shape to stabilise tubing.*

Once background draining was complete, 9 L of water was added. A funnel fitting the aperture to the background and a 1 L measuring cylinder were used to replenish the volume.

The NEMA PET phantom pictured in **Figure 4-3** was not the only phantom used in this study.

4.2.2 Bottle Phantom

Conventional quantification often requires a point source imaged with the patient, as referred to in section 3.1.2.2, to convert counts to activity. An alternative method was employed to create a calibration curve for the conversion. As with the point source method, this required imaging a source of known activity.

The background of the phantom was briefly considered as a source of known activity, and while readily available and convenient, was ruled out for multiple reasons:

Firstly, clinical applicability was a priority and this information would not be clinically available. There is no section of a patient that has a known quantity of activity.

Secondly, the calibration curve was intended to be applied to the spheres, which are orders of magnitude higher in concentration than the background (MBq/ml and kBq/ml, respectively). Extrapolating that distantly is prone to high error.

Finally, there was difficulty guaranteeing homogeneity of the background solution. Despite efforts to spin and shake the phantom, it is large and cumbersome, and difficult to be overly vigorous without risk of breaking the phantom. This method has additional risk of the spheres interfering with results.

When selecting VOIs to create the calibration curve, the ideal is a volume with a large margin in a homogeneous solution. This ensures the VOIs remain unaffected by spill out or spill in of counts from other objects. Spill occurs when the object of interest has, for example, low radiotracer concentration relative to surrounding structures and activity from these surrounding areas “spills over” into the structure of interest (Cherry et al. 2004). To prevent spill from affecting the chosen VOIs, a bottle was used.

The bottle was chosen based on criteria to counteract the aforementioned issues of homogeneity, margin and extrapolation.

The bottle should also be made of malleable plastic to be robust against potential damage.

A volume of approximately 2 L was chosen. This volume balanced VOI and extrapolation requirements. It was large enough to provide wide margins for the chosen VOIs, yet facilitated a higher activity concentration. The larger the volume, the more activity is required to create a higher concentration. At minimum, the same order of magnitude as the spheres was desired.

The spheres have activity concentrations beginning at 50 MBq/ml and the background reaches down to 1 kBq/ml. 6000 MBq of activity remaining from clinical patients was available and diluted into the approximately 2 L bottle with water. While the resulting 3 MBq/ml is not the 50 MBq/ml peak concentration for the spheres, it is in the same order of magnitude and allowed the concentration magnitude to span that of the background in final scans.

Scanning took place once a week, relying solely on decay for spread of data. This was based on available access to the camera.

The scan protocol was the same as that for the NEMA phantom, for SPECT and planar acquisitions.

4.2.3 Scan Protocol

A modified version of the Lu-177 clinical protocol was used. For each tomographic scan, 60 projections were acquired using a 256 x 256 matrix. As discussed in section 3.1, MELP collimators and the 208 keV photopeak window were most suitable. TEW scatter correction, with 20% PW and 10% UW and LW, was applied.

Lu-177 patients are not scanned every day so prior to all scans, the camera heads were extrinsically peaked (peaked with the collimators on). If quantification is desired, energy peaking is crucial to correct peak shift. Peak shift is the shift of a specified radioisotope peak from its real position. The shift affects image quality as it degrades uniformity (Mahidul Haque et al. 2016). Peaking is an automated part of the scan protocol and required approximately 200 MBq of Lu-177 in a point source. Peaking was all that was required prior to scanning for the duration of this study. There were no major recalibrations to uniformity or sensitivity for the duration of this study, as advised by Senior Nuclear Medicine Medical Physicist staff as SCGH. All of these details are identical to the clinical protocol.

Clinically, the stop conditions are 17 seconds per view, which was modified to 40 kilo counts (kCts) per view. This created less variation in image quality between scans. With all other parameters identical, the higher the counts the higher the image quality, which affects quantification. With varying activity between scans, time per view stop conditions would have been a root cause for variation in image quality. The desire was to equalise counts across all scans to allow isolation of other reasons for varying quantification accuracy. Furthermore, it guaranteed scans with much lower activity would meet total count requirements set by the manufacturer.

Siemens has specified that image registration and use of its XSPECT reconstruction require a minimum number of counts (Vija, A 2015). The minimum is 6000 kCts, as advised by Siemens engineers and apps specialists. As part of the workflow, Siemens supplies XSPECT Check which displays the total counts.

The number of counts per view and number of views does not directly correspond to the final number of counts in the reconstructed SPECT. What constitutes a count in the reconstructed image does not correspond to one acquisition count, as the count is a line of response that convolves information of many different parts that happen to be aligned at the current projection angle. For example, in a patient, many different parts of anatomy are aligned depending on the projection angle. The number of counts in the reconstructed image also depend on the filtering, FOV and zoom of the specific reconstruction (Cherry et al. 2004).

The chosen 40 kCts per view results in approximately 7000 kCts total, meeting the minimum requirements. While higher counts are desirable, it requires lengthier acquisitions which was not appropriate in a clinical department.

The protocol required the injected activity and time. This was provided with use of an Excel spreadsheet calculating the total activity at the time of the scan. Residuals were not entered, already being accounted for in the excel spreadsheet.

The CT reconstruction recommended by Siemens for attenuation correction is the AC Pelvis SoftTissue 3.0 B08s (Siemens 2016). The CT is converted into a μ-map (i.e., array of attenuation correction exponents) and it is this μ-map that is superimposed upon the 3D acquisition data in order to create path integrals for the photons. Too many sharp discontinuities in the μ-map (such as those that might be created with sharp CT reconstructions) can introduce distortions into the

calculations of path attenuation. The smoother the μ-map, the better, and the errors introduced into attenuation by smoothing out the anatomy are small (Vija, A 2015).

Post SPECT/CT acquisition and running XSPECT check to ensure the final counts were sufficient, dual image reconstruction was applied. The first reconstruction, XSPECT, has the automated quantification ability and allows results to be sent as a PET image. The relevant key difference between SPECT and PET images in this case is the DICOM format for multi-instance series. DICOM files are often broken down into the following format:

-Patient

-Study

-Instance

-Frame

In Nuclear Medicine (NM) format, series such as SPECT (raw and reconstructed) appear as just described with one image (instance). However, each instance has multiple frames in which the individual images are stored. PET format is akin to CT format where each image (each transaxial slice) exists as a separate instance within the series. So, in NM format a SPECT reconstruction will have one image (with multiple frames) whereas in PET format the same SPECT reconstruction will have many images, each with a single frame, the number of images being equal to the number of transaxial slices (Cherry et al. 2004).

Enabling VOI results in kBq/ml required the XSPECT reconstructed images to be sent as PET images. The 3D Flash is the traditional reconstruction and is sent as a NM image. Its VOI results are in proportional counts of the FOV or simply counts, rather than in units of absolute quantification of kBq/ml like the XSPECT produces.

Both reconstructions had skeletal exam type selected.

4.2.4 Tc-99m

Since Lu-177 was not readily available, a trial was run prior to use of Lu-177. The aim was to become familiar with the use of the phantom, camera and scan protocol. Tc-99m was chosen due to its availability and being an included isotope for the XSPECT feature. Details of the methodology and results can be found in Appendix F and Appendix G respectively.

4.2.5 Planar

Planar data is often used in clinical practice at SCGH for whole-body retention. The phantom position was altered for planar scans. Placement on its side, as it was positioned for SPECT/CT, would result in overlap of the spheres preventing quantification of individual spheres. Instead, it was positioned with a birds-eye-view of all the spheres so they would appear discretely. This study did not consider quantification of individual spheres, yet the phantom set up was designed such that this may be possible for future work that wishes to address individual sphere quantification.

The phantom position was recreated for each scan using the information detailed in **Table 4-2**.

Table 4-2 *Phantom and camera positioning information for all acquisitions.*

Initial Camera Position	Homed
Collimator 1	8.3 cm
Collimator 2	26.7 cm
Lateral Bed Position	72.3 cm
Horizontal Bed Position	22.2 cm
Phantom on Bed	Flat edge aligned to bed CT demarcation. Spirit levelled across X and Y axis.

The imaging protocol stop conditions were set to 500 kCts per camera head. Once again counts, rather than time, was selected to equalise their effect on image quality scans.

With use of unsealed isotopes in a clinical area, particularly an isotope such as Lu-177 with a long half-life, risk of contamination needed to be reduced to a minimum. The above-described processes required extensive planning and consideration for radiation safety concerns such as contamination. Details of the radiation safety precautions can be found in Appendix H.

4.3 Results

All results were collected through readily available Siemens multimodality reading software, Syngo.Via, and analysed in Excel and Prism. The initial concentration of the spheres, based on well counter measurements and volume, were decay corrected to each scan date and time using the same method as **Equation 2-6** in excel. These values were used as the comparison point for accuracy.

Syngo.Via allows manual selection of VOIs as a perfect sphere, or through the RECIST tool when reading images in MM Oncology. RECIST is a methodology used to evaluate the activity and efficacy of cancer therapeutics in solid tumors using validated and consistent criteria to assess changes in tumor burden (CanadianCancerTrialGroup 2022). The MM Oncology reading setting was used for all SPECT images as it enables quantitative output, much like it does for PET images. RECIST automatically contours a VOI based on a threshold of the highest concentration it detects, which users set as a percentage of this maximum. RECIST with a threshold of 40% is used clinically, rather than manual VOI selection. RECIST was used for sphere VOI selection due to its clinical relevance, with a range of thresholds. The choice to investigate percentages other than 40% was based on the visible cut-off of a significant proportion of counts, as displayed in **Figure 4-4**.

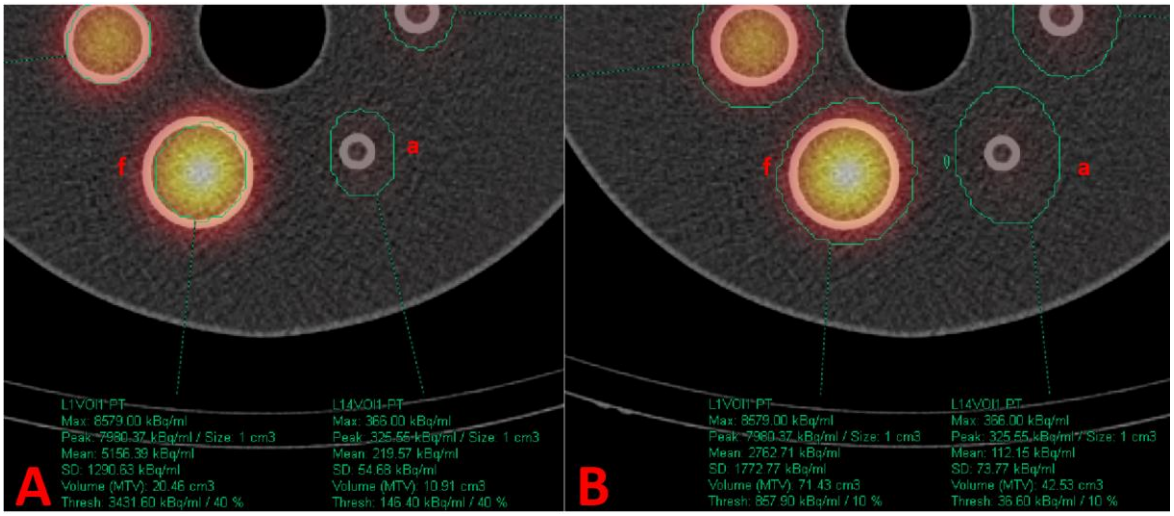

***Figure 4-4 A**. 40% threshold **B.** 10% Threshold for the same acquisition. Both display the largest and smallest spheres (sphere a and sphere f). 40% appears to cut off a significant portion of counts, even for the larger higher activity spheres.*

Once the VOIs are drawn, the threshold may be modified. Data for 10, 20, 30 and 40% was collected.

When the VOI is selected, Syngo.Via provides the factors Max, Peak, Mean, SD, Volume and Threshold, displayed in **Figure 4-4**. Syngo.Via did not allow for export of this data, so it was transcribed into Excel. Prior to determining which Syngo.Via statistics and thresholds were most accurate, consideration was given to the exam type.

4.3.1 XSPECT Automated Quantification

The first data set analysed was the XSPECT, since this was the main focus of the study. As previously mentioned, all activity-based results are presented in concentration form as kBq/ml.

4.3.1.1 Exam type

Within the reconstructions, it is possible to select “exam type”. It was suspected “skeletal” was affecting the results by attributing counts to the plastic of the spheres, possibly due to the higher attenuation.

The reconstruction was re-run with each exam type for 5 scans (7/7/21-13/7/21). The VOIs were selected with 10 and 40% RECIST thresholds, to cover any scenario in which that also played a part.

Each statistic (mean, SD etc.) is expected to be identical for a specific sphere, date and threshold for different exam types. This means there are 8 (the number of different exam types) data points that should be identical on 6(statistics) x 6(spheres) x 5(dates) x 2(thresholds) = 360 occasions. With only 8 data points for each of these occasions there is no robust statistical analysis available, but still a large volume of data to assess. The clearest way to assess equivalence was to plot the data.

The data was separated by statistic (mean, SD etc.) with one graph for each RECIST threshold (10% and 40%). Each sphere (labelled ‘a’ through ‘f’), on each graph, has 5 distinct dots of different colours. These are the “occasions”. There are 8 data points from the exam types that should overlay each other exactly. Deviation from this would change the appearance of the expected single, un-spread point. If they maintain this appearance, the data is essentially identical and the exam type

has no significant influence on the results for this study. An example of this for the volume of the VOIs is displayed in **Figure 4-5**, all others are in Appendix I.

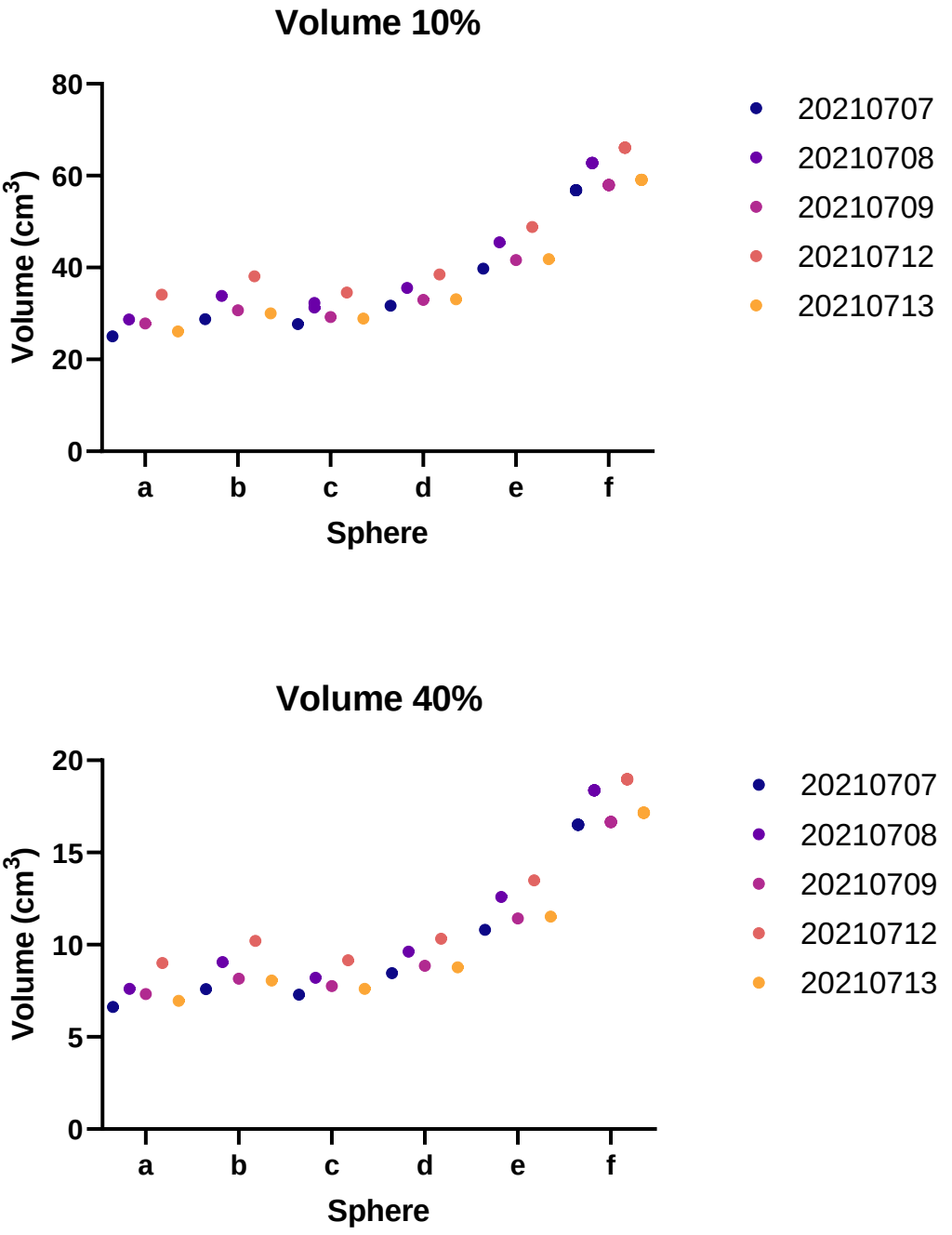

Figure 4-5 *Syngo.Via provided statistic Volume for 10 and 40% RECIST thresholds. Each coloured dot contains the Syngo.Via provided volume for all 8 different exam types for a single sphere on a single date. As all dots appear unsmeared, this confirms that a change in exam type during reconstruction does not alter the Syngo.Via statistic, Volume in this figure. This also does not change with a higher or lower RECIST threshold.*

After this visual analysis all results were reviewed and found to be identical, confirming the exam type exerts no influence on the results. Once eliminating exam type as an influence, the Syngo.Via statistics were examined.

4.3.1.2 Syngo.Via Statistics

All activity-based statistics (Max, Mean, Threshold, SD and Peak) are presented in concentration form as kBq/ml, rather than activity. Since the spheres were filled with a solution of known concentration in kBq/ml, the Syngo.Via results were able to be directly compared when assessing the accuracy of each activity-based statistic. Activity in kBq is addressed in section 4.3.3.

The primary method for determining accuracy is comparing test results from one method, to the values achieved from a method that is accepted as accurate. In this case, the method accepted as accurate is the sphere solution concentration from the well counter with applied decay correction. There are multiple comparisons with these accepted as accurate results, in the form of Syngo.Via statistics with different RECIST thresholds. Changing the RECIST threshold changes the Mean but does not affect the Peak and Max. This is expected as the Peak and Max only consider the centre of the sphere where the highest readings would be achieved.

When comparing methods to the accepted standard, a linear regression was graphed using Prism. The closer the equation resembled y = x, the higher the accuracy. However, it is expected the smaller the sphere, the less accurate the concentration results become.

Ideally, the intensity of each pixel in a SPECT image would be proportional to the amount of radioactivity within the corresponding volume. Even with attenuation and scatter corrections, error in assigning activity values remains for small volumes. A SPECT system has a characteristic resolution volume dependant on its x-y and z resolutions. For sources and measurements smaller than this resolution volume, if all the pixels attributed to that object were summed, the total activity would still be accurate. However, the concentration of the activity is no longer accurately reflected, since the counts are distributed over a volume larger than that of the actual source (Cherry et al. 2004). This is reflected in **Figure 4-4A** of the largest and smallest spheres. Both contain the same concentration of activity, yet the smaller the sphere, the further the RECIST contour deviates from the plastic sphere outline. Due to the Partial Volume Effect (PVE), each sphere was assigned its own linear regression, as seen in **Figure 4-6**.

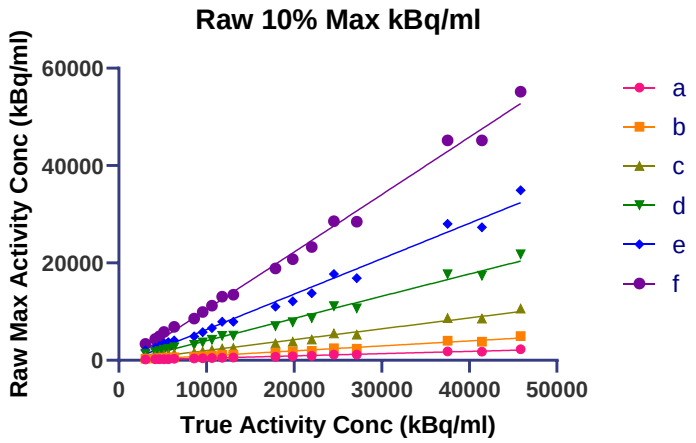

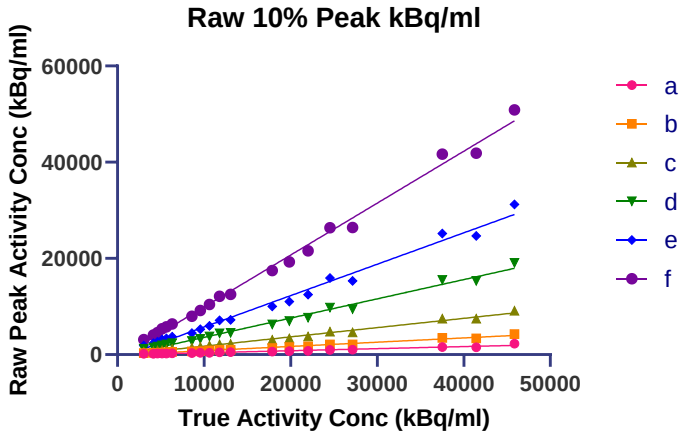

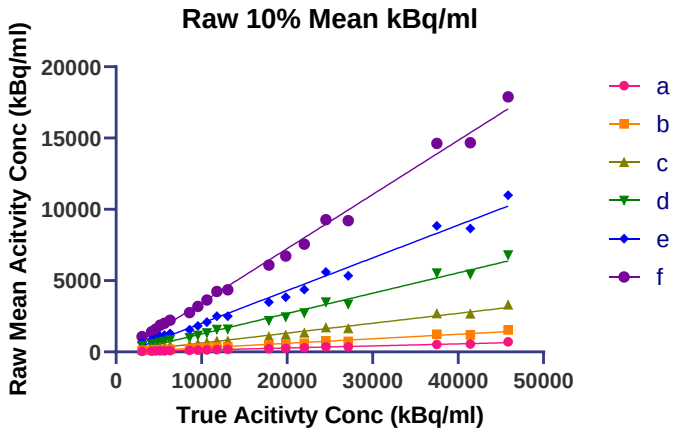

Figure 4-6 *Linear regressions of Raw Syngo.Via statistics Max, Peak and Mean for a 10% RECIST threshold with individual linear regressions assigned to each sphere. The smallest sphere is labelled a and the largest is labelled f. The y-axis ("Raw" activity concentration), refers to the measured activity concentration on the software. The x-axis ("True" activity concentration) refers to corresponding measured activity concentration from the well-counter. All activities are decay corrected.*

If the PVE was not a factor, there would be precision between the linear regressions for each sphere size, even if they all deviated from the desired $y = x$ (meaning they would be precise but not accurate). That is, data sets ‘a’ through ‘f’ would be overlayed, with a similar slope for each fitted line of regression. Instead, **Figure 4-6** displays how pronounced the PVE is, and its increase in severity with reducing the sphere size.

When choosing the statistic that produced the highest accuracy, each regression’s gradient, r-squared and root mean square error (Sy.x) was considered. The desirable criteria were minimal deviation of the gradient from unity, high r-squared and low root mean square error. As mentioned in section 3.3.2, the root mean square error uses standard deviation of the residuals to track how much the points vary from the calculated regression. It is larger and is a better estimate of goodness-of-fit than r-squared alone.

Deviation from linearity was tested for each regression as described in section 3.3.2. The only significant deviation from linearity, as indicated by the red framed P-value in **Table 4-3**, was for the Peak value of the smallest sphere. The Peak value is taken over a 1 cm^3 volume, with the VOI placed over the object of interest, such that the mean value is maximum. This 1 cm^3 is much larger than sphere ‘a’, creating more unpredictability and veering the data away from appearing linear.

Table 4-3 *Syngo.Via statistics linear fit with goodness of fit information.*

	Equation					
Sphere	a	b	c	d	e	f
Max	Y = 0.04640*X - 19.32	Y = 0.1022*X - 105.2	Y = 0.2233*X - 227.4	Y = 0.4563*X - 528.8	Y = 0.7279*X - 965.1	Y = 1.180*X - 1358
Peak	Y = 0.04283*X - 41.36	Y = 0.08867*X - 73.80	Y = 0.1928*X - 168.2	Y = 0.4005*X - 416.7	Y = 0.6530*X - 796.4	Y = 1.080*X - 900.4
Mean (10% RECIST)	Y = 0.01430*X - 6.904	Y = 0.03184*X - 32.63	Y = 0.06943*X - 70.12	Y = 0.1427*X - 163.3	Y = 0.2296*X - 292.4	Y = 0.3795*X - 345.4
Mean (20% RECIST)	Y = 0.01976*X - 9.434	Y = 0.04322*X - 43.33	Y = 0.09453*X - 95.16	Y = 0.1936*X - 221.6	Y = 0.3105*X - 403.3	Y = 0.5078*X - 464.4
Mean (30% RECIST)	Y = 0.02404*X - 10.91	Y = 0.05270*X - 53.75	Y = 0.1154*X - 118.8	Y = 0.2360*X - 275.5	Y = 0.3770*X - 494.8	Y = 0.6126*X - 553.6
Mean (40% RECIST)	Y = 0.02786*X - 12.36	Y = 0.06114*X - 62.74	Y = 0.1338*X - 138.6	Y = 0.2736*X - 329.8	Y = 0.4362*X - 573.4	Y = 0.7057*X - 625.0
	Deviation From Linearity P value					
Max	0.0767	0.3186	0.3186	0.3186	0.3186	0.6814
Peak	0.009	0.3186	0.3186	0.3186	0.3186	0.3186
Mean (10% RECIST)	0.3186	0.3186	0.3186	0.3186	0.3186	0.3186
Mean (20% RECIST)	0.0767	0.3186	0.3186	0.3186	0.3186	0.3186
Mean (30% RECIST)	0.0767	0.3186	0.3186	0.3186	0.3186	0.3186
Mean (40% RECIST)	0.0767	0.3186	0.3186	0.3186	0.3186	0.3186
	r-Squared					
Max	0.9881	0.9835	0.9884	0.9873	0.9855	0.9918
Peak	0.9666	0.9862	0.9903	0.9891	0.9872	0.9932
Mean (10% RECIST)	0.9909	0.9843	0.9889	0.988	0.9863	0.9927
Mean (20% RECIST)	0.9893	0.9838	0.9886	0.9877	0.9859	0.9925
Mean (30% RECIST)	0.9893	0.9837	0.9882	0.9876	0.9858	0.9927
Mean (40% RECIST)	0.9891	0.9835	0.9885	0.9874	0.9857	0.9925
	Sy.x					
Max	69.34	179.8	329	704	1202	1461
Peak	108.3	142.6	259.3	571.5	1013	1213
Mean (10% RECIST)	18.7	54.67	100.3	214.1	368.5	443.9
Mean (20% RECIST)	27.94	75.5	138.3	294	504.9	601.7
Mean (30% RECIST)	33.98	92.44	171.4	359.4	614.8	716.4
Mean (40% RECIST)	39.75	107.8	196.3	421.1	715.9	835.5

Peak and Max have the Minimum gradient deviation from one with similar values for each sphere regression. Based on the r-squared and the Sy.x, the peak was determined superior in its linear fits. The peak is used clinically, so it was selected as the Syngo.Via statistic to base further analysis on.

Once the statistic was chosen, PVE was addressed. This is crucial if using a quantification method based on actual volumes.

4.3.1.3 Partial Volume Correction

PVE in all cases reduces the contrast between areas of high activity concentration and those of low activity concentration, which leads to underestimation of concentration in the higher activity regions and overestimation of concentrations in surrounding background regions. This can be the dominant source of error in small structures during quantitative SPECT and requires addressing.

PVE can be corrected using a volume-based method. The correction of apparent concentration to true concentration is called the recovery coefficient (RC). Actual volumes of the objects may be used for this correction, which is common for phantom studies. This is still clinically relevant with accompanying CT information since CT has high resolution allowing definition of sizes of in vivo objects (Cherry et al. 2004; Dewaraja et al. 2012). The RC is strongly influenced by the data acquisition protocol and reconstruction, meaning experimentally determined RCs should be formed for the specific camera/collimator and acquisition/reconstruction (Ljungberg et al. 2016).

Commonly, the recovery coefficient comes in the form of **Equation 4-2**.

$$RC = 1 - ae^{-bVol}$$

Equation 4-2

where *a* and *b* are fitted parameters and *Vol* is the actual volume of the object (D'Arienzo et al. 2016; Willowson, Bailey & Baldock 2008). However, this implies the *RC* is capped at one. In some situations, it can be greater than one, when there is spill out from surrounding structures into the object of interest (Cherry et al. 2004).

Studies such as Finocchiaro et al. (2019) and Ramonaheng, van Staden and du Raan (2021) used a similar formula without this limitation, which was applied to this study, in the form of **Equation 4-3**.

$$RC = c - ae^{-bVol}$$

Equation 4-3

which replaces the 1 in **Equation 4-2** with fitted parameter c. Both studies discuss the limitation of volume-based *RC*. These corrections are based on spherical volumes, and while appropriate for objects of ellipsoid shape, it is not sufficient for more complex shapes. Finocchiaro et al. (2019) investigated the volume-based corrections application on more clinically relevant shapes. A phantom study with more complex shapes revealed sphere-volume-based RCs on non-sphere-shaped objects requires other input factors. While beyond the scope of this study, future work may consider incorporating extra factors such as surface area and compactness of the object in forming a RC as well as addressing object with inhomogeneous uptake.

4.3.1.3.1 Gradient RC

In mathematical terms, the goal of the RC is to transform all $y = mx + c$ equations in **Figure 4-6** (Raw Peak), to $y = x$. Transformation of m to 1 was first considered.

Each gradient was graphed with the associated sphere volumes in Prism (**Figure 4-7**) and **Equation 4-3** fitted. The resulting fit is listed in **Table 4-4**.

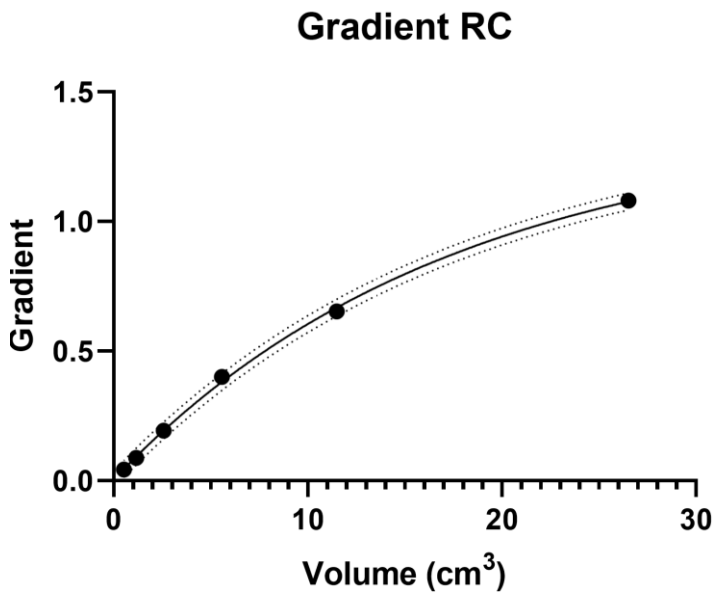

Figure 4-7 *Gradients from linear fits in* ***Figure 4-6*** *Peak plotted against the corresponding sphere volumes. Fitted with RC Equation 4-3. The 95% Confidence band is too close to the exponential fit to visualise but the 95% prediction band is visible and further indicates a good fit.*

Table 4-4 *Line of best fit data for Gradient RC in* ***Figure 4-7*** *Gradients from linear fits in* ***Figure 4-6*** *Peak plotted against the corresponding sphere volumes. Fitted with RC Equation 4-3. The 95% Confidence band is too close to the exponential fit to visualise but the 95% prediction band is visible and further indicates a good fit.*

Data for fit of y=c-a*exp(-b*x)	
Best-fit values	
c	1.374
a	1.369
b	0.05759
95% CI (profile likelihood)	
c	1.345 to 1.406
a	1.343 to 1.398
b	0.05507 to 0.06012
Goodness of Fit	
r-Squared	0.9981
Sum of Squares	0.02879
Sy.x	0.01610

Figure 4-7 displays the fit with prediction bands to visualise possible error. The prediction bands are more conservative than confidence bands. The 95% prediction band is the area in which you expect 95% of all data points to fall. In contrast, the 95% confidence band is the area that has a 95% chance of containing the true regression line (GraphPad 2022a). Based on the 95% prediction band and goodness of fit values in **Table 4-4**, the fit was deemed acceptable.

This formed the transformation of the gradient m, to the desired value of 1 when applied as in **Equation 4-4**.

$$PVC_{Peak} = \frac{Peak}{RC_{gradient}}$$

Equation 4-4

where PVC_{Peak} is the partial volume corrected peak in kBq/ml, *Peak* is the raw Peak value from Syngo.Via in kBq/ml and $RC_{gradient}$ is the RC based on the gradients with fitted factors listed in **Table 4-4**.

4.3.1.3.2 Intercept RC

The error on the fitted intercepts was too high for any fit to be reliable. The intercept ± error entered into Prism was taken as half the width of the 95% confidence interval of the fitted intercepts in **Table 4-5**. The resulting graph in **Figure 4-8** displays the error bars in the plot. The same was done for the gradient PVC fit but the errors were minor (detailed further, with all other uncertainties, in Appendix J).

Table 4-5 *Error bar information for* ***Figure 4-8****.*

Sphere	a	b	c	d	e	f
Y-intercept 95% CI	-127.5 to 44.78	-187.2 to 39.59	-374.4 to 38.03	-871.2 to 37.83	-1602 to 9.171	-1865 to 63.98
± Intercept Error	86.14	113.4	206.22	454.52	805.586	964.495

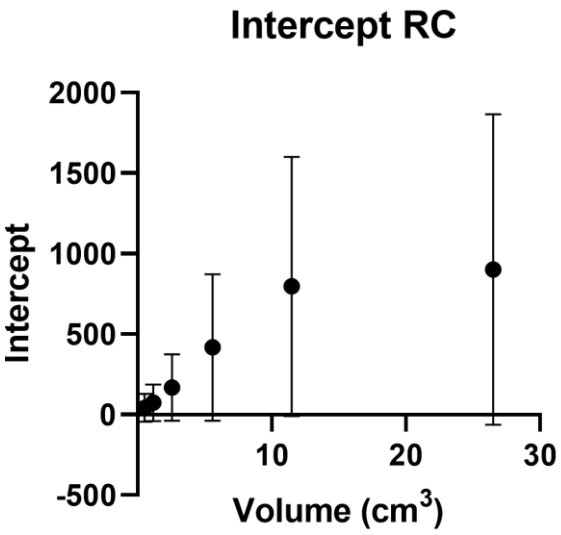

Figure 4-8 *Intercepts from linear fits in* ***Figure 4-6*** *plotted against the corresponding sphere volumes. The error bars indicate an extreme level on uncertainty making any RC derived from this data unreliable.*

This intercept transformation, had the error not excluded it, would have been a y-axis translation in the form of **Equation 4-5**.

$$PVC_{Peak} = \frac{Peak}{RC_{gradient}} - RC_{intercept}$$

Equation 4-5

where $RC_{intercept}$ is the RC based on an appropriate fit of data in **Figure 4-8**. This would have been in addition to the scaling of the $RC_{gradient}$.

4.3.1.3.3 RECIST Volume RC

RECIST volumes were investigated since they are readily clinically available. The data could not, however, be approached in the same manner as the actual sphere volumes. The data in **Figure 4-6** have a singular actual volume associated with each linear regression (one for each sphere). The RECIST volumes vary for each sphere, so the process of assigning each sphere its own regression in an attempt to use that fit and an associated volume does not translate here. Instead, the ratio of true (capintec derived) to RECIST measured (scanner derived) activity concentration was plotted in **Figure 4-9**. The 40% threshold volumes were used since the peak remains unchanged no matter the threshold, but this percentage best reflects the actual sphere volume.

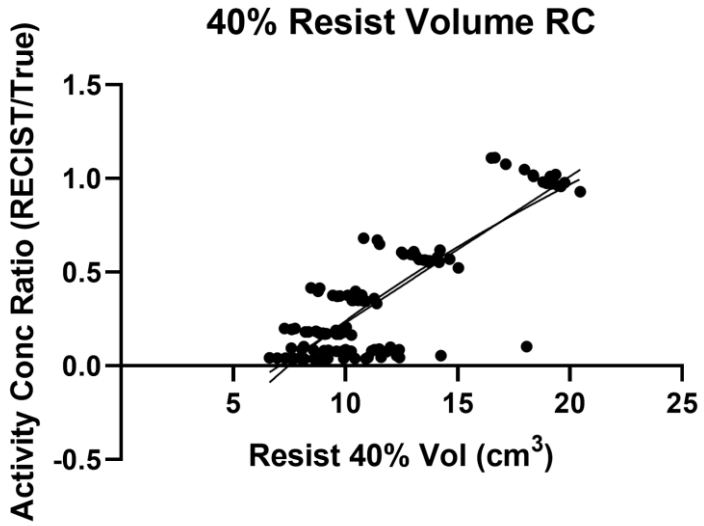

Figure 4-9 *Raw Peak activity concentration divided by the True activity concentration versus the corresponding Volume provided by Syngo.Via using a 40% RECIST threshold.*

The resulting data in **Figure 4-9** does not supply a cohesive trend to base a RC on.

An attempt to use the $RC_{gradient}$ using RECIST volumes was made and was unsuccessful since that RC is based on different volume associations. For this to be successful the RECIST volumes would need to closely resemble the actual volumes. The accuracy of the RECIST volume depends on the threshold, size of the object and the activity concentration. While beyond the scope of this study, future work may consider combining these factors to develop a RECIST-volume-based RC.

There are other PVC methods this study did not explore, some which are software based such as those discussed in the review of PVC by Erlandsson et al. (2012), but their implementation in clinical practice is limited due to their complexity (Dewaraja et al. 2012). Such PVC is beyond the focus of this study and the experimentally determined $RC_{gradient}$, was applied.

4.3.1.3.4 PVC Application

The $RC_{gradient}$ was applied to the Peak data and graphed in **Figure 4-10**. The precision has greatly improved alongside the accuracy. This is observed in the closeness of the graphs and the transformation of the gradients to approximately one seen in **Table 4-6**.

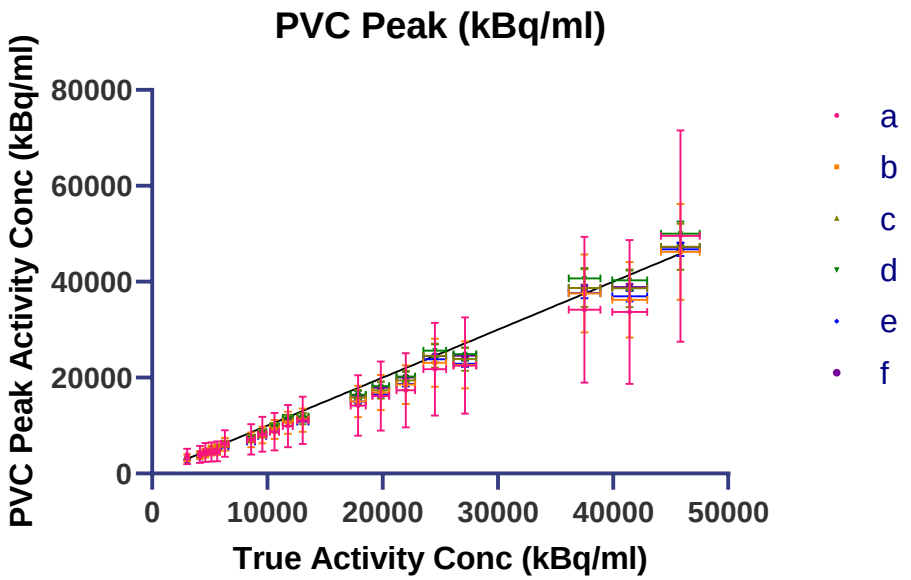

Figure 4-10 *XSPECT Lu-177 Peak Partial Volume Corrected activity concentration results (kBq/ml) versus the True activity concentration (kBq/ml). Results were corrected using RCgradient with factors from Table 4-4 in Equation 4-4. Each sphere is fitted with a linear regression to assess its accuracy.*

Table 4-6 *Linear equations with goodness of fit information for* ***Figure 4-10****.*

Sphere	a	b	c	d	e	f
Equation	Y = 0.9379*X - 905.7	Y = 0.9559*X - 795.6	Y = 0.9965*X - 869.2	Y = 1.051*X - 1094	Y = 0.9778*X - 1193	Y = 1.003*X - 836.2
r-Squared	0.9666	0.9862	0.9903	0.9891	0.9872	0.9932
Sy.x	2372	1537	1340	1500	1517	1126

This PVC correction would only be recommended for interpolating, not extrapolating beyond the investigated volumes.

To summarise, the chosen Syngo.Via statistic, Peak, required a PVC in the form of a RC. The aim of the RC was to transform the raw activity concentration to a more accurate representation of the true activity concentration. Multiple RCs, based on different factors were considered. Use of the RECIST volumes, while clinically relevant, was beyond the scope of this study as its use would require incorporating multiple other factors to make it viable. The gradient and intercept from the raw Peak linear fits were considered with only the gradient being viable due to the high level of uncertainty in the intercepts. The gradients were used in combination with the actual volume of the spheres to form the $RC_{gradient}$. The application of the $RC_{gradient}$ showed improved accuracy and precision in the results for sphere concentration.

4.3.2 3D Flash Manual Quantification

The same PVC method was applied to 3D Flash reconstructed data, but with prior extra steps to have the data in activity concentration form, rather than counts. Since 3D Flash reconstructed results are in terms of counts, this needed to be converted to activity concentration in kBq/ml. The Peak activity concentration (Peak kBq/ml) remained the chosen Syngo.Via statistic for all results.

Clinically, for quantitative imaging, the point source method detailed in section 3.1.2.2, converts counts to activity. Instead, a calibration curve to convert counts to activity concentration in kBq/ml was formed using the bottle phantom as discussed in section 4.2.2. The relationship is still assumed to be linear, except based on multiple data points and not forced through (0,0) as assumed with the point source method.

Each image had 3 VOI selected as seen in **Figure 4-11**, which fit the criteria discussed in section 4.2.2.

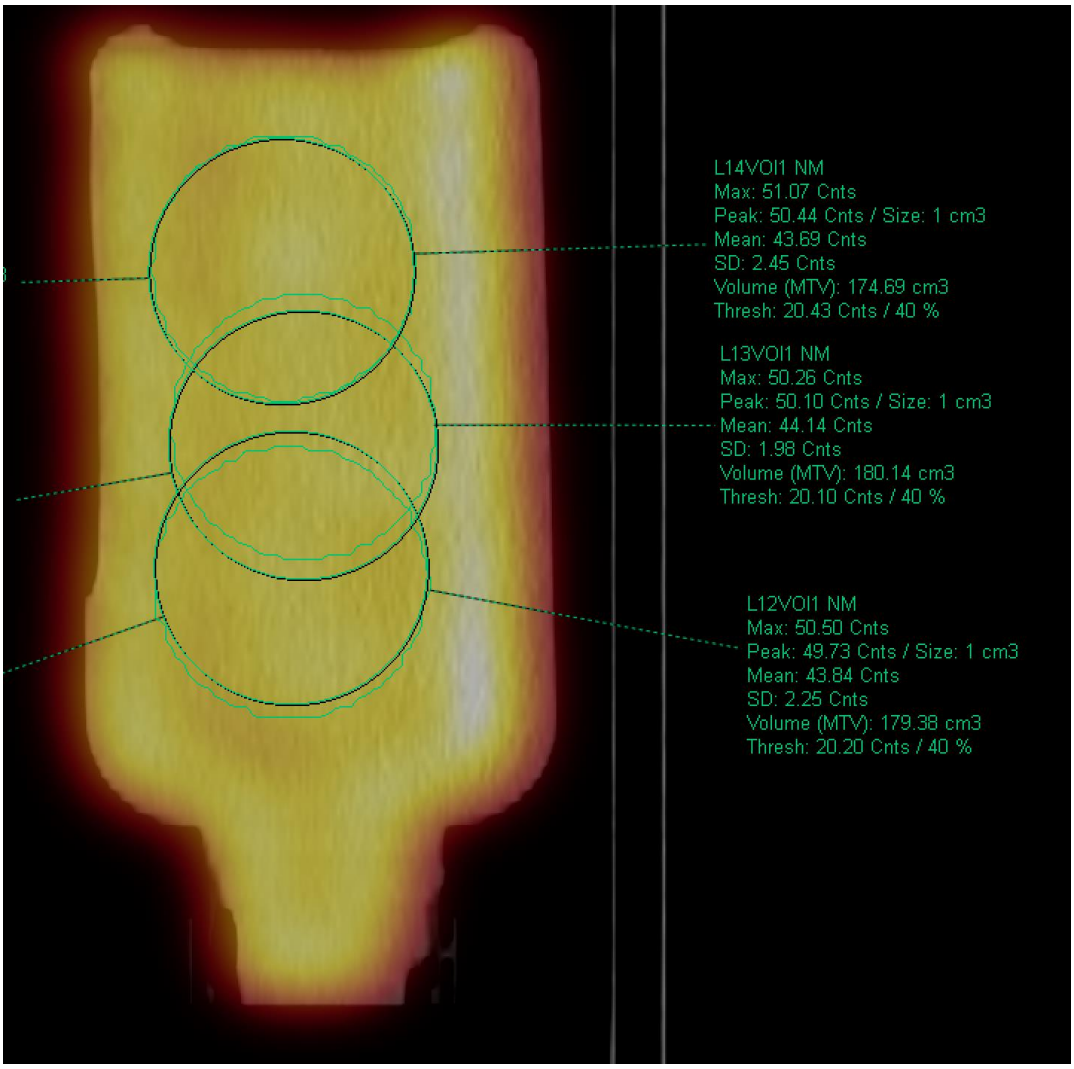

Figure 4-11 *A sample Bottle Phantom image from Syngo.Via. The VOIs are selected in the centre of the phantom to avoid the effects of spill in or out. Three VOIs are selected so an average Peak value may be used for each data point in the following bottle calibration curve.*

Since the acquisition parameters are identical to that for the NEMA phantom, this meant stop conditions were set to counts per view. While helpful for reducing counts as a reason for varied

image quality, it does mean that the total counts are very similar between images despite varied activity. If using the clinical protocol, stop conditions as time per view, the number of counts would vary with the activity. For this study, time to acquire instead of the number of counts varies with activity. The counts and actual frame duration from the DICOM header (tag 0018, 1242) formed count rate. The three resulting count rates per image were averaged and graphed against the known activity concentration to form the calibration curve, **Figure 4-12**.

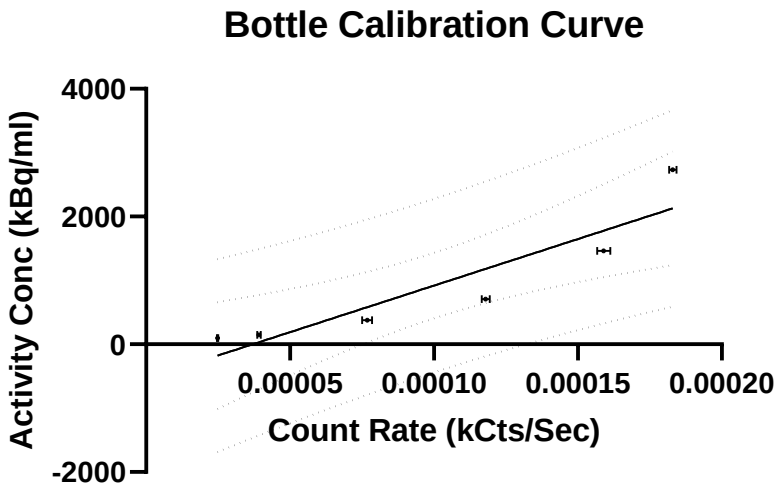

Figure 4-12 *Bottle Calibration Curve to convert count rate in kCts/Second to activity concentration in kBq/ml. Each point is the average of three VOI collected for each image taken of the Bottle Phantom, as depicted in the previous Figure 4-11. Despite the wide 95% confidence and prediction bands, the linear regression fitted to this data was still the most appropriate fit.*

Table 4-7 *Linear equation with goodness of fit information for Figure 4-12.*

Equation	Y = 14579555*X - 539.3
r-Squared	0.8421
Sy.x	452.8

Figure 4-12 contains wide 95% confidence and prediction bands. Nonlinear fits were attempted with improved r-squared and Sy.x but had poor results when used to convert count rate to activity concentration. The linear fit in **Table 4-7** yielded the most accurate results. While a nonlinear fit may appear appropriate, this does not accurately reflect the known relationship between the Peak activity concentration and count rate. This is why the attempted nonlinear fits produced highly inaccurate results.

4.3.2.1 3D Flash PVC

The converted concentration results had PVC applied in the same manner as the XSPECT results. A RC was formulated from the converted concentration data using the same method detailed in section 4.3.1.3.1.

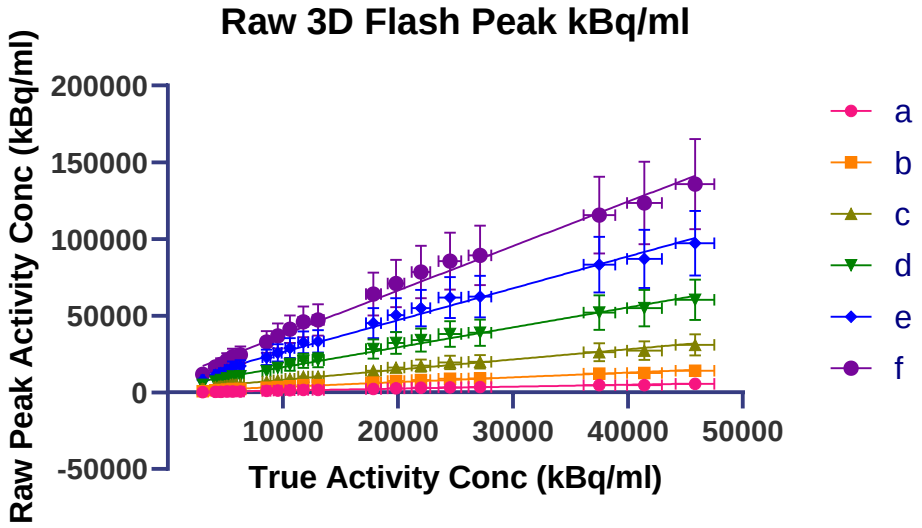

Figure 4-13 *Raw 3D Flash reconstructed Peak activity concentration data versus the True activity concentration. Each sphere has its own linear regression fitted to assess accuracy.*

Table 4-8 *Linear equations with goodness of fit information for Figure 4-13.*

Sphere	a	b	c	d	e	f
Equation	Y = 0.1260*X - 99.83	Y = 0.3106*X + 446.9	Y = 0.6647*X + 1460	Y = 1.299*X + 3368	Y = 2.077*X + 5457	Y = 2.899*X + 8299
r-Squared	0.9860	0.9874	0.9881	0.9898	0.9902	0.9900
Sy.x	204.5	476.5	993.8	1797	2816	3958

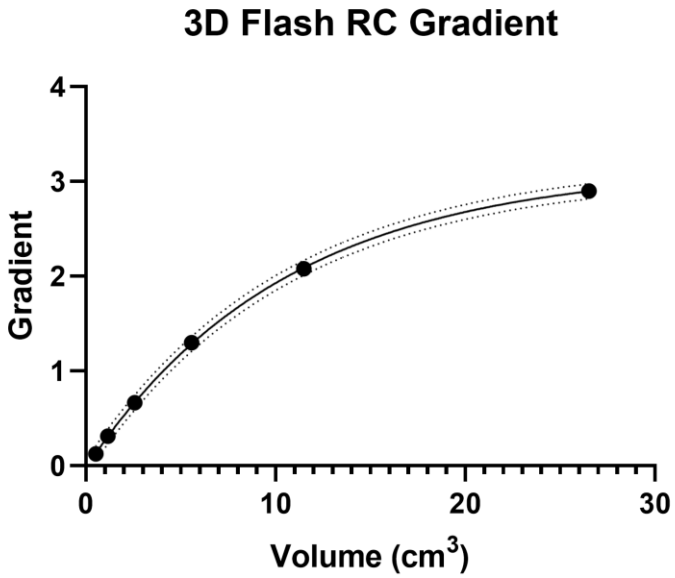

Figure 4-14 *Gradients from linear fits in Figure 4-13 plotted against the corresponding sphere volumes. Fitted with RC Equation 4-3. The 95% Confidence band is too close to the exponential fit to visualise but the 95% prediction band is visible and further indicates a good fit.*

Table 4-9 *Line of best fit for 3D Flash RC Gradient data in Figure 4-14.*

y=c-a*exp(-b*x)	
Best-fit values	
c	3.148
a	3.171
b	0.09543
95% CI (profile likelihood)	
c	3.116 to 3.181
a	3.141 to 3.201
b	0.09290 to 0.09798
Goodness of Fit	
r-Squared	0.9985
Sum of Squares	0.1681
Sy.x	0.03892

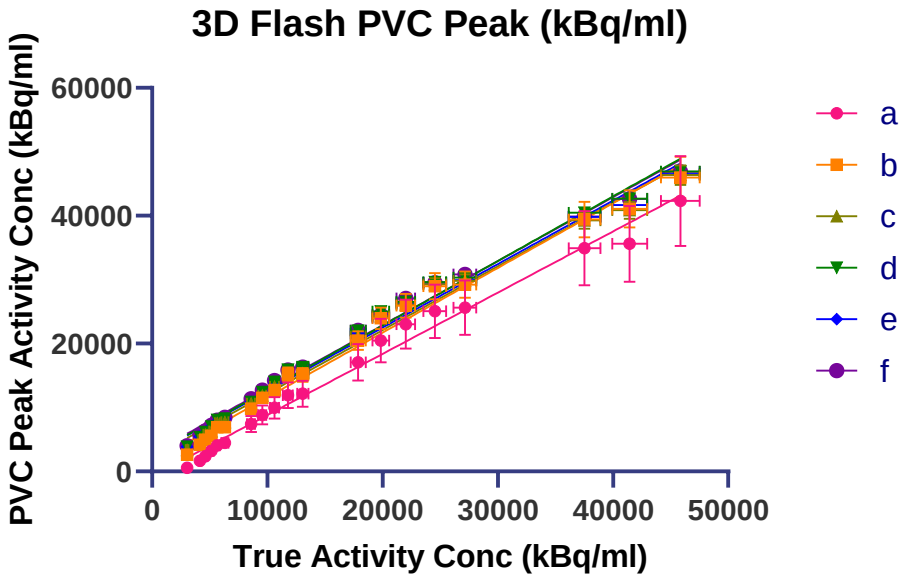

Figure 4-15 *3D Flash Lu-177 Peak Partial Volume Corrected results versus the True activity concentration. Results were corrected using* $RC_{gradient}$ *with the results from Table 4-9 in Equation 4-4. Each sphere is fitted with a linear regression to assess its accuracy.*

Table 4-10 *Linear equations with goodness of fit information for data in Figure 4-15*

Sphere	a	b	c	d	e	f
Equation	Y = 0.9576*X - 758.7	Y = 1.013*X + 1457	Y = 0.9962*X + 2189	Y = 1.010*X + 2621	Y = 0.9941*X + 2612	Y = 1.001*X + 2866
r-Squared	0.9860	0.9874	0.9881	0.9898	0.9902	0.9900
Sy.x	1555	1554	1490	1398	1348	1367

Prior to PVC, as seen in **Figure 4-13** and **Table 4-8**, the results were further from the ideal y = x than the comparable XSPECT data in **Figure 4-6 Peak**. The 3D Flash $RC_{gradient}$ has small 95% prediction bands, and desirable goodness of fit values, just as $RC_{gradient}$ for XSPECT did. The PVC, as seen in **Figure 4-15** and **Table 4-10**, was successful with the gradients now close to unity.

The VOI results for the 3D Flash reconstruction are not in units of kBq/ml, rather they are counts. Since the stop conditions were set to counts per view, all count results were very similar. Instead, count rate (in kCts/sec) were used. To convert the count rate to activity concentration in kBq/ml, a

calibration curve was created. Scanning a known activity concentration was required to create the calibration curve, for which a bottle phantom was repeatedly scanned. The chosen bottle was able to meet the homogeneity, margin and extrapolation requirements for reliable activity concentration data. Once the results were converted to kBq/ml, a PVC was applied. The PVC was formulated using the same methods as that for the XSPECT results, using $RC_{gradient}$. The application of the $RC_{gradient}$ showed improved accuracy and precision in the activity concentration, as it did for the XSPECT results.

Currently, all the results have been in terms of activity concentration (kBq/ml), however analysis of the activity was still required to draw useful clinical conclusions.

4.3.3 Comparison of Activity Based Results

While previous sections discussed results in terms of concentration, activity in each sphere was still addressed. While PVC activity concentration is the most accurate in terms of concentration, the uncorrected activity concentration combined with various RECIST volumes still produce reasonable activity (kBq) results. All activity concentration and volume combinations were trialled. The results were normalised to the true activity concentration and compared in **Figure 4-16** via boxplot.

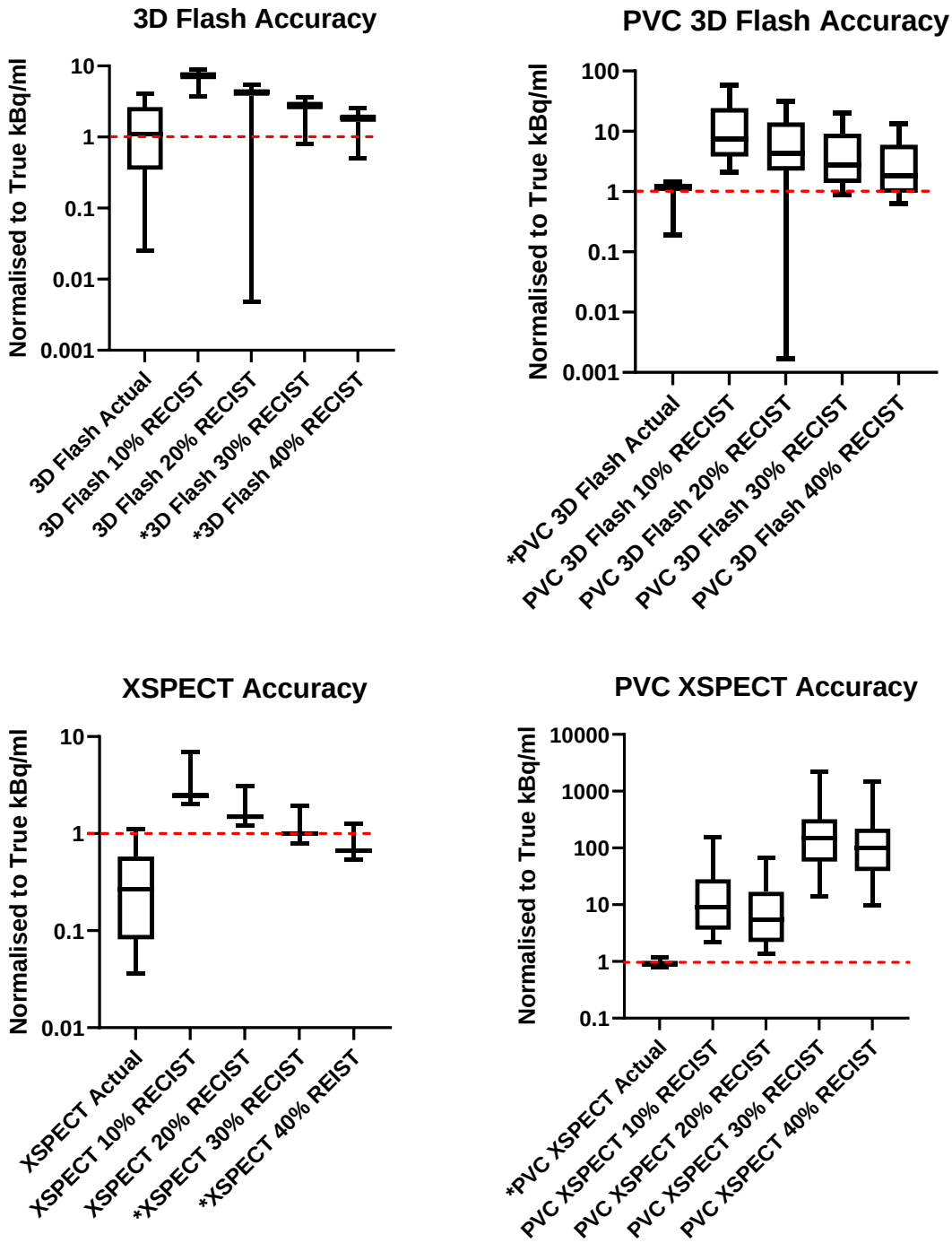

Figure 4-16 *Box plots of results normalised to the True activity concentration (True kBq/ml) for all volume and concentration combinations for activity (kBq) results. Each graph is separated by the reconstruction and correction applied (PVC). The smaller the box plot and the closer it lies to 1, the better the accuracy of those results.*

Each graph represents one data set combined with all possible volumes. PVC activity concentration have the most accurate results in combination with actual volumes, as that is the basis of the PVC. The raw activity concentration is most accurate combined with 30 or 40% RECIST volumes. This is expected since PVC activity concentration data (as described in section 4.3.1.3) is based entirely on the actual volumes of the spheres. To combine it with anything that deviates from the actual volume

will not produce accurate results. Likewise, to combine raw activity concentration results with volumes that do not reflect how Syngo.Via determined the data will not produce accurate results. The results marked with an asterisk (*) were the closest to the ideal (1). The comparison of these chosen combinations in **Figure 4-17** allows clearer visualisation of these choices.

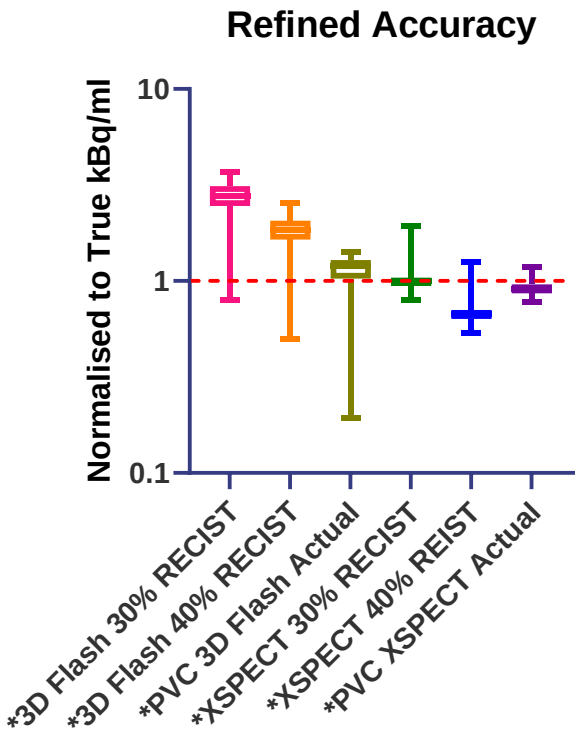

Figure 4-17 *Box plots of results normalised to True activity concentration (True kBq/ml) for the selected most accurate volume and concentration combinations for activity (kBq) results; 3D Flash 30% RECIST, 3D Flash 40% RECIST, PVC 3D Flash Actual, XSPECT 30% RECIST, XSPECT 40% RECIST and PVC XSPECT Actual. The smaller the box plot and the closer it lies to 1, the better the accuracy of those results. The XSPECT results have the smaller range and IQR than the 3D Flash, better meeting the desirable criteria.*

The chosen combinations in **Figure 4-17** generally show the XSPECT (automated quantification) results as superior to 3D Flash (manual quantification) due to the smaller range, smaller Interquartile Range (IQR) and closeness of their median to 1. Further quantitative analysis of the results in **Figure 4-17** showed which combination was most clinically beneficial.

All chosen combinations were plotted against the true activity values and fitted with a linear regression. Accuracy and precision were the desired outcomes, making the desirable properties: high r-squared, low Sy.x, a regression close to y = x and a small standard deviation of residuals. The residuals refer to the calculated activity minus the known activity. Visually, the closer and more consistently the residuals lie to 0, the closer they reflect the true activity, and this is quantitatively reflected in a smaller standard deviation of the residuals. The standard deviation of the residuals calculates how much the data points spread around the regression line $y = x$. These results are listed in **Table 4-11**.

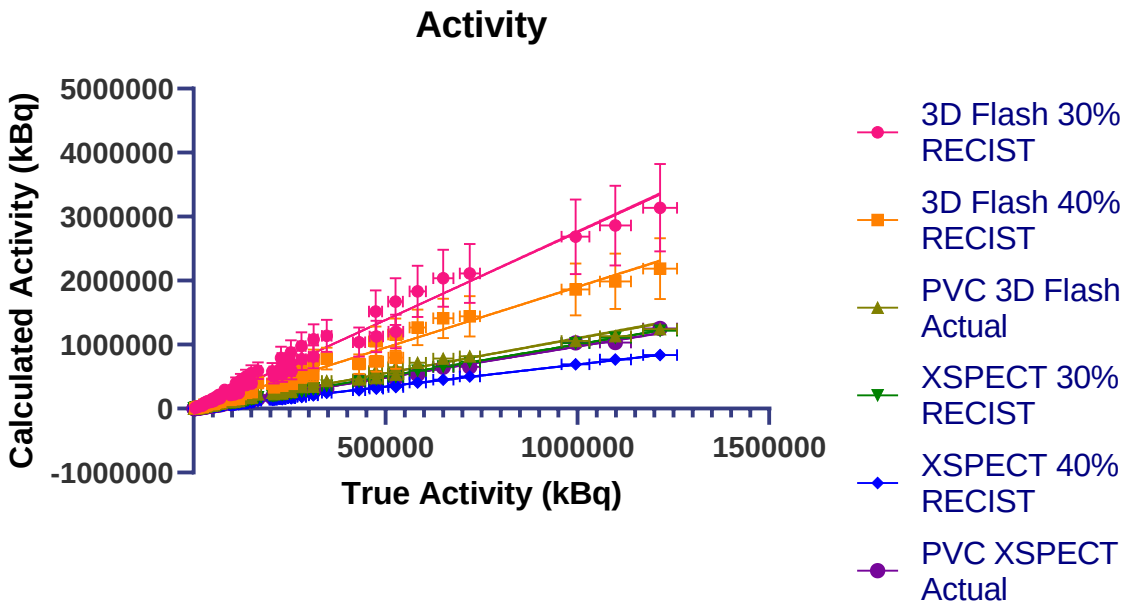

Figure 4-18 *Linear regressions for the selected most accurate volume and concentration combinations for activity results; 3D Flash 30% RECIST, 3D Flash 40% RECIST, PVC 3D Flash Actual, XSPECT 30% RECIST, XSPECT 40% RECIST and PVC XSPECT Actual. The closer the fit to y = x, the better the accuracy.*

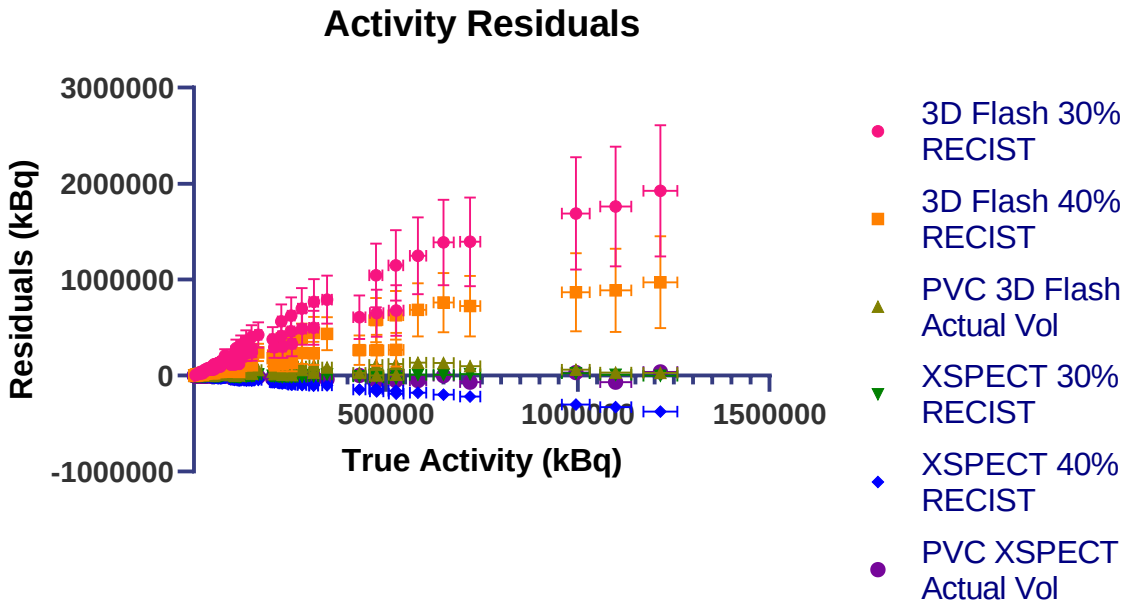

Figure 4-19 *Residuals for the selected most accurate volume and concentration combinations for activity results; 3D Flash 30% RECIST, 3D Flash 40% RECIST, PVC 3D Flash Actual, XSPECT 30% RECIST, XSPECT 40% RECIST and PVC XSPECT Actual. The closer the residuals to zero, the more accurate the results.*

Table 4-11 *Linear equations, goodness of fit information and standard deviation of the residual with respect to y = x for the data in Figure 4-18*

	3D Flash 30% RECIST	3D Flash 40% RECIST	PVC 3D Flash Actual	XSPECT 30% RECIST	XSPECT 40% RECIST	PVC XSPECT Actual
Equation	Y = 2.743*X + 13103	Y = 1.894*X + 5633	Y = 1.086*X + 9801	Y = 1.006*X - 1422	Y = 0.6918*X - 1673	Y = 0.9756*X - 4314
r-Squared	0.9825	0.9805	0.9893	0.9991	0.9988	0.9947
Sy.x	80364	58595	24818	6736	5214	15608
Residual Std Dev	389119	203908	30998	6854	67538	16426

Based on results in **Table 4-11**, the most suitable combination is XSPECT 30% RECIST with a close second in PVC XSPECT Actual. This is important to note since clinically, a 40% threshold is usually set.

While different thresholds could be used depending on the object actual size and activity, as discussed in section 4.3.1.3.3, this is beyond the scope of this study, whose aim is to find the best all-inclusive option. Minimal “rules” allow for simple clinical application. The size of the spheres is relevant to both mCRPC and NET since Lu-177 PSMA and octreotate are ideal for smaller wide spread disease due to the range of the beta particles, as discussed in chapter 1.

The PVC on the raw Peak activity concentration data successfully improved the accuracy and precision of the activity concentration for both the XSPECT and 3D Flash reconstructed results. However, activity per sphere, rather than activity concentration, still needed to be considered to produce clinically applicable advice. Volumes and concentrations were multiplied to produce activity values. All combinations of volumes, actual and RECIST produced, were combined with the PVC and raw peak activity concentration values for both 3D Flash and XSPECT reconstructions. The XSPECT raw Peak activity concentration with 30% RECIST volume produced the overall most accurate results.

The design of this phantom study aimed to closely replicate clinical activities so the results could be used to provide advice for the clinical environment. Based on these results, it would be advised to change the RECIST threshold commonly used in clinical practice from 40 to 30%. Additionally, the design of this study facilitated investigation into the effects the background concentration may have on the results.

4.3.4 Background Effects

The study was designed to cover a wide range of background to sphere concentrations for clinical relevance as detailed in section 4.1.3. To determine the effect of the background on accuracy, the data was initially grouped by sphere size since the effect of the background was suspected to be more severe on smaller objects. This is owing to the PVE being more pronounced when considering smaller objects as addressed in section 4.3.1.3. Only the most accurate combination, XSPECT 30% RECIST, was examined.

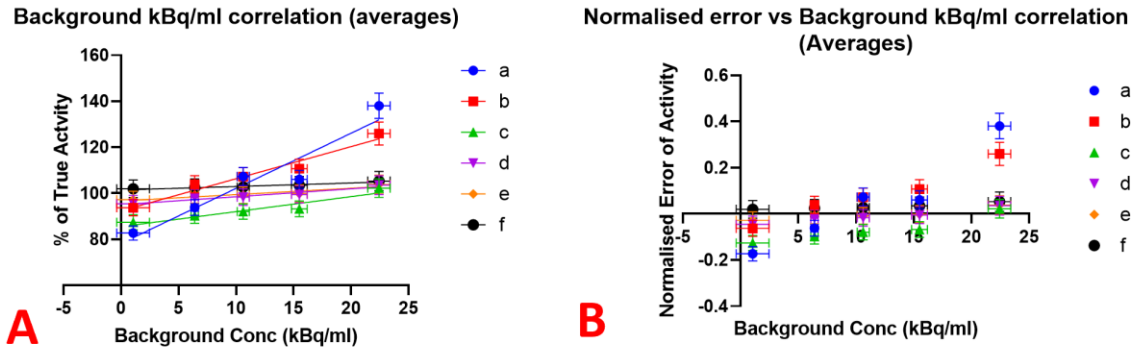

***Figure 4-20 A**. Percentage accuracy for similar background concentrations versus the background concentration with fitted linear regression. Each point is the average of data with different sphere concentrations but the same background concentration, either 1, 6, 10 or 20 kBq/ml. The data is split by sphere size, the smallest labelled a, the largest labelled f. The closer the linear fit is to y = 100, the less that sphere is affected by the background concentration.*

***B.** Normalised error versus the background concentration. Each point is the average data with different sphere concentrations but the same background concentration, either 1, 6, 10 or 20 kBq/ml. The data is split by sphere size. The closer the points to 0, the less that sphere is affected by the background concentration.*

The percentages of the true activity were graphed, rather than the absolute difference between the calculated and true activity, to make the results comparable. Each point is the average of that sphere for a similar background concentration (approximately 1, 6, 10, 15 and 20 kBq/ml). Each average is comprised of 3 to 5 data points. The points that comprise these averages have a range of activity (low to high) with the aim of negating the possibility that any correlation seen would be due to sphere activity, rather than background. Fewer visible points on the graph allow for clearer interpretation while still holding the weight of a larger volume of data.

Each sphere appeared to contain a positive trend in activity that increased with background concentration, so linear regression was fitted for each sphere. The closer the graph resembled y = 100, the less the backgrounds influence. The ideal is a gradient of 0 and intercept of 100. The fits are listed in **Table 4-12**.

***Table 4-12** Linear equations and goodness of fit information for data in Figure 4-20A. The smallest sphere is 'a' and the largest is 'f'.*

	a	b	c	d	e	f
Equation	Y = 2.396*X + 78.16	Y = 1.394*X + 92.38	Y = 0.6517*X + 85.50	Y = 0.3445*X + 95.04	Y = 0.2761*X + 96.65	Y = 0.1523*X + 101.4
r-Squared	0.8605	0.8454	0.6403	0.3551	0.2560	0.09401
Sy.x	7.241	4.475	3.667	3.484	3.532	3.549

The equation with the largest gradient is for the smallest sphere, a, and its intercept is the furthest from 100. This is consistent with the expectation that the most pronounced effect of the background concentration is on the smallest spheres. For large spheres activity accuracy is less affected by background concentration. The normalised error plot, **Figure 4-20B**, affirms this. When considering the activity based on peak values, the central 1cm^3 is far from the background for larger spheres so the loss and gain from scatter out and in has less effect on the result. This is not to imply there is no effect on the largest spheres.

Future work may be aimed at determining the exact object size for which background concentration effects should be accounted for and a possible correction. This could be done by adding another parameter to the already suggested future work discussed in section 4.3.1.3.3. This adds to the clinical relevance since background can vary for a multitude of reasons. Differing uptake from organ

to organ for each radiopharmaceutical or differing uptake to tumours in close proximity are just a couple of examples. This is important for dosimetry with a large number of small lesions in the vicinity of such objects.

Raw percentages of the true activity were also graphed in **Figure 4-21**. The resulting linear regressions have the same result, the smallest sphere with the largest gradient and the intercept furthest from 100, in **Table 4-13**. The correlation coefficient is much smaller since the sphere concentration increases scatter of the points.

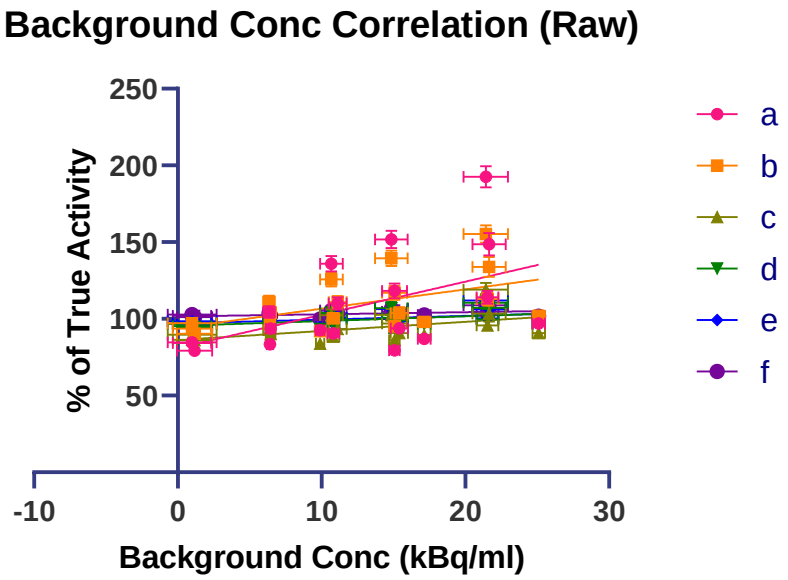

Figure 4-21 *Unaveraged percentage of true activity (kBq) versus Background concentration (kBq/ml) with linear regressions for each sphere size. The data is split by sphere size. The closer the linear fit is to y = 100, the less that sphere is affected by the background concentration. The smallest sphere is 'a' and the largest is 'f'.*

Table 4-13 *Linear equations and goodness of fit information for data in Figure 4-21.*

	a	b	c	d	e	f
Equation	Y = 2.161*X + 81.04	Y = 1.260*X + 94.02	Y = 0.5936*X + 86.21	Y = 0.3111*X + 95.45	Y = 0.2450*X + 97.03	Y = 0.1368*X + 101.6
r-Squared	0.2751	0.2689	0.2615	0.2270	0.1683	0.1906
Sy.x	26.52	15.70	7.541	4.340	4.117	2.131

Use of the averages removes the effect of the sphere concentration and plotting the raw values does not reveal its influence either. To address the role of sphere concentration in the background effect while maintaining comparability of results, the normalised error was plotted as a function of the background to sphere ratio in **Figure 4-22**.

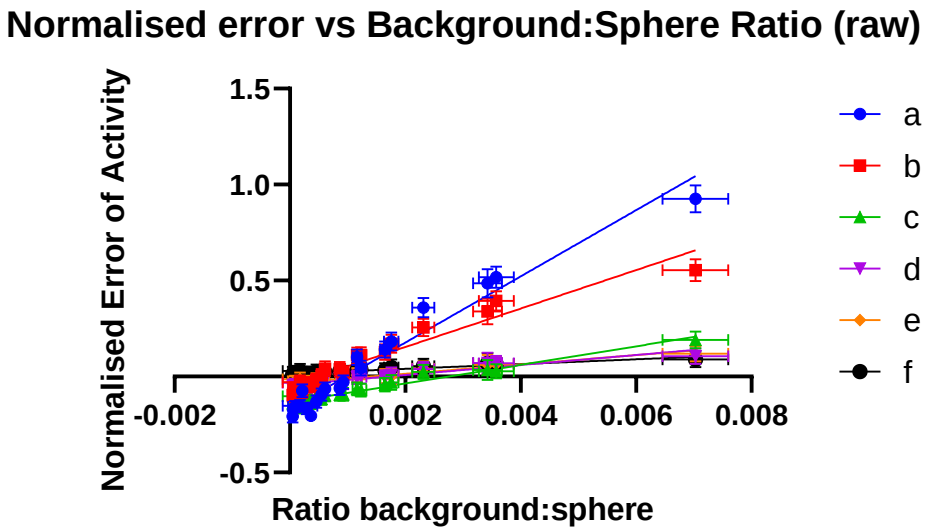

Figure 4-22 *The normalised error of activity vs Ratio of the background to sphere concentration with linear fits for each sphere size. This ratio was used to address sphere concentration's role in the background effect while maintaining comparability of results. Normalised error of zero is desired.*

Again, the smallest spheres are the most severely affected. When looking at the raw data in **Table 4-14**, all sections display the same trend with varying degrees of strength; the larger the sphere concentration, the lower the percentage of true activity. The strongest example is sphere 'a' with a 21 kBq/ml background highlighted in **Table 4-14** by a red box.

Table 4-14 *Percentage of actual activity for all combinations of background and sphere concentrations.*

	Background (kBq/ml)	Sphere (kBq/ml)	Percentage of True Activity (Uncorrected 30% RECIST Vol)					
			a	b	c	d	e	f
	1.16	24528	79.2	90.3	86.1	94.5	96.2	101.1
	0.99	11783	84.3	93.6	86.3	95.3	96.9	101.9
	0.99	5661	84.8	97.2	89.8	96.7	98.5	102.8
Average	1.05	13991	82.7	93.7	87.4	95.5	97.2	102.0
	6.41	22018	83.5	96.3	87.5	95.7	96.9	101.5
	6.46	10616	93.6	104.1	90.2	98.8	98.8	102.2
	6.34	5148	104.4	111.2	93.0	100.0	102.2	103.6
Average	6.40	12594	93.8	103.8	90.2	98.2	99.3	102.4
	9.90	45834	92.7	92.0	83.8	93.5	94.7	100.0
	10.82	19851	90.5	100.3	88.5	96.3	96.9	101.9
	11.12	9564	110.2	111.0	93.5	99.6	100.8	103.4
	10.69	4625	135.9	125.6	102.3	103.8	104.1	105.5
Average	10.63	19969	107.3	107.2	92.0	98.3	99.1	102.7
	15.07	41443	79.5	95.0	86.2	93.8	96.0	100.8
	17.14	37528	86.9	98.1	89.4	96.6	98.3	102.5
	15.41	17885	93.9	103.8	90.6	99.0	98.4	102.7
	15.08	8586	118.2	117.1	97.0	100.8	100.1	104.7
	14.86	4154	151.8	139.5	102.7	107.0	106.5	106.5
Average	15.51	21919	106.1	110.7	93.2	99.5	99.9	103.5
	25.12	27146	97.1	101.8	90.7	96.9	97.0	101.9
	21.54	13079	114.1	112.8	95.7	99.6	100.2	103.3
	21.66	6322	148.6	134.0	103.4	107.1	106.1	106.9
	21.43	3049	192.5	155.4	119.1	110.5	111.9	108.9
Average	22.44	12399	138.1	126.0	102.2	103.6	103.8	105.3

This is further illustrated in **Figure 4-24**, a sample of the graphs of the sphere vs background kBq/ml. Each graph represents a separate sphere; however, the error bars indicate the percentage error. As the sphere concentration becomes less, the longer the error bars become for all sphere graphs. This is true for all graph sets (split by their background concentrations, so there is a set for 1, 6, 10, 15 and 21 kBq/ml, listed in Appendix K)

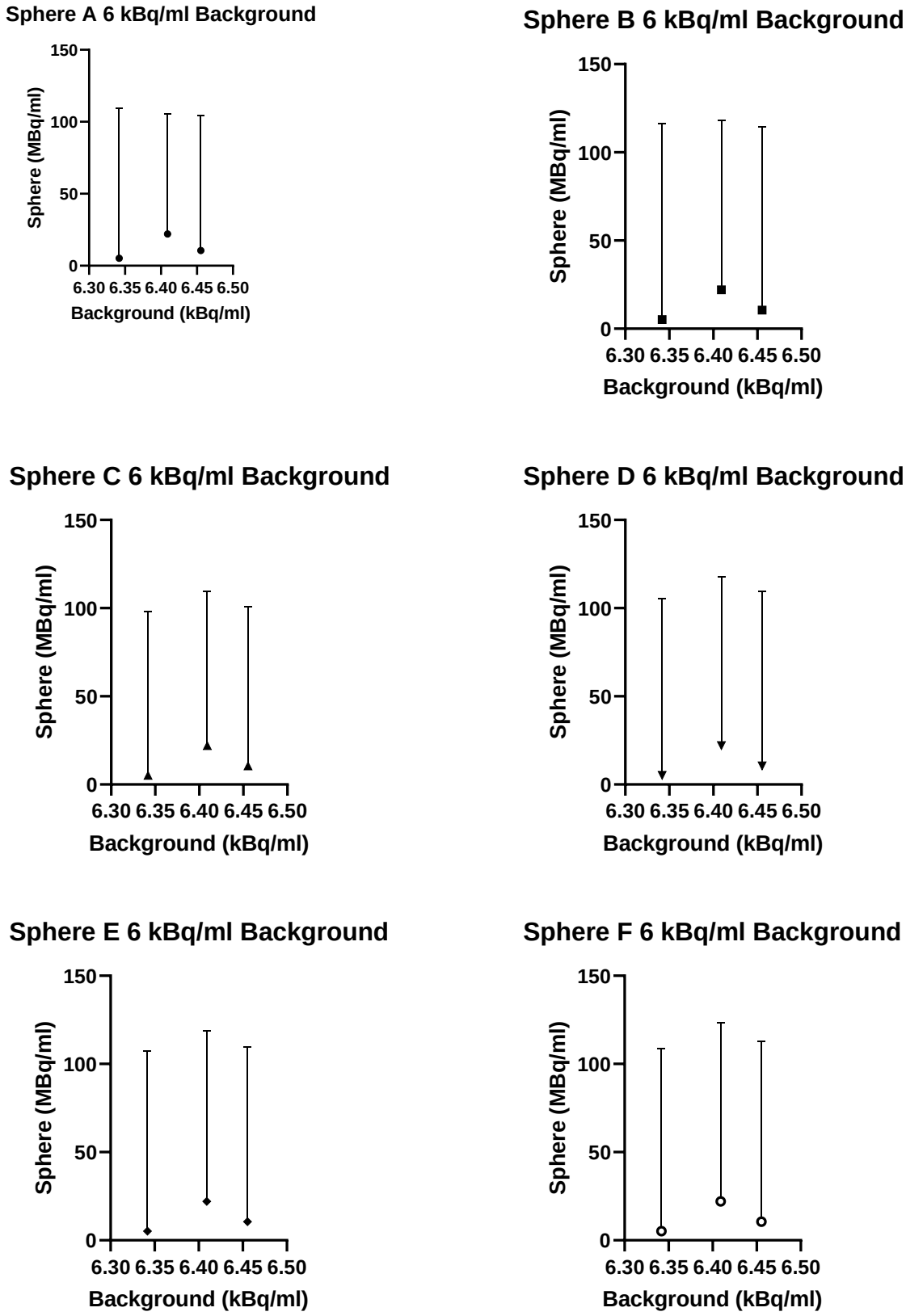

Figure 4-24 *Sphere concentration (MBq/ml) vs Background concentration (kBq/ml) for all sphere's ('a' through 'f') for a 6 kBq/ml background concentration. Each graph represents a separate sphere and the error bars are the percentage error. As the Sphere concentration decreases, the error bars become longer. Results for all other background concentrations are contained in Appendix K.*

After determining the most accurate activity results come from the raw Peak activity concentration values combined with a 30% RECIST threshold determined volume, the effect of background concentration was addressed. The study was designed to use clinically relevant activity concentrations in the background, based on a range blood concentration in patients. The background was found to influence the results. The severity of influence was found to have a correlation with sphere size, the smaller the sphere, the more acute the effect. The background to sphere concentration ratio was another important factor. The larger the ratio, the larger the effect of the background on the results. However, quantification and correction of these effects is beyond the scope and purpose of this study. As previously mentioned, future work would be needed to form and implement a correction for this which could be clinically relevant for reasons previously discussed.

4.3.5 Planar

The planar data has an output of counts rather than activity concentration in Syngo.Via. Much like the 3D Flash results, this required a conversion to count rate using the acquisition time from the DICOM header. Also similar to the 3D Flash, clinically the point source method is used when quantification is desired for planar. As an alternative this study used a calibration curve, also based on the bottle phantom, for a conversion to activity. However planar images were read using MI Reading instead of MM Oncology and data collection did not utilise a RECIST tool. Instead, the method of extracting results from Syngo.Via closely followed methods used clinically for estimating whole-body retention.

The images were windowed to reveal the spill out of counts after which regions of interest (ROIs) were manually drawn. To ensure the ROI were symmetrical, once a ROI was drawn, it was copied and inverted onto the opposing image where Syngo.Via would automatically place it in the same location as the first image, as shown in **Figure 4-25**.

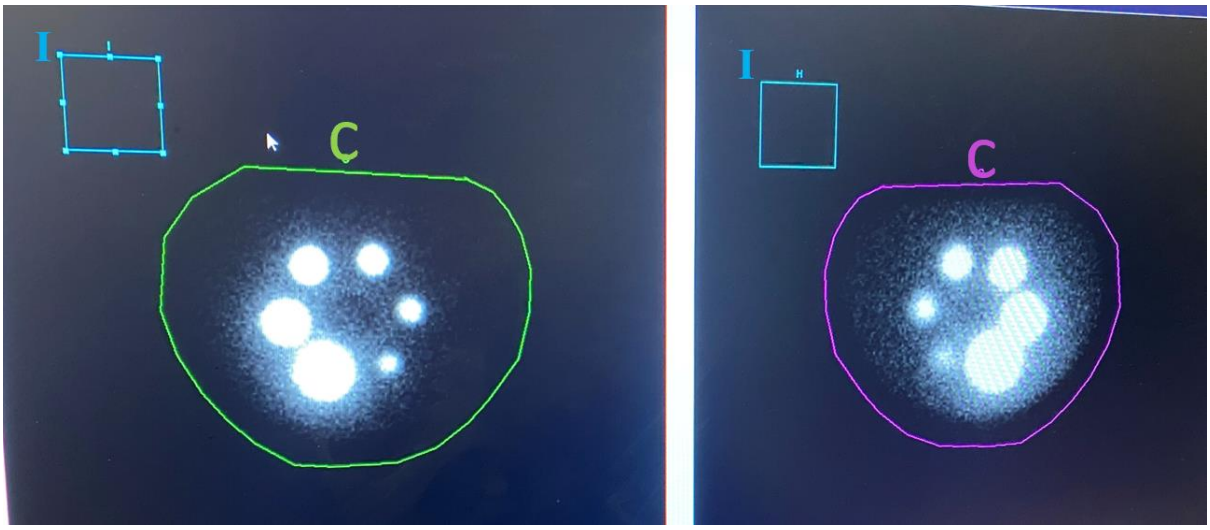

Figure 4-25 *Screenshot of Syngo.Via analysis of a planar image of the NEMA phantom. On the left, the anterior view with C the ROI drawn around the phantom and I the background ROI. On the right, the posterior view with mirrored ROI used on the phantom and background.*

Each ROI required background subtraction, using a smaller ROI towards the periphery of the FOV, and a conversion from counts to count rate using **Equation 4-6**.

$$CR = \frac{C_{Obj} - (C_{Back}\frac{P_{Obj}}{P_{Back}})}{Time}$$

Equation 4-6

where *CR* is the background corrected count rate, *Time* is the acquisition time taken from the DICOM header, C_{Obj} and C_{Back} are the total counts from the object and background ROIs respectively and P_{Obj} and P_{Back} are the number of pixels in the object and background ROIs.

This was repeated for the anterior and posterior image and an average of the **Equation 4-6** results taken using **Equation 4-7**.

$$\overline{CR} = \frac{CR_{ant} + CR_{post}}{2}$$

Equation 4-7

where $\overline{CR}$ is the average count rate and CR_{ant} and CR_{post} are the anterior and posterior background corrected rates, respectively.

Using this method and the 6 planar images of the bottle phantom, a calibration curve was created. The true activity contained in the bottle at the time of each scan versus the $\overline{CR}$ in **Figure 4-26** depicts the calibration curve with predication bands.

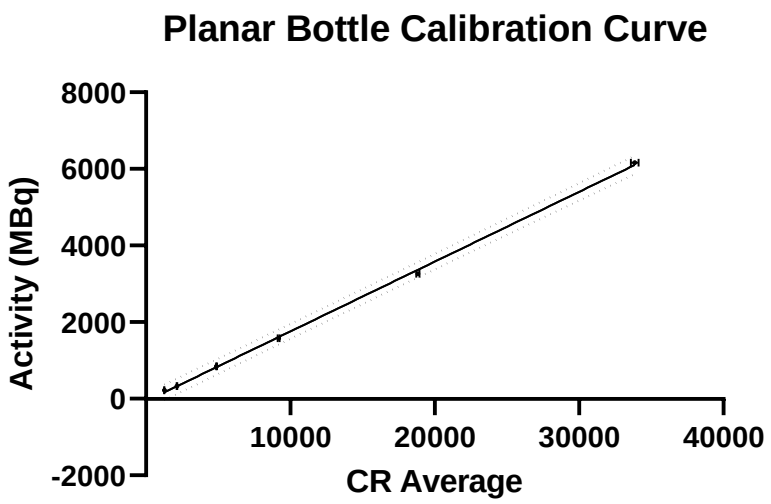

Figure 4-26 *Planar bottle calibration curve. The bottle phantom, initially containing 6000 MBq, was imaged once a week for 6 weeks, relying solely on decay to vary the activity. Each acquisition Count Rate (CR) for anterior and posterior view was background subtracted then averaged. This was plotted with the true activity to create the calibration curve to convert average count rate to activity.*

Table 4-15 *Line of best fit with goodness of fit information for data in Figure 4-1.*

Equation	Activity = 0.1822*$\overline{CR}$ - 64.71
r-Squared	0.9994
Sy.x	64.84

While the resulting fit in **Table 4-15** indicates a good fit, the application yielded highly inaccurate results.

The NEMA phantom planar results were only examined for total activity, not that of individual spheres. Clinically at SCGH, planar acquisitions are only examined for an estimate of whole-body retention. Drawing a reliable ROI that contains only information pertinent to one sphere is not possible due to spill over from surrounding spheres, as seen in **Figure 4-4**.

The NEMA phantom planar results were collected with the same method as previously discussed and converted to count rate using **Equation 4-6** and **Equation 4-7** and then converted to activity using the equation in **Table 4-15**.

Results were graphed with the true activity of the phantom and fitted with a linear regression, **Figure 4-27** and **Table 4-16**.

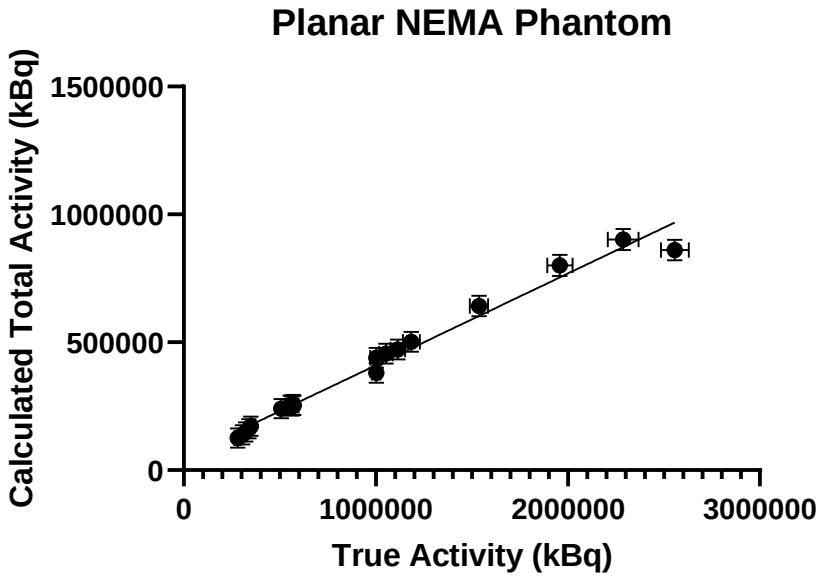

Figure 4-27 *The Planar Bottle Calibration Curve was used to convert the CR results of the planar NEMA phantom images to activity. Only whole-body, rather than individual spheres, was quantified. The results are plotted here with the true activity and fitted with a linear regression. The closer the linear regression to y = x, the better the accuracy. The accuracy of the planar results is poor due to lack of corrections for factors such as scatter and attenuation.*

Table 4-16 *Linear equation and goodness of fit information for data in Figure 4-27.*

Equation	Y = 0.3588*X + 51316
r-Squared	0.9808
Sy.x	35730

The closer the results to y = x, the better the accuracy of the results. As seen in **Table 4-16**, they are far from this and so highly inaccurate. None of the results reached even 50% of the desired true activity, shown in a plot of the **Equation 4-8** in **Figure 4-28**.

$$\%\ true\ activity = \frac{Calculated\ Total\ Activity\ (kBq)}{True\ Activity\ (kBq)} \times 100$$

Equation 4-8

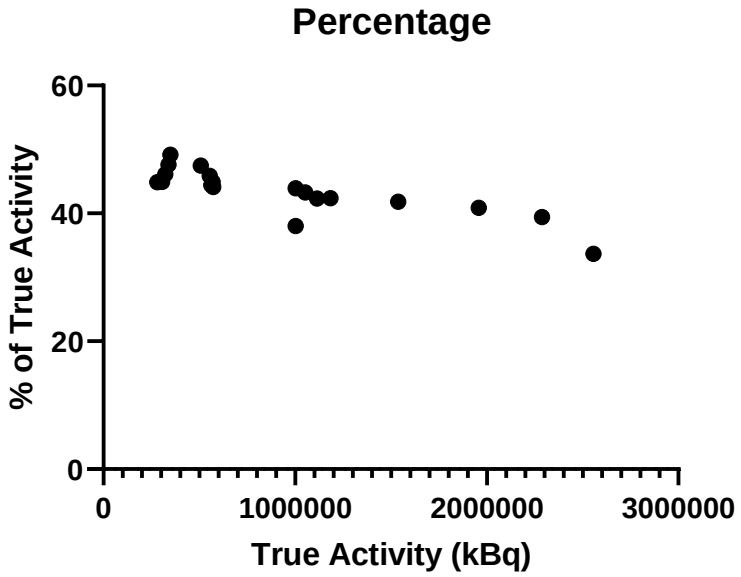

Figure 4-28 *Plot of the percentage of the true activity for the planar NEMA phantom results. The calculated activity is always less than 60% of that of the true activity. If it were accurate the data would be in a horizontal line at 100%.*

The poor results are due to the lack of corrections the SPECT has applied to it such as attenuation and scatter correction. While it is possible to apply scatter correction to a planar image using methods such as an attenuation map from the acquired CT, this is beyond the scope of this study (Bailey et al. 2015b; Beauregard et al. 2011; King & Farncombe 2003). This could be considered for future work to increase accuracy and further compare with SPECT/CT results.

Similarly, while MIM (Medical Image Merge) software has the ability to perform dosimetry using one SPECT and multiple planar, this is also beyond the scope of this study as quantitation of a single image is the focus, rather than multiple timepoint dosimetry (Nelson, A, Mirando, D, Nilman, R 2020).

In addition to the SPECT/CT data, planar acquisition was used to scan the NEMA phantom. The results were analysed to calculate the total activity in the phantom, rather than individual spheres. Similar to the 3D Flash data, results required conversion from counts to count rate and then to activity. A technique similar to that used for clinical wholebody retention calculations was used. The count rate for the anterior and posterior image were background subtracted and averaged. To convert the results to activity, the same bottle phantom for 3D Flash was imaged using planar acquisition and the results were used to create a calibration curve to convert from count rate to activity. The results had poor accuracy due to the lack of corrections for confounding factors such as scatter and attenuation.

4.3.6 Uncertainties

The only uncertainty that impacted decision in this study are those discussed in section 4.3.1.3.2. All other uncertainty calculations and results are further discussed in Appendix J.

5 Conclusion

5.1 Implications for Clinical Practice

SCGH commenced Lu-177 therapy for metastatic prostate cancer (using Lu 177 PSMA) and neuroendocrine tumours (using Lu-177-octreotate) in 2018. Dosimetry for these patients requires post therapy imaging with a Siemens Symbia Intevo SPECT/CT which is equipped with XSPECT quant (automated quantification) for Lu-177.

The aim of this study was to determine if automated (XSPECT reconstruction) is more accurate than manual (3D Flash reconstruction) quantification when considering Lu-177 in a clinical context as well as the optimal measurement conditions in a clinical context. The designed NEMA phantom study covered a wide range of clinically applicable patient uptakes. SCGH typically only scans Lu-177 patients from 24 hours post therapy, so quantities were based on a literature review of blood concentration and tumour/OAR uptake from 24 hours post infusion of PSMA or octreotate. Blood concentration was represented by phantom background activity concentration and tumour/organs by fillable spheres.

Prior to the phantom study, the accuracy of the dose calibrator and deadtime effects were addressed. The dose calibrator plays a key role in both quantification methods and so its accuracy and optimal measuring conditions for Lu-177 were determined. Vial and syringe geometry are clinically relevant and each was applied to this study, so both were investigated. Measurements for both geometries at various heights from the base of the well were compared to that of the manufacturers' results. The manufacturers' calibrated activity was chosen for comparison because their equipment is more regularly officially calibrated. No correction factor was necessary to measure Lu-177 and a distance of approximately 10 cm from the base of the well was the optimal position for both vial and syringe measurements.

Deadtime effects are isotope-, collimator- and camera-specific and can have an impact on quantification results. Traditional methods utilising a large Lu-177 activity and relying on decay were unsuitable for this study taking place on a high-demand camera, due to the relatively long half-life of Lu-177. To measure deadtime, a new intrinsic method was developed using nine sealed 10 MBq sources of Lu 77 to allow collection of a larger volume of data in a much shorter period of time. Sources were placed in a 3D printed holder attached to an inbuilt probe that extended to approximately the middle of the FOV. In a single day nine measurements were taken by first measuring a single source to give the minimum activity then sequentially adding another and measuring until all nine sources were included in the holder to measure the maximum activity. Count rate deadtime thresholds of 25 and 20 kcps were determined for camera heads 1 and 2, respectively. Since all the measurements taken in the phantom study were below these thresholds, it was determined that no deadtime correction was necessary.

Phantom images were acquired once per day over 20 consecutive working days, with the phantom background concentration manually altered to create a range of background to sphere ratios. MELP collimators, 208 keV photopeak and Triple Energy Window scatter correction with dual reconstruction (XSPECT and 3D Flash for automated and manual quantification respectively) were applied. The RECIST contouring tool in Syngo.Via was used to collect automated and manual quantification results. Data were collected using RECIST 10, 20, 30 and 40% thresholds of the maximum counts, with and without recovery coefficients for partial volume correction.

The study's findings provided some implementable changes to clinical practices. First, the well counter measurements using vials should be measured with the dipper 10 cm above the base of the well for optimal results. Second, deadtime need not be corrected for if considering patient imaging from 24 hours post infusion. And third, most importantly, automated (XSPECT) is a significant improvement on manual quantification (3D Flash). Optimal measurement conditions included a 30% RECIST threshold which should be applied when considering quantification, instead of the currently standard 40% threshold, where Lu 177 is concerned. If CT derived volumes (rather than RECIST) are applied, then partial volume correction is essential.

5.2 Further Work

Should the routine clinical practice be modified to include scanning patients immediately post infusion, a count rate would need to be determined for a patient dose before any opportunity for excretion or radionuclide decay. This increases the scanned activity to 8 GBq (possibly more), which is the maximum dose currently administered for NET and mCRPC patients. If this is determined to be above the deadtime threshold, a correction should be formed and implemented.

If planar images are desired for quantification use, for either wholebody retention or discrete objects, attenuation and scatter correction are necessary. It is possible to apply such corrections to a planar image using an attenuation map from an acquired CT. While this was beyond the scope of this study, the planar phantom images were acquired with a birds-eye-view of all the spheres so they would appear discretely. This allows the data to be useful for future work that wishes to address individual sphere quantification, and not simply wholebody retention.

When considering the use of CT derived volumes in quantification, further work would be required to allow such a correction to handle the more complex shapes that occur clinically. A PVC with factors such as surface area and compactness of shape are possible. This would be achievable through a phantom study with more complex shapes. Objects with inhomogeneous uptake should also be considered.

PVC using RECIST derived volumes, rather than CT derived volumes, could also be considered. For this to be successful the RECIST volumes would need to closely resemble the actual volumes. The accuracy of the RECIST volume depends on the threshold, size of the object and the activity concentration. A RECIST based PVC would require inclusion of these correlated factors.

Any incorporation of the background effects into a correction would need to consider the object size. This study confirmed that the smaller the sphere was, the more acute the PVE was. The background to sphere concentration ratio would also require consideration. The larger the ratio, the larger the effect of the background on the results. Both of these effects would need further examination for quantification and formation of a correction.

Appendix A. Deadtime Results for Camera Head 2

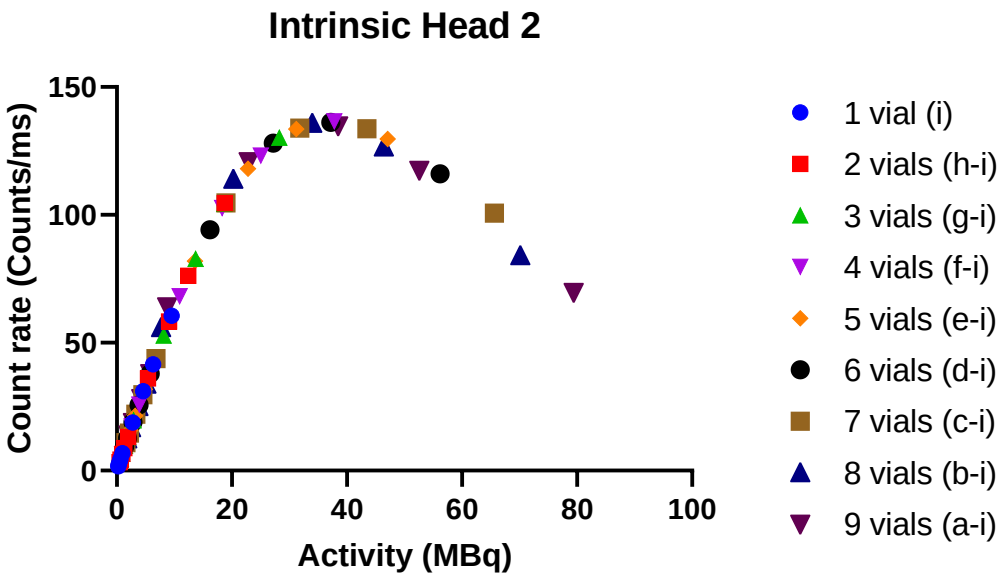

Figure A - 1 *Intrinsic measurements for camera head 2, using measurements of multiple vials on the same day.*

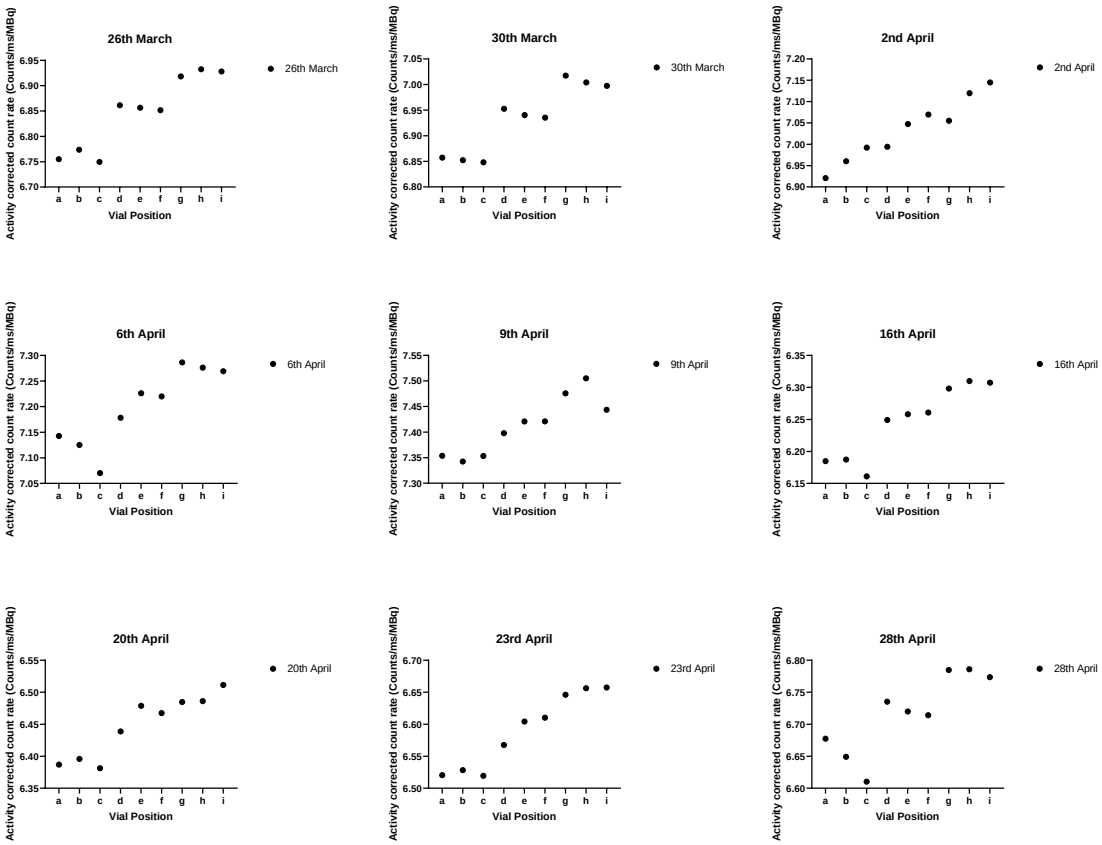

Figure A - 2 *Results for camera head 2, V-Vial-a imaged in every position, 'a' through 'i', in the holder on each day of imaging. The results are decay corrected.*

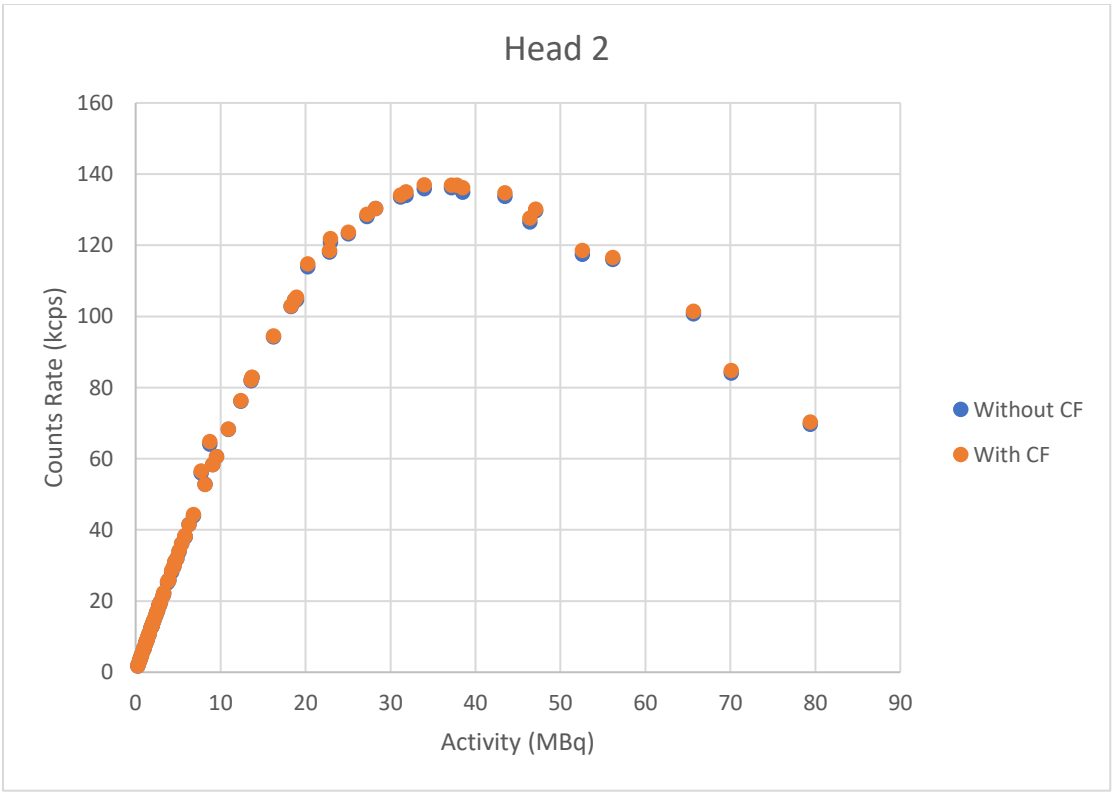

Figure A - 3 *The intrinsic deadtime results with and without the CF for camera head 2.*

Appendix B. Deadtime CF Statistical Analysis

Firstly, the **D'Agostino-Pearson** normality test was applied in *PRISM* to test if the data were normally distributed. Prism first computes the skewness and kurtosis to quantify how far the distribution is from Gaussian in terms of asymmetry and shape. It then calculates how far each of these values differs from the value expected with a Gaussian distribution, and computes a single P value from the sum of these discrepancies. D'Agostino developed several normality tests, of which Prism uses the "omnibus K2" test (Prism 1986). **D'Agostino-Pearson** was also applied to test for lognormality. The results are for each camera head are listed in **Table B - 1** and **Table B - 2**.

Table B - 1 *Summary of normality test results applied to intrinsic deadtime data with and without a CF for camera head 1.*

	Camera Head 1	
Compare normal and lognormal	**Count Rate Without CF**	**Count Rate With CF**
Probability normal (Gaussian)	8.234e-008%	7.823e-008%
Probability lognormal	100%	100%
Likelihood ratio (LR)	8.234e-010	7.823e-010
1/LR	1214523293	1278348067
Which distribution is more likely?	Lognormal	Lognormal
Test for lognormal distribution		
D'Agostino & Pearson test		
K2	8.624	8.594
P value	0.0134	0.0136
Passed lognormality test (alpha=0.05)?	No	No
P value summary	*	*
Number of values	81	81
Impossible values in lognormal distributions		
Number of zeroes	0	0
Number of negative values	0	0

Table B - 2 *Summary of normality test results applied to intrinsic deadtime data with and without a CF for camera head 2.*

	Camera Head 1	
Compare normal and lognormal	**Count Rate Without CF**	**Count Rate With CF**
Probability normal (Gaussian)	8.736e-008%	8.681e-008%
Probability lognormal	100%	100%
Likelihood ratio (LR)	8.736e-010	8.681e-010
1/LR	1144662992	1151995140
Which distribution is more likely?	Lognormal	Lognormal
Test for lognormal distribution		
D'Agostino & Pearson test		
K2	9.059	9.008
P value	0.0108	0.0111
Passed lognormality test (alpha=0.05)?	No	No
P value summary	*	*
Number of values	81	81
Impossible values in lognormal distributions		
Number of zeroes	0	0
Number of negative values	0	0

In **Table B - 1** and **Table B - 2**, the “compare normal and lognormal” indicates which out of normal and lognormal is more likely. Lognormal was definitely the more likely. This, however, is not to be interpreted as the distribution being accepted as lognormal, it is just more likely compared to a normal distribution. Lognormal being the more likely of the two is expected since the shift between the data with and without the CF is one way, the data with the CF is shifted higher in **Figure 3-14**.

The data was then tested for lognormality likelihood. With a P-value <0.05, shown in **Table B - 1** and **Table B - 2**, the null hypothesis that the data is sampled from a normal distribution is rejected.

With the lack of normality confirmed, next the **Wilcox matched pairs test** was employed to see if the data had a statistically significant shift after the CF was applied. The Wilcoxon signed-rank test is a non-parametric statistical hypothesis test used to compare two related samples to assess whether their population mean ranks differ (i.e. it is a paired difference test) (Prism 2022).

Table B - 3 *Wilcox matched pairs test results for intrinsic deadtime data with and without a CF for camera head 1.*

Column B	Position corrected count rate (kcps)
vs.	vs.
Column A	Count rate (kcps)
Wilcoxon matched-pairs signed rank test	
P value	<0.0001
Exact or approximate P value?	Exact
P value summary	****
Significantly different (P < 0.05)?	Yes
One- or two-tailed P value?	Two-tailed
Sum of positive, negative ranks	2544 , -84.00
Sum of signed ranks (W)	2460
Number of pairs	81
Number of ties (ignored)	9
Median of differences	
Median	0.09747
How effective was the pairing?	
rs (Spearman)	0.9999
P value (one tailed)	<0.0001
P value summary	****
Was the pairing significantly effective?	Yes

Table B - 4 *Wilcox matched pairs test results for intrinsic deadtime data with and without a CF for camera head 2.*

Column B	Position corrected count rate (kcps)
vs.	vs.
Column A	Count rate (kcps)
Wilcoxon matched-pairs signed rank test	
P value	<0.0001
Exact or approximate P value?	Exact
P value summary	****
Significantly different (P < 0.05)?	Yes
One- or two-tailed P value?	Two-tailed
Sum of positive, negative ranks	2486 , -142.0
Sum of signed ranks (W)	2344
Number of pairs	81
Number of ties (ignored)	9
Median of differences	
Median	0.1053
How effective was the pairing?	
rs (Spearman)	0.9999
P value (one tailed)	<0.0001
P value summary	****
Was the pairing significantly effective?	Yes

The P values in **Table B - 3** and **Table B - 4** determines if the median difference between the data sets is zero, what is the chance that random sampling would result in a median change as far from zero as observed in the data? If the p value is small, the observed difference is not due to chance. The small P value in **Table B - 3** and **Table B - 4** support that the position correction makes a statistically significant difference for both camera heads (Prism 2022).

Appendix C. Deadtime Full Results

Table C - 1 *Camera head 1 and 2 results for line of no losses with the cut off points surrounded in red.*

Camera Head 1					Camera Head 2				
Count Rate (kcps)	**R^2**	**Sy.x**	**P value (runs test)**	**Deviation from linearity**	**Count Rate (kcps)**	**R^2**	**Sy.x**	**P value (runs test)**	**Deviation from linearity**
101.9	0.9946	1.96	<0.0001	Significant	102.7	0.9912	2.386	<0.0001	Significant
93.8	0.9952	1.731	<0.0001	Significant	94.2	0.9927	2.013	<0.0001	Significant
82.1	0.9971	1.252	<0.0001	Significant	82.8	0.9935	1.753	<0.0001	Significant
82	0.9981	0.9268	<0.0001	Significant	81.9	0.9934	1.664	<0.0001	Significant
76.2	0.9984	0.8	<0.0001	Significant	76.1	0.994	1.48	0.0249	Significant
68.2	0.9989	0.6034	<0.0001	Significant	68.2	0.9944	1.328	0.1577	Not Significant
60.8	0.9992	0.4702	<0.0001	Significant	64	0.9938	1.312	0.062	Not Significant
57.9	0.9994	0.4001	<0.0001	Significant	60.6	0.9939	1.237	<0.0001	Significant
55.3	0.9994	0.385	<0.0001	Significant	58.3	0.994	1.165	<0.0001	Significant
52.8	0.9994	0.3503	0.0001	Significant	55.9	0.9965	0.8133	0.041	Significant
49.5	0.9995	0.2944	0.0114	Not Significant	52.8	0.9964	0.7688	0.002	Significant
43.8	0.9995	0.2918	0.0733	Significant	43.9	0.9997	0.2146	0.0005	Significant
41.7	0.9995	0.2612	0.0249	Significant	41.5	0.9997	0.1849	0.0057	Significant
37.9	0.9996	0.2263	0.0079	Significant	38	0.9997	0.1805	0.0087	Significant
37.8	0.9995	0.2289	0.0102	Not Significant	37.9	0.9997	0.1609	0.0021	Significant
36.1	0.9996	0.2103	0.0502	Significant	36.1	0.9998	0.1491	0.0155	Significant
33.6	0.9996	0.1964	0.0334	Significant	33.8	0.9997	0.1506	0.0226	Significant
31.9	0.9995	0.1968	0.0226	Not Significant	31.8	0.9997	0.1484	0.0296	Significant
30.8	0.9995	0.1915	0.1025	Significant	31	0.9998	0.1304	0.0187	Significant
29.6	0.9995	0.1781	0.038	Not Significant	29.7	0.9997	0.1309	0.0116	Significant
28.3	0.9995	0.1804	0.0516	Not Significant	28.2	0.9998	0.1139	0.0349	Significant
25.7	0.9995	0.1649	0.1376	Significant	25.8	0.9997	0.1148	0.0219	Significant
25.6	0.9994	0.1652	0.0219	Not Significant	25.7	0.9998	0.1028	0.0345	Significant
25.2	0.9995	0.1471	0.363	Not Significant	25.1	0.9998	0.08792	0.045	Significant
22.1	0.9996	0.127	0.1908	Not Significant	22	0.9998	0.08726	0.0109	Significant
21.4	0.9996	0.1247	0.4148	Not Significant	21.5	0.9998	0.08864	0.016	Significant
19.6	0.9995	0.1259	0.32	Not Significant	19.7	0.9998	0.07972	0.7147	Not Significant
19.1	0.9996	0.1136	0.4231	Not Significant	18.9	0.9998	0.07567	0.6153	Not Significant
18.9	0.9996	0.1013	0.9631	Not Significant	18.9	0.9998	0.07621	0.5137	Not Significant
18.8	0.9996	0.1016	0.8847	Not Significant	18.8	0.9998	0.07745	0.6317	Not Significant

17.3	0.9996	0.1033	0.9296	Not Significant	17.3	0.9998	0.06907	0.2265	Not Significant
16.8	0.9996	0.09741	0.1621	Not Significant	16.8	0.9998	0.05511	0.4116	Not Significant
16	0.9997	0.08295	0.8724	Not Significant	15.9	0.9998	0.05296	0.7692	Not Significant
14.8	0.9996	0.0831	0.8243	Not Significant	14.7	0.9998	0.05405	0.6883	Not Significant
13.9	0.9996	0.07888	0.1842	Not Significant	14	0.9998	0.05524	0.6369	Not Significant
13.1	0.9996	0.08064	0.2174	Not Significant	13.2	0.9998	0.05364	0.2189	Not Significant

Appendix D. Pig Data

Table D - 1 Beykan et al. (2016) table of blood samples taken from pigs, weighing 25-32 kg, who were administered 105 MBq of Lu-177. A human dose of 8500 MBq and weight of 70 kg was assumed for scaling factors in **Equation 4-1**.

* Decay-corrected to the time of sampling

** %IA/ml denotes percentage injected activity per volume of blood

	Time post dosing	Time post dosing	Whole blood				Plasma	
	Minutes	hours	Bq/ml*	kBq/ml*	kBq/mL Scaled	%IA/ml**	Bq/ml*	%IA/ml**
Pig 1	1.18	0.020	24986	24.986	924.7	0.02443	39017	0.03815
	1.22	0.020	20887	20.887	773.0	0.02078	32837	0.03266
	3.2	0.053	12499	12.499	462.5	0.01243	18324	0.01823
	5.05	0.084	9373	9.373	346.9	0.00933	13686	0.01362
	10.05	0.168	5494	5.494	203.3	0.00547	8304	0.00827
	20	0.333	3153	3.153	116.7	0.00314	4860	0.00484
	30.1	0.502	2278	2.278	84.30	0.00227	3484	0.00347
	50	0.833	1686	1.686	62.39	0.00168	2340	0.00234
	75.02	1.250	1193	1.193	44.15	0.00119	1834	0.00183
	100.05	1.668	939	0.939	34.75	0.00094	1426	0.00143
	200.05	3.334	659	0.659	24.39	0.00067	1027	0.00104
	300	5.000	498	0.498	18.43	0.00051	672	0.00068
	3030	50.50	101	0.101	3.738	0.00012	162	0.0002
	5910	98.50	64	0.064	2.368	0.0001	99	0.00015
	8730	145.5	37	0.037	1.369	0.00007	62	0.00012
	17400	290.0	6	0.006	0.222	0.00002	13	0.00005
Pig 2	1.4	0.023	16156	16.156	597.9	0.01517	22058	0.02072
	2.15	0.036	13592	13.592	503.0	0.01277	17445	0.01638
	3	0.050	10943	10.943	405.0	0.01028	14867	0.01396
	5	0.083	7720	7.72	285.7	0.00725	10170	0.00955
	10.02	0.167	4628	4.628	171.3	0.00435	6110	0.00574
	20.03	0.334	2684	2.684	99.33	0.00252	3712	0.00349
	30.17	0.503	1950	1.95	72.16	0.00184	2787	0.00262
	50.03	0.834	1400	1.4	51.81	0.00132	1937	0.00183
	75.16	1.253	1054	1.054	39.01	0.001	1389	0.00131
	99.5	1.658	884	0.884	32.71	0.00084	1173	0.00111
	200.1	3.335					744	0.00071
	300	5.000	396	0.396	14.65	0.00038	528	0.00051
	3180	53.00	84	0.084	3.109	0.0001	134	0.00016
	6060	101.0	58	0.058	2.146	0.00009	94	0.00014
	8892	148.2	29	0.029	1.073	0.00005	54	0.0001
	17610	293.5	4	0.004	0.148	0.00001	9	0.00003
Pig 3	0.35	0.006	42509	42.509	1573.1	0.0403	55934	0.05302
	1.22	0.020	35041	35.041	1296.8	0.03322	48037	0.04554
	2.13	0.036	26473	26.473	979.68	0.0251	36024	0.03415
	5	0.083	16265	16.265	601.92	0.01542	21724	0.0206

	10.34	0.172	10020	10.02	370.81	0.00951	13555	0.01286
	19.56	0.326	6587	6.587	243.76	0.00625	9026	0.00857
	29.44	0.491	4965	4.965	183.74	0.00472	6775	0.00644
	49	0.817	3310	3.31	122.49	0.00315	4687	0.00446
	82.2	1.370	2087	2.087	77.233	0.00199	3379	0.00322
	100.14	1.669	1838	1.838	68.019	0.00176	3643	0.00348
	199.18	3.320	1452	1.452	53.734	0.0014	2013	0.00194
	300	5.000	1071	1.071	39.634	0.00104	1777	0.00172
	3360	56.00	138	0.138	5.1069	0.00017	159	0.00019
	6180	103.0	43	0.043	1.5913	0.00006	69	0.0001
	14880	248.0	10	0.01	0.3701	0.00003	12	0.00003
Pig 4	1	0.017	29160	29.16	1079.1	0.02581	38536	0.0341
	1.15	0.019	27344	27.344	1011.9	0.0242	34930	0.03092
	2.05	0.034	21540	21.54	797.1	0.01907	28053	0.02483
	5.05	0.084	13905	13.905	514.6	0.01231	18353	0.01625
	10.02	0.167	8458	8.458	313.0	0.00749	11094	0.00983
	19.58	0.326	5007	5.007	185.3	0.00444	6540	0.0058
	29.48	0.491	3651	3.651	135.1	0.00324	4878	0.00433
	49.55	0.826	2713	2.713	100.4	0.00241	3450	0.00306
	74.56	1.243	2058	2.058	76.2	0.00183	2641	0.00235
	99.45	1.658	1673	1.673	61.9	0.00149	2136	0.0019
	225	3.750	1085	1.085	40.2	0.00098	1447	0.0013
	300	5.000	829	0.829	30.7	0.00075	1102	0.001
	3360	56.00	168	0.168	6.2	0.00019	202	0.00023
	6180	103.0	93	0.093	3.4	0.00013	122	0.00017
	14880	248.0	11	0.011	0.4	0.00003	12	0.00003
Pig 5	0.4	0.007	43410	43.41	1606.5	0.04476	68287	0.0704
	0.57	0.010	31774	31.774	1175.9	0.03276	48412	0.04991
	1.56	0.026	14945	14.945	553.1	0.01541	29290	0.0302
	4.58	0.076	8304	8.304	307.3	0.00856	13910	0.01435
	10.49	0.175	6029	6.029	223.1	0.00622	8459	0.00873
	20.06	0.334	3825	3.825	141.6	0.00395	5395	0.00557
	29.22	0.487	2821	2.821	104.4	0.00291	4134	0.00427
	49.44	0.824	1827	1.827	67.6	0.00189	2756	0.00285
	76	1.267	1499	1.499	55.5	0.00155	2036	0.00211
	100	1.667	1138	1.138	42.1	0.00118	1726	0.00179
	206.1	3.435	758	0.758	28.1	0.00079	1161	0.00121
	293	4.883	574	0.574	21.2	0.0006	835	0.00088
	3360	56.00	127	0.127	4.7	0.00016	171	0.00022
	6000	100.0	72	0.072	2.7	0.00012	105	0.00017
	14700	245.0	12	0.012	0.4	0.00004	14	0.00004

Appendix E. Sir Charles Gairdner and Fiona Stanley Hospital Lutetium^{177} Agreement

As part of my professional development while under the employ of SCGH as a Medical Physicist, I have commenced a Masters of Medical Physics undertaken with the University of Adelaide, part of which is a research project concerning the quantification of Lu^{177}. The study's central focus is to ascertain the scope and capability of a Siemens Symbia T16 SPECT/CT to quantify Lu^{177}. This is to be facilitated through a series of phantom studies with clinically relevant quantities of Lu^{177}. The quantities of Lu^{177} for this study cannot be satisfied through the one-off purchase of 5GBq already made and so a "top up dose" once a week is required. Without reliable weekly Lu^{177} therapies, this top up dose in unable to be sourced from within SCGH.

This document includes the details of agreement between SCGH and FSH pertaining to the collection, transport and use of residual Lu^{177} post therapy for use as a top up dose.

1) Specification of use:

The purpose of the Lutetium received from FSH is strictly for phantom studies and not clinical patient use.

2) Transport:

a) General Training

In accordance with RSP-C-2-2019 (ARPANSA 2019), I have received the necessary training to handle and transport unsealed radioactive material. This includes:

(i) The unsealed handling course supplied by the University of Western Australia;

(ii) General awareness/familiarization training including description of the categories of radioactive material; labelling, marking, placarding and packaging and segregation requirements; the purpose and content of the radioactive material transport document; and the available emergency response documents;

b) Safety training

(i) Methods and procedures for avoidance of accident conditions during transport, such as proper use of package handling equipment and appropriate methods of stowage of radioactive material.

(ii) Available emergency response information and how to use it.

(iii) General hazards presented by the various categories of radioactive material and how to prevent exposure to those hazards, including, if appropriate, the use of personal protective clothing and equipment.

(iv) Procedures to be immediately followed in the event of an unintentional release of radioactive material, including any emergency response procedures for which the person is responsible and personal protection procedures to be followed.

I will be transporting the radioactive material under the general supervision of a Radiation Safety Act licensee, Chief Radiochemist Chris Jones. The packages will be carried securely: in the boot of a car; or away from driver in vans and station wagons, in a shielded container and Type-A packaging which I will provide. The package will not be left unattended at any time. I will also provide the consignment form which I will attached to each package and ensure that it has been completed with details of the radionuclide being delivered and its destination, including the measurement and calculation of the packages transport index.

3) Supply

After consultation with FSH RSO John Burrage and radiochemist Divesh, Lu^{177} therapies are administered on Tuesdays and Wednesdays, usually with a minimum residual of 1GBq. The collection of unused Lu^{177} would be once per week on the Tuesday of any unutilised activity for the month of February and March 2021.

Appendix F. Tc-99m Methodology

Since Lu-177 was not readily available, a trial was run prior to use of Lu-177. The aim was to become familiarised with the use of the phantom, camera and scan protocol. Tc-99m was chosen due to its availability and being an included isotope for the XSPECT feature. Due to the difference in half-life, the phantom methodology differed.

The camera was accessed once per day, and with a half-life of 6 hours, both sphere and background activity were altered manually for each scan. The spheres were drained each day with a spinal needle and syringe, and the syringe activity measured. Residual in the spheres was calculated using this measurement. The spheres were refilled using the same method as described in section 4.2.1.1. The background was not drained and only required removal of a small volume so addition of activity could take place.

The desired quantities were derived from the Lu-177 plan in section 4.2.1. The difference in image quality owing to the difference in gamma energies, relative fluence and collimators meant direct comparison with Lu-177 was not possible. Instead, an estimate of similar background to sphere ratios was used.

The highest total activity contained in the spheres chosen was 1000 MBq to ensure the lowest activity scans were not extremely small quantities. Each Tc-99m scan correlated to a Lu-177 scan by using the same background to sphere ratio and approximately the same percentage of the initial scans sphere activity. This plan is displayed in **Figure F - 1**.

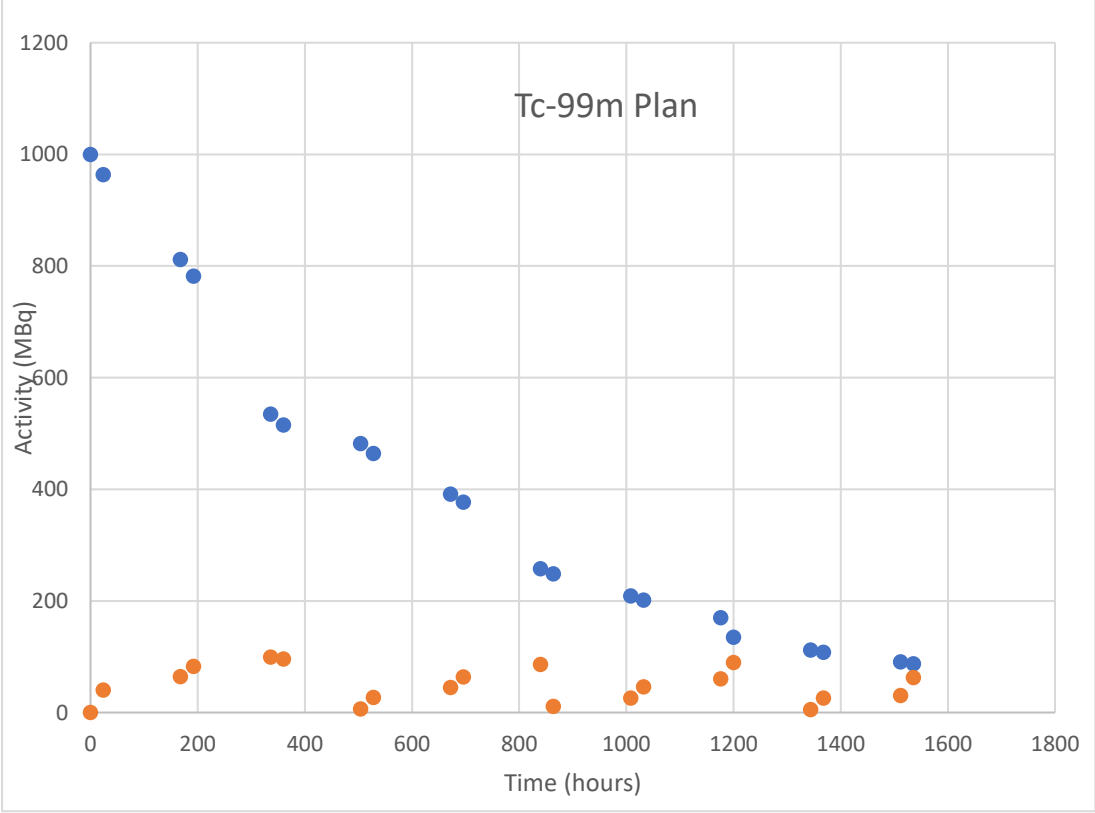

Figure F - 1 *Initial draft of Tc 99m activity in spheres and background of the NEMA phantom for the duration of the study. Sphere activity is the total activity contained across all spheres. The time in hours does not reflect actual scan times, it represents a rough, overall timeline of 10 weeks (1600 hours) where scanning occurs approximately twice in 8 days.*

The scan protocol was identical to that for Lu-177, except for the stop conditions and the use of 3D Flash reconstruction. Rather than 40 kCts, stop conditions were set to 200 kCts. As these scans were prior to the Lu-177, the threshold to achieve the minimum required total counts for XSPECT had not been determined. Due to time constraints, total counts were reduced close to the minimum when scanning Lu-177.

Appendix G. Tc-99m Results

With its long-standing use as a diagnostic isotope, Tc-99m absolute quantitation has been available for longer than Lu-177. There have been studies about the quantitative capabilities of these reconstructions for Tc-99m (Bailey & Willowson 2013; Willowson et al. 2010; Willowson, Bailey & Baldock 2008). The purpose of a Tc-99m study was to familiarise with the XSPECT protocol and reconstruction, rather than a full assessment of its capabilities and direct comparison to Lu-177. A direct comparison would not be valid since the activities used were not directly comparative, and the protocols were not identical, as discussed in Appendix F. Nonetheless, the accuracy of the results was investigated.

Peak remained the chosen Syngo.Via statistic. The PVC follows the method discussed in section 4.3.1.3.1. **Figure G - 1** displays the raw data before any corrections.

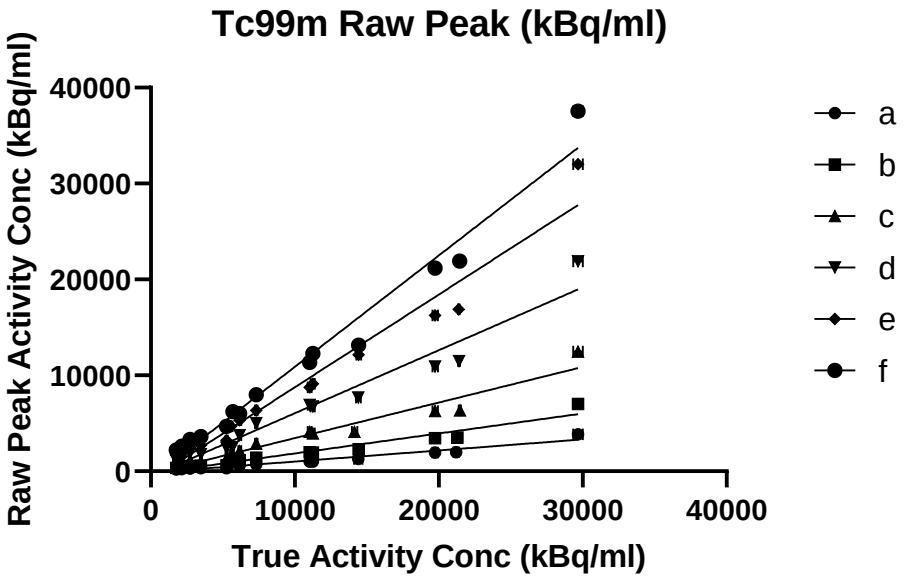

Figure G - 1 *Plot of raw Peak activity concentration (kBq/ml) results for Tc-99m NEMA phantom results using the XSPECT reconstruction. Each sphere is assigned its own linear regression due to the expected PVE. The closer the regression to y = x, the better the accuracy.*

Table G - 1 *The linear regressions per sphere of the raw peak data once again show the need for PVC.*

Sphere	a	b	c	d	e	f
Equation	Y = 0.1156*X - 143.1	Y = 0.2085*X - 229.7	Y = 0.3711*X - 256.7	Y = 0.6566*X - 518.2	Y = 0.9661*X - 906.1	Y = 1.161*X - 728.3
r-Squared	0.9535	0.9467	0.9513	0.9571	0.9615	0.9752
Sy.x	228.5	429.6	729.3	1208	1680	1609

As described in section 4.3.1.3.1, the gradients were again used to create a RC gradient through fit with **Equation 4-3**, the results are displayed in **Figure G - 2** and **Table G - 2**.

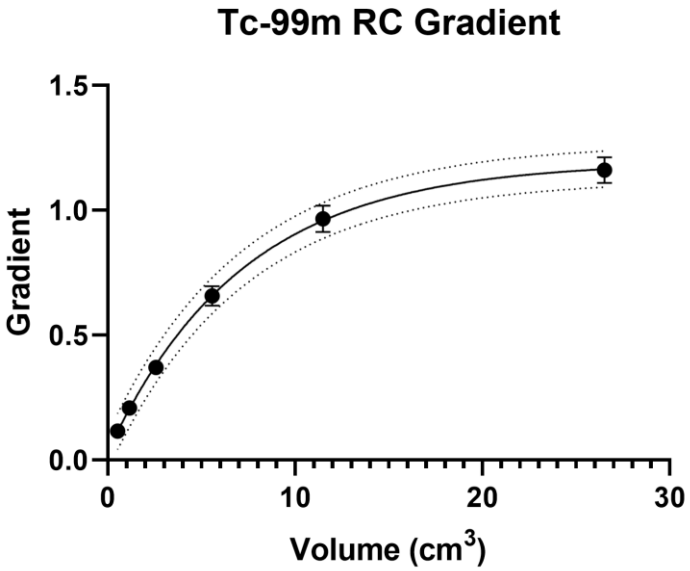

Figure G - 2 *Gradients from linear fits in* ***Figure G - 1*** *plotted against the corresponding sphere volumes. Fitted with RC* ***Equation 4-3****. The 95% Confidence band is too close to the exponential fit to visualise but the 95% prediction band is visible and further indicates a good fit.*

Table G - 2 *Line of best fit data for Gradient RC in Figure G - 2. Gradients from linear fits in Figure G - 1 Peak plotted against the corresponding sphere volumes. Fitted with RC Equation 4.3. The 95% Confidence band is too close to the exponential fit to visualise but the 95% prediction band is visible and further indicates a good fit.*

y=c-a*exp(-b*x)	
Best-fit values	
c	1.194
a	1.162
b	0.1389
95% CI (profile likelihood)	
c	1.179 to 1.209
a	1.146 to 1.177
b	0.1335 to 0.1445
Goodness of Fit	
r-Squared	201
Sum of Squares	0.9914
Sy.x	0.2635

With **Figure G - 2** prediction bands and a high r-squared value in **Table G - 2**, the fit was deemed acceptable. The **Table G - 2** determined equation for $RC_{gradient}$ for Tc-99m was applied to the raw data resulting in **Figure G - 3**.

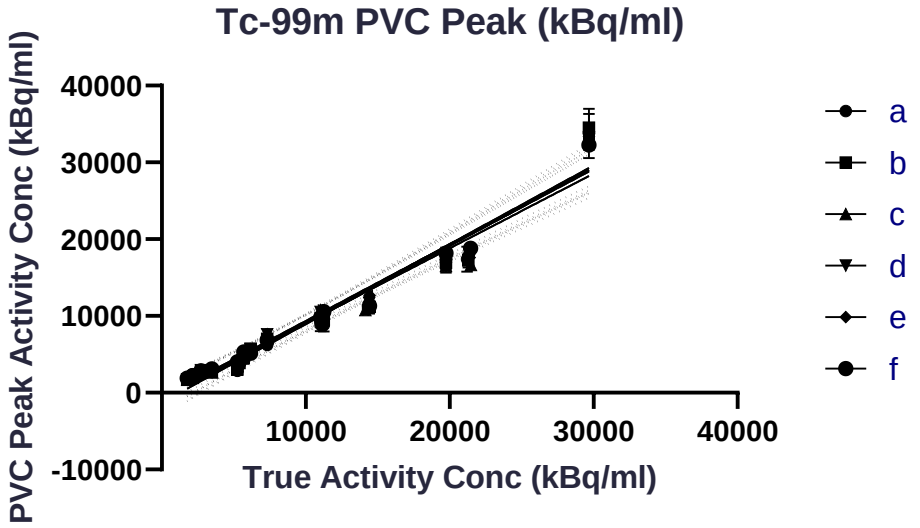

Figure G - 3 Tc-99m Peak Partial Volume Corrected activity concentration results versus the True activity concentration. Results were corrected using $RC_{gradient}$ with results from **Table G - 2** in **Equation 4-4**. Each sphere is fitted with a linear regression to assess its accuracy.

Table G - 3 *Linear equations with goodness of fit information for data in* **Figure G - 3**.

Sphere	a	b	c	d	e	f
Equation	Y = 1.019*X - 1260	Y = 1.024*X - 1128	Y = 0.9739*X - 673.7	Y = 0.9976*X - 787.2	Y = 1.008*X - 945.7	Y = 0.9972*X - 625.5
r-Squared	0.9535	0.9466	0.9513	0.9571	0.9615	0.9752
Sy.x	2013	2110	1914	1836	1753	1382

The same desirable as criteria discussed in section 4.3.1.3.4 applies; a linear fit closer to $y = x$, high R squared and low Sy.x values. These criteria were met by the PVC data in **Table G - 3** and **Figure G - 3** visualises the improved accuracy and precision.

These results, as discussed in section 4.3.3, were combined with various available volumes to calculate the activity in each sphere. Only the actual volume and the 30 and 40% RECIST volumes were considered since they were established the most successful in section 4.3.3. Select combinations were applied. The PVC data was combined with the actual volumes, since the correction is based on these volumes. The uncorrected peak value was combined with actual, 30% and 40% RECIST volumes.

Figure G - 4 compares the results using linear regression and the same criteria discussed in section 4.3.3, with results in **Table G - 4**, further assisted the comparison.

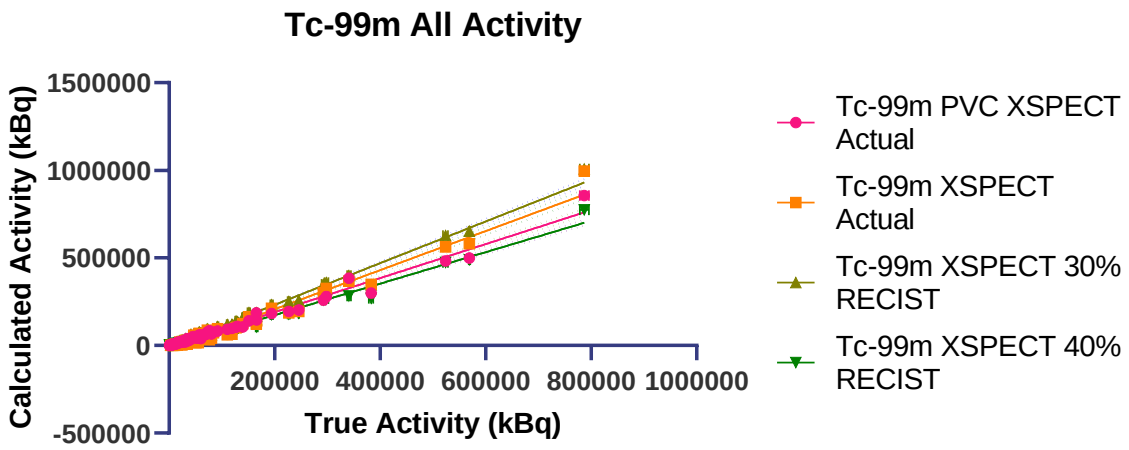

Figure G - 4 *Tc-99m XSPECT results with linear regressions for the selected most accurate volume and concentration combinations for activity results. The closer the fit to y = x, the better the accuracy.*

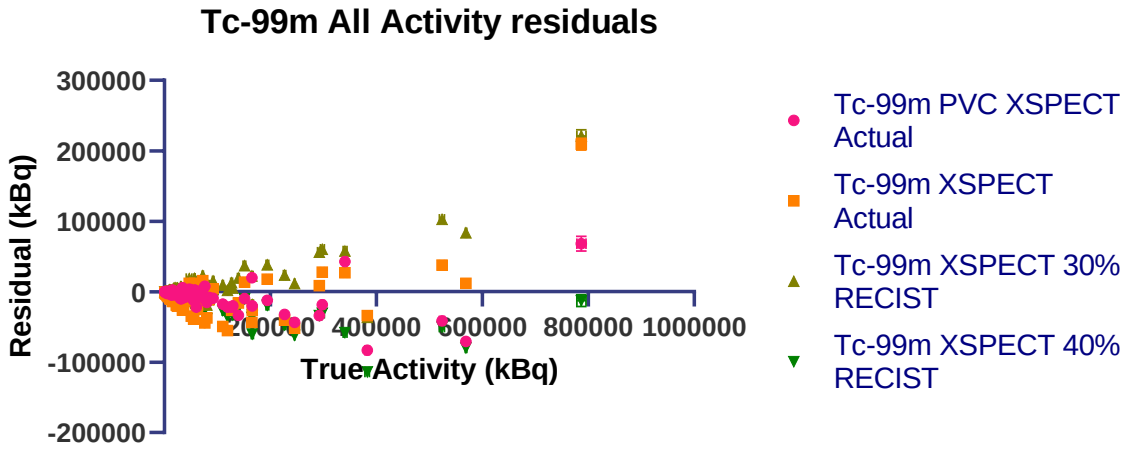

Figure G - 5 *Tc-99m XSPECT residuals for the selected most accurate volume and concentration combinations for activity results. The closer the residuals to zero, the more accurate the results.*

Table G - 4 *Linear equations, goodness of fit information and standard deviation of the residual with respect to y = x for the data in* ***Figure G - 4****.*

	Tc-99m PVC XSPECT Actual	Tc-99m XSPECT Actual	Tc-99m XSPECT 30% RECIST	Tc-99m XSPECT 40% RECIST
Equation	Y = 0.9701*X - 3521	Y = 1.115*X - 16116	Y = 1.189*X - 5840	Y = 0.8980*X - 6251
r-Squared	0.9824	0.9735	0.9888	0.9861
Sy.x	17353	24553	16886	14206
Residual Std Dev	17702	28791	30207	19565

The optimal results from **Table G - 4** are the Tc-99m PVC XSPECT Actual, based on the smallest residual standard deviation and closeness of the fit to y = x. The results for the Tc-99m XSPECT 40% RECIST are closer to the ideal than the same combination for Lu-177, the same as is used clinically. As previously discussed, a direct comparison cannot be made based on the results of this study.

Prior to the use of Lu-177, Tc-99m was used in the NEMA phantom for familiarisation with filling the phantom, scan protocol and reconstructions. The scan protocol was the same as that for Lu-177 except the stop conditions were set to 200 kCts per view instead of 40 kCts and only the XSPECT

reconstruction was of interest. The same Syngo.Via statistic, PVC methodology and volume-concentration combinations were applied. The PVC results with the actual volumes produced the most accurate activity results. No direct comparisons were made between the Tc-99m and Lu-177 results due to the differences in image quality owing to the difference in gamma energies, relative fluence, collimators and scan protocol.

Appendix H. Radiation Safety

The radiation safety concept, ALARA (As Low As Reasonably Achievable), was employed at all times. All work was carried out with others present in the department and available in case of emergency.

Training

The University of Western Australia Unsealed Radioisotope Handling Course was completed in 2014. This and extensive experience in handling and transporting unsealed radioisotopes during 7 years employment at the Department of Medical Technology & Physics, including many years working with the Nuclear Medicine therapy patients, was considered sufficient radiation safety training. In accordance with RSP-C-2-2019 (ARPANSA 2019) the necessary training to handle and transport unsealed radioactive material was met. For more detail on these requirements, please refer to Appendix E.

Shielding

All radioactivity was transported in shielding and labelled appropriately. This included the trolley to transport the phantom. All unsealed isotope handling was carried out behind shielding in either the well counter in the Nuclear Medicine laboratory, or a designated sink. The majority of the higher contamination risk work was performed at the sink. This area was not in regular use by the department and was equipped with extra precautions.

PPE

The floor was covered in absorbent and anti-slip Benchkote, with appropriate PPE use (Gloves, overshoes, lab coat) during all handling of unsealed sources.

Area Monitoring (Dose Rate and Contamination)

A contamination monitor was present at all times. This enabled swab testing for contamination on areas of isotope handling and the phantom once it was prepared. Additionally, there were contamination checks of personnel upon exit of the covered floor area. The monitor was dual purpose, able to measure counts/second and Sieverts/hour. Dose rates of all radioactivity containers were checked before transport.

The phantom was only transported when the camera was directly available for imaging to minimise others exposure. The phantom was transferred onto an absorbent bed protector on the camera bed. Once imaging was complete, the bed protector was disposed of and the bed monitored for any contamination.

Personnel Monitoring

As with all other unsealed radiation work, personnel have a monthly personal radiation dosimeter provided by GMS (Global Medical Solutions).

Waste management

All waste management was in agreement with Nuclear Medicine departmental standards. Dose rate of all waste was taken before storage in the Nuclear Medicine waste store and further shielded where appropriate.

The large volumes of weakly concentrated background fluid from the phantom (9 L extracted once per week) were stored in large secure receptacles.

Appendix I. Different exam types

Remaining statistic results discussed in section 4.3.1.2.

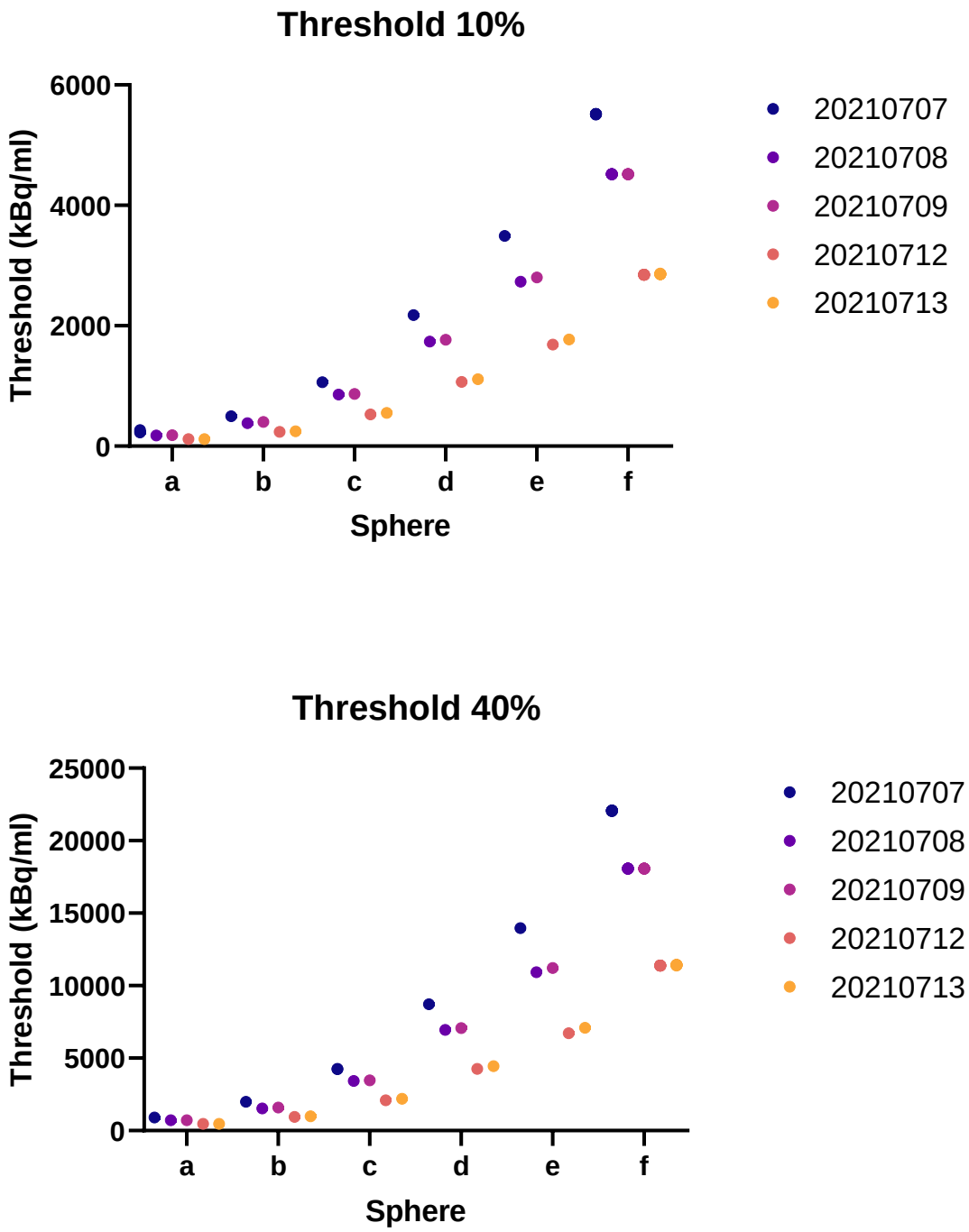

Figure I - 1 *Syngo.Via provided statistic Threshold for 10 and 40%. Each coloured dot contains the Syngo.Via provided volume for all 8 different exam types for a single sphere on a single date. As all dots appear unsmeared, this confirms that a change in exam type during reconstruction does not alter the Syngo.Via statistic, Threshold in this figure.*

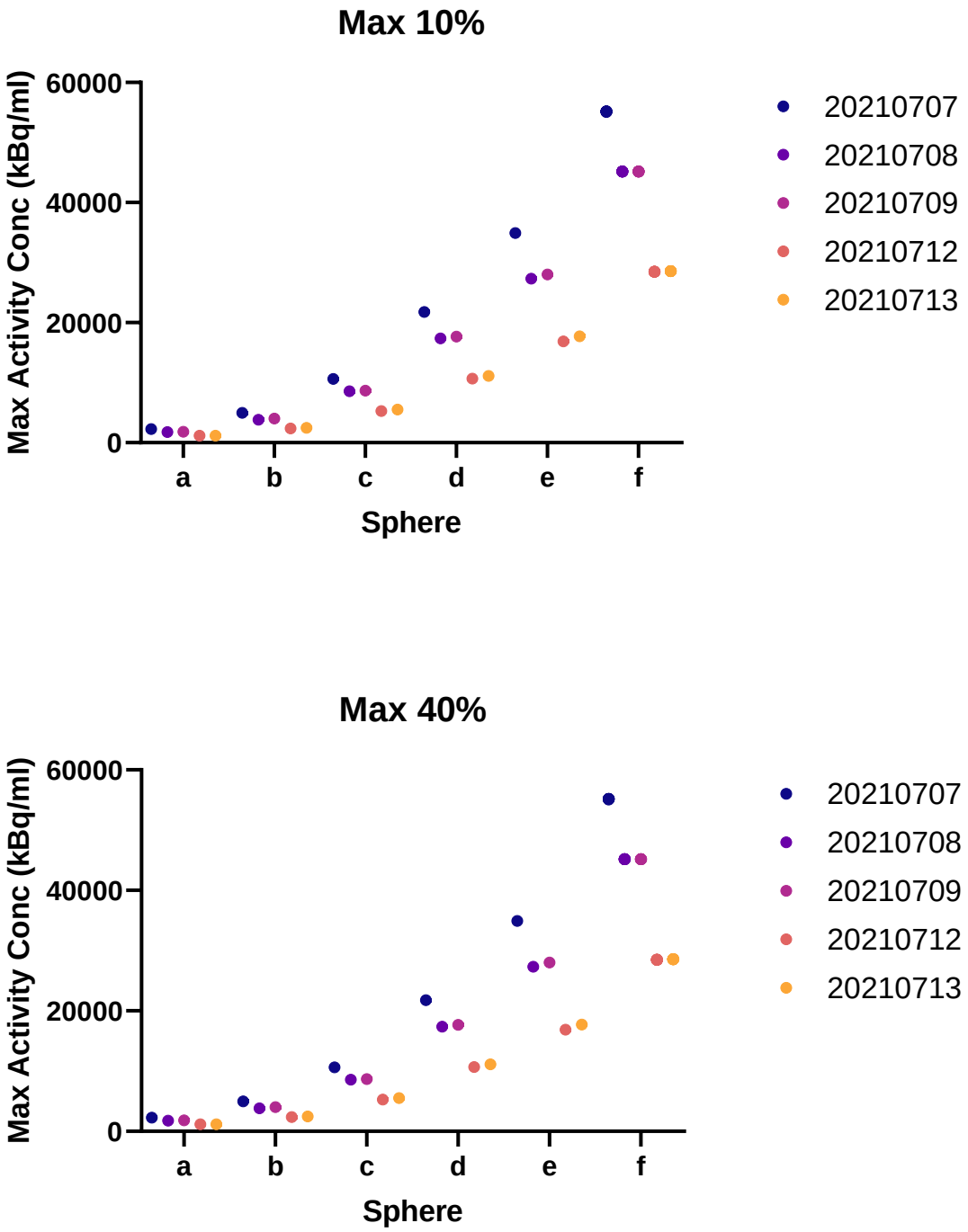

Figure I - 2 *Syngo.Via provided statistic Max kBq/ml for 10 and 40% RECIST thresholds. Each coloured dot contains the Syngo.Via provided volume for all 8 different exam types for a single sphere on a single date. As all dots appear unsmeared, this confirms that a change in exam type during reconstruction does not alter the Syngo.Via statistic, Max kBq/ml in this figure. This also does not change with a higher or lower RECIST threshold.*

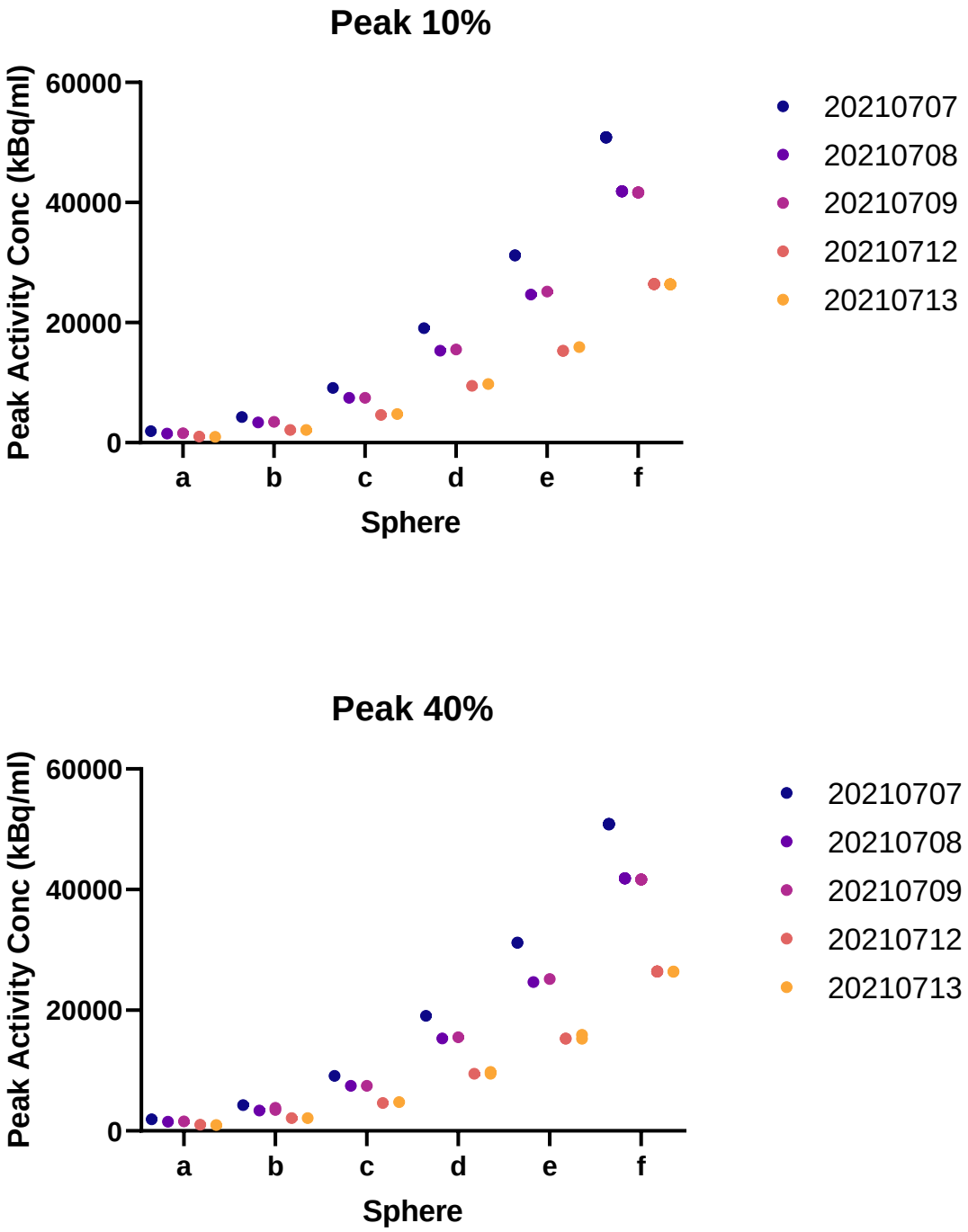

Figure I - 3 *Syngo.Via provided statistic Peak kBq/ml for 10 and 40% RECIST thresholds. Each coloured dot contains the Syngo.Via provided volume for all 8 different exam types for a single sphere on a single date. As all dots appear unsmeared, this confirms that a change in exam type during reconstruction does not alter the Syngo.Via statistic, Peak kBq/ml in this figure. This also does not change with a higher or lower RECIST threshold.*

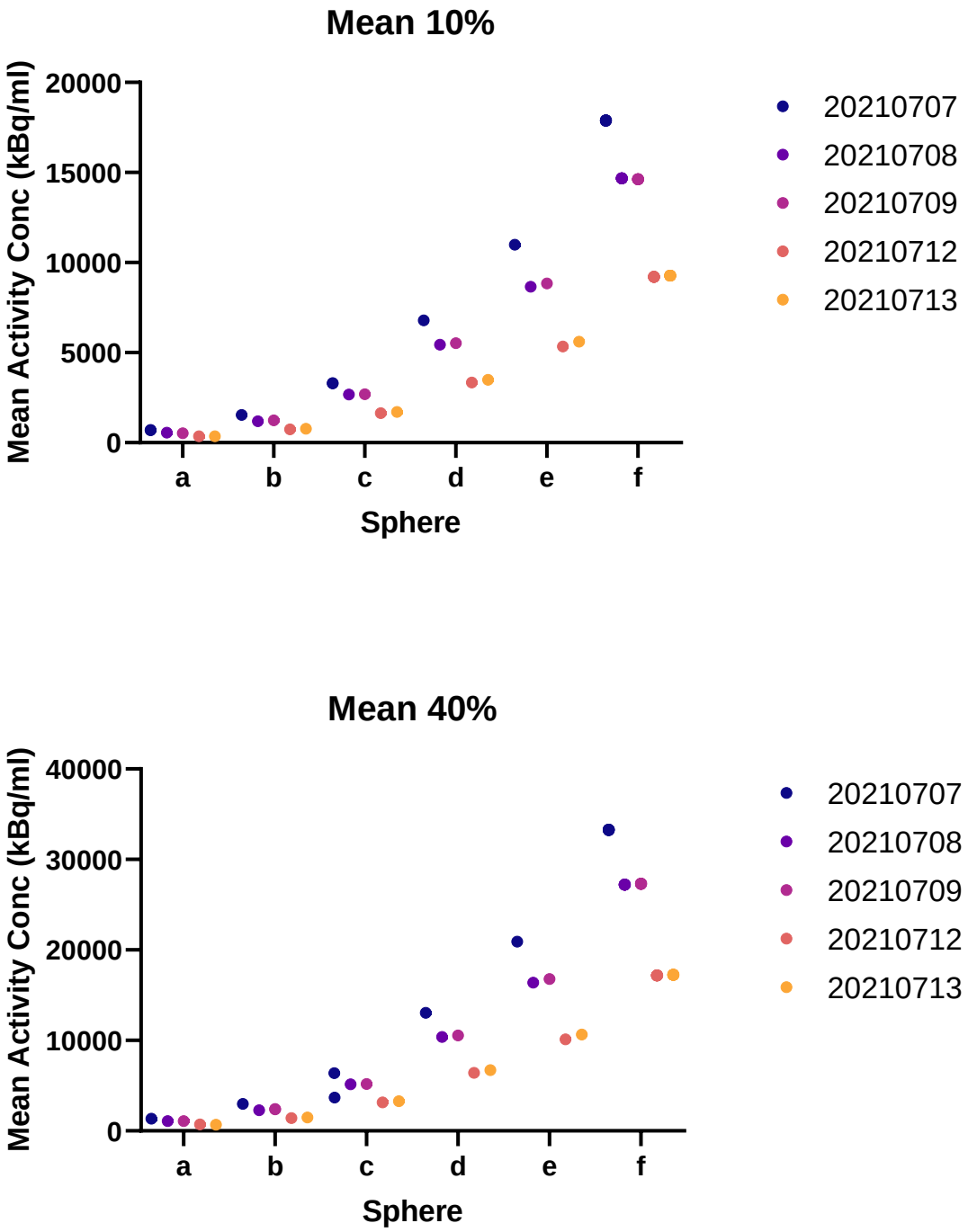

Figure I - 4 *Syngo.Via provided statistic Mean kBq/ml for 10 and 40% RECIST thresholds. Each coloured dot contains the Syngo.Via provided volume for all 8 different exam types for a single sphere on a single date. As all dots appear unsmeared, this confirms that a change in exam type during reconstruction does not alter the Syngo.Via statistic, Mean kBq/ml in this figure.*

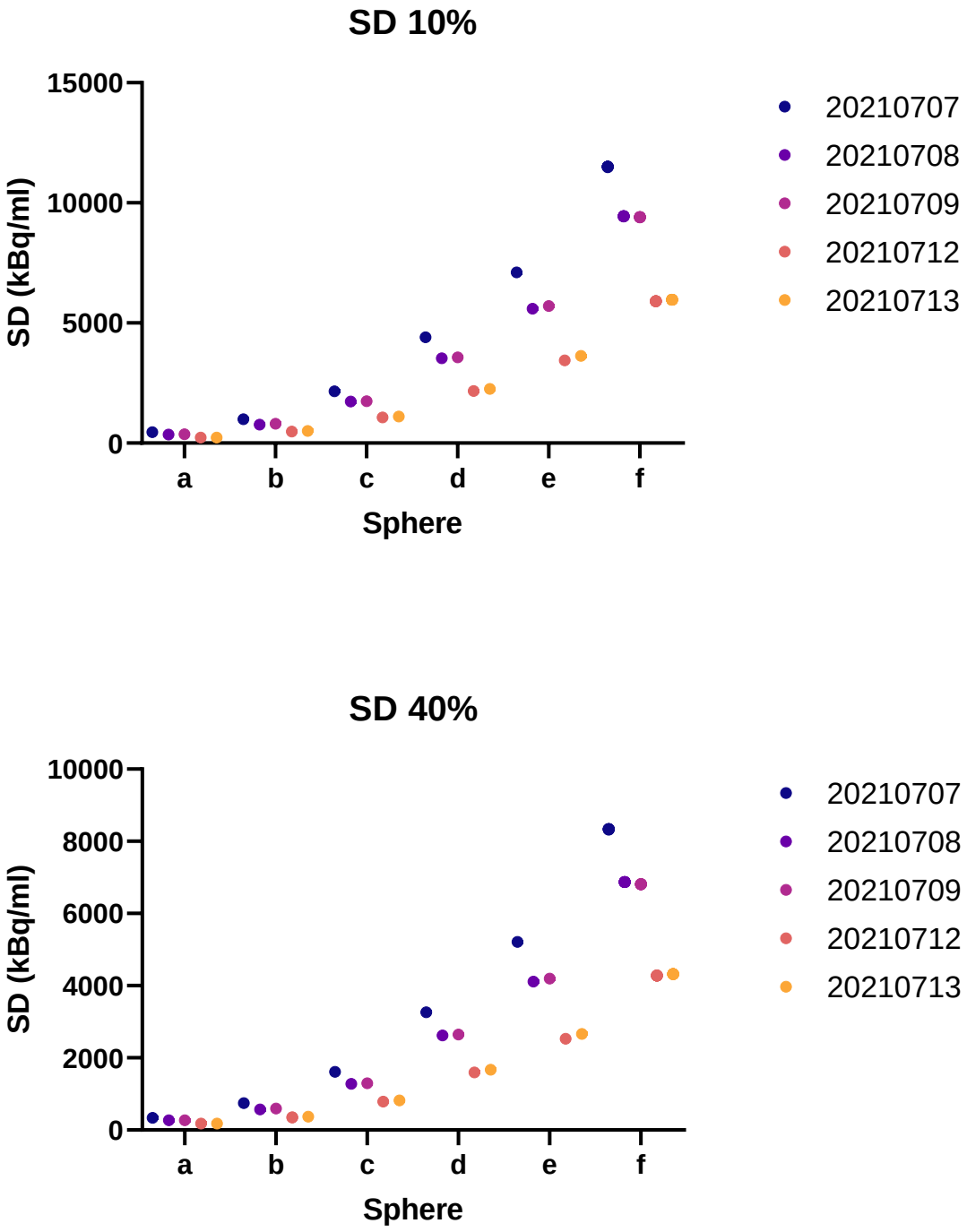

Figure I - 5 *Syngo.Via provided statistic SD (Standard Deviation) for 10 and 40% RECIST thresholds. Each coloured dot contains the Syngo.Via provided volume for all 8 different exam types for a single sphere on a single date. As all dots appear unsmeared, this confirms that a change in exam type during reconstruction does not alter the Syngo.Via statistic, SD in this figure.*

Appendix J. Uncertainty calculations

There are many sources of uncertainty throughout an experiment. Accounting for them is essential as they inform decisions about how data is used. For example, in section 4.3.1.3.2, the uncertainty in the data was too great to consider it for the basis of a correction. While this uncertainty was the only one discussed previously, uncertainty calculations were made on all data.

Lu-177 XSPECT Uncertainties

Lu-177 Syngo.Via XSPECT Output

As Siemens does not provide a standard deviation for the utilized Peak activity concentration (kBq/ml) value, the uncertainty is unknown. The standard deviation provided changes with the RECIST threshold, so this was likely related to the mean (since Peak does not change with threshold). The same applies to uncertainty in the volumes provided by Syngo.via. Due to the nature of this study, there were no repeated measurements of the same data point. This meant statistical uncertainty was not calculable since each point is a single value, not a mean. The statistical error relates to the repeatability (precision) of the results, which is not a concern for the peak activity concentration value, accuracy is.

Lu-177 Physically Measured and True Activity Concentration Values Uncertainty

The uncertainty in the true activity concentration (kBq/ml), determined from the well counter, volumes and decay correction, can be calculated. The capintec has a resolution uncertainty of ± 0.5 MBq or kBq (depending on the units displayed) and the syringe volume ± 0.5 ml when considering the sphere solution. These resolution uncertainties combined with the decay corrections, have been used to calculate the absolute uncertainty in the sphere concentrations, using **Equation J - 1**.

$$u_x = \frac{x_{max} - x_{min}}{2}$$

Equation J - 1

where u_x is the uncertainty in a value, in this case concentration, and x_{max} and x_{min} are the maximum and minimum possible values respectively. x_{max} and x_{min} are based on the resolution uncertainties for the activity and volume of the concentration. For example, an activity of 50 MBq would have an x_{max} of 50.5 MBq and an x_{min} of 49.5 MBq.

These uncertainties are displayed as horizontal error bars in **Figure J - 1**, the XSPECT Peak activity concentration values before PVC (Kirkup 2019). Due to the reasonable size of the uncertainty of each point in **Figure J - 1**, it was considered reasonable to base a PVC on this data as described in section 4.3.1.3.

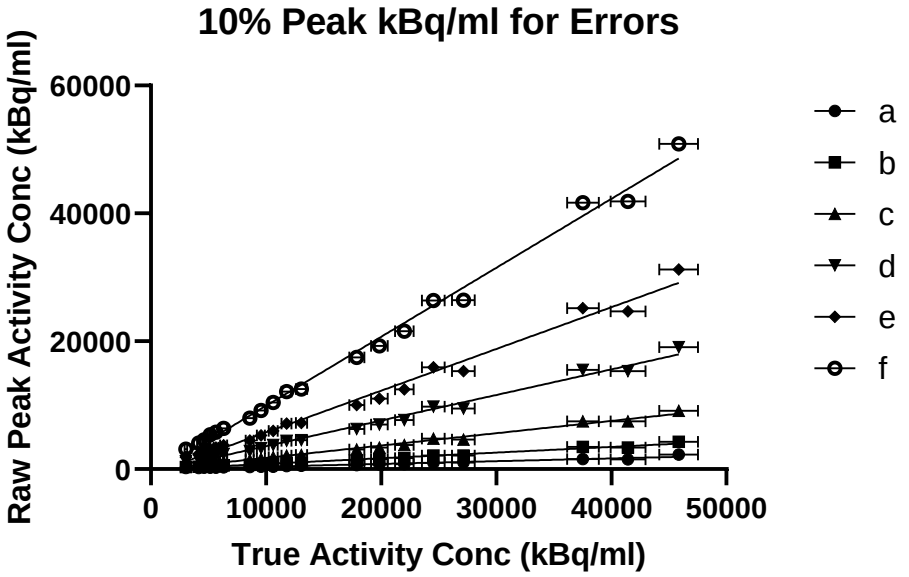

Figure J - 1 *Linear regressions of Raw Syngo.Via statistics Peak for a 10% RECIST threshold with individual linear regressions assigned to each sphere. The smallest sphere is labelled a and the largest is labelled f. This graph is identical to Figure 4-6 Peak but with added error bars.*

Lu-177 XSPECT $RC_{gradient}$ Uncertainty

The PVC uses the $RC_{gradient}$ discussed in section 4.3.1.3.1, which is based on the gradients of the linear fits for the Peak activity concentration graph in ***Figure 4-6****. The r-squared values for the Peak linear fits for* ***Figure 4-6*** *listed in*

Table 4-3 are high (all ≥ 0.96), and there are 19 data points used to create each graph. Prism provides the standard error for each of its fitted parameters, those for the gradient are listed in **Table J - 1**, which is assumed reliable based on the r-squared and number of data points.

Table J - 1 *Standard error of gradients in Figure 4-6 Peak from PRISM.*

Sphere	a	b	c	d	e	f
Slope SE	0.001930	0.002541	0.004622	0.01019	0.01805	0.02161

The standard error of the slope was entered as the standard deviation of each gradient value used to calculate the $RC_{gradient}$ as shown in **Table J - 2**.

Table J - 2 *Standard errors from* ***Table J - 1*** *entered into PRISM as standard deviation of each gradient.*

Sphere	Volume (cm^3)	Gradient	SD	N
a	0.52	0.0483	0.00193	19
b	1.15	0.0887	0.00254	19
c	2.57	0.193	0.00462	19
d	5.57	0.401	0.0102	19
e	11.5	0.653	0.0181	19
f	26.	1.08	0.0216	19

This allowed follow through of the error from the true activity concentration values to the formulated $RC_{gradient}$. *PRISM* offers only select options that will take error values into consideration when calculating the parameter fit and errors and the standard deviation is one such option (GraphPad 2017).

Standard error as standard deviation is acceptable. In *PRISM* all best fit parameters in a regression (linear or non-linear), the standard error and standard deviation are the same, it is only convention that labels it standard error (SE) (GraphPad 2009).

The $RC_{gradient}$ fit is displayed with error bars in **Figure J - 2**.

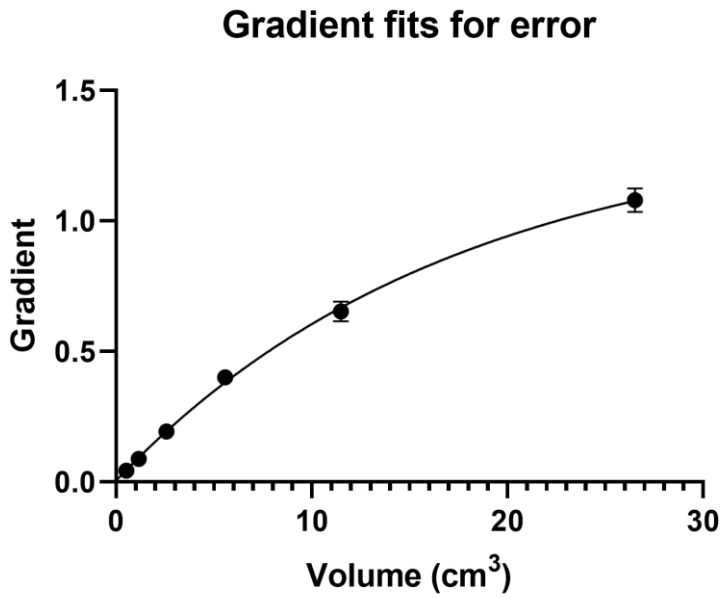

Figure J - 2 *The same as* ***Figure 4-7*** *Gradients from linear fits in* ***Figure 4-6*** *Peak plotted against the corresponding sphere volumes. Fitted with RC Equation 4-3. The 95% Confidence band is too close to the exponential fit to visualise but the 95% prediction band is visible and further indicates a good fit.) with error bars instead of confidence and prediction bands.*

Since the error bars in **Figure J - 2** are so small, they were not of concern and did not influence the use of the $RC_{gradient}$ for PVC. However, the fit 95% confidence or prediction bands are a better visual than the error bars. Prediction bands are further from the best-fit line than the confidence bands, a lot further if there are many data points. The 95% prediction band is the area in which you expect 95% of all data points to fall. In contrast, the 95% confidence band is the area that has a 95% chance of containing the true regression line (GraphPad 2022a). **Figure 4-7** confidence band is so close to the fitted line it is difficult to see, which is not the case for the predication band.

As discussed in section 4.3.1.3.1, the prediction band reaffirms the reliability of using the $RC_{gradient}$ for PVC. The prism reported standard error for each of the $RC_{gradient}$ fitted parameters is listed in **Table J - 3**.

Table J - 3 *Prism reported standard error for each $RC_{gradient}$ fitted parameter.*

Constant	Value	SEM
c	1.374	0.015
a	1.369	0.014
b	0.058	0.001

The parameters and their standard error in **Table J - 3** for $RC_{gradient}$ were used to determine the uncertainty in the PVC Peak activity concentration (PVC_{peak}) values.

Lu-177 XSPECT PVC_{peak} Activity Concentration Uncertainty

The previous uncertainties utilise basic arithmetic via **Equation J - 1**, or through providing *PRISM* with the error parameters. Calculation of the PVC_{peak} (**Equation J - 2**) values were performed in excel, since this was not a statistical analysis. Due to the multiple parameters and more complex calculation, rather than **Equation J - 1**, the partial derivative method in **Equation J - 3** was used to calculate the uncertainty.

$$PVC_{peak} = \frac{Peak}{c - ae^{-bVol}}$$

Equation J - 2

$$u_{PVC_{peak}} = \sqrt{\left(\frac{\partial PVC_{peak}}{\partial c}\right)^2 u_c^2 + \left(\frac{\partial PVC_{peak}}{\partial a}\right)^2 u_a^2 + \left(\frac{\partial PVC_{peak}}{\partial b}\right)^2 u_b^2}$$

Equation J - 3

where $u_{PVC_{peak}}$ is the uncertainty in the PVC Peak activity concentration (PVC_{Peak}), u_a u_b u_c are the uncertainty in parameters *a b* and *c* respectively, and $\frac{\partial PVC_{peak}}{\partial a}$ $\frac{\partial PVC_{peak}}{\partial b}$ $\frac{\partial PVC_{peak}}{\partial c}$ are the partial derivatives of **Equation 4-4** with respect to parameters *a b* and *c* respectively. The standard error provided by Prism in **Table J - 3** for each parameter were used as u_a u_b u_c (Kirkup 2019). The partial derivatives of **Equation J - 3** are **Equation J - 4**, **Equation J - 5** and **Equation J - 6** respectively.

$$\frac{\partial PVC_{peak}}{\partial c} = \frac{-Peak}{(c - ae^{-b\,Vol})^2}$$

Equation J - 4

$$\frac{\partial PVC_{peak}}{\partial a} = \frac{e^{b\,Vol} Peak}{(a - ce^{b\,Vol})^2}$$

Equation J - 5

$$\frac{\partial PVC_{peak}}{\partial b} = \frac{-a\,Vol\;Peak\;e^{b\,Vol}}{(ce^{b\,Vol} - a)^2}$$

Equation J - 6

The resulting uncertainty for each PVC_{Peak} value using **Equation J - 3** were entered into prism as ± error to achieve the vertical error bars in in **Figure 4-10**, the horizontal error bars are the same as those in **Figure J - 1**.

Any uncertainty in concentration is relatively amplified with decreasing sphere size. This is reflected in **Figure 4-10**s error bars for the smallest sphere. When considering the maximum and minimum of the error bars for sphere 'a', the correction has still made an improvement. The process was similar for the 3D Flash data uncertainties, but contained extra sources of uncertainty due to the added steps.

Lu-177 3D FLASH Uncertainties

Lu-177 Bottle Phantom Calibration Curve Uncertainties

As described in section 4.3.2, the bottle phantom was measured once a week and three VOI were taken to form the calibration curve. The calibration curve consists of average count rate ($\overline{CR}$) on the x-axis and true activity concentration (kBq/ml) on the y-axis. Both have associated uncertainty.

The true kBq/ml have an absolute uncertainty resulting from the capintec and volume measuring instruments, calculated using **Equation J - 1**. These values were entered into Prism as the standard deviation on the true activity concentration (kBq/ml) to carry through their uncertainty to the calibration curve resulting in **Figure 4-12** horizontal error bars.

The $\overline{CR}$ is from repeated VOIs on each image depicted in **Figure 4-11** discussed section 4.3.2. Therefore, uncertainty for each point was taken as the standard deviation of the samples, resulting in the vertical error bars in **Figure 4-12**.

The uncertainty in the number of counts is not incorporated. The same as discussed for **Lu-177 Syngo.Via XSPECT Output**, the focus of the uncertainty is on the calibrations and transformations this study produced and applied, rather than the raw data Syngo.Via produces. However, the repeated measurements allow for statistical error, the standard deviation of each point creating the vertical error bars in **Figure 4-12**. These vertical error bars are too small to visualise and the horizontal are only visible with very small point markers.

These vertical and horizontal errors are carried through in *PRISM* to the uncertainties in the calibration curve in **Figure 4-12** (the linear regression), listed as the slope and intercepts standard error in **Table J - 4**.

Table J - 4 *PRISM provided standard error of the slope and intercept of the linear fit for a calibration curve in* ***Figure 4-12****.*

	Std. Error
Slope	3156297
Y-intercept	366.1

Lu-177 Calibration Curve Produced Raw Activity Concentration Data

The uncertainty in the bottle phantom calibration curve (**Equation J - 7**), is propagated to the resulting raw activity concentration (kBq/ml) data in **Figure 4-13** using the partial derivative method in **Equation J - 8**.

$$ {}^{kBq}/_{ml} = m\,CR + c $$

Equation J - 7

where *m* is the slope of the fit and *c* is the intercept.

$$ u_{\frac{kBq}{ml}} = \sqrt{\left(\frac{\partial\, {}^{kBq}/_{ml}}{\partial m}\right)^2 u_m^2 + \left(\frac{\partial\, {}^{kBq}/_{ml}}{\partial c}\right)^2 u_c^2} $$

Equation J - 8

where $u_{\frac{kBq}{ml}}$ is the uncertainty in the 3D Flash activity concentration (kBq/ml) data, $\frac{\partial kBq/ml}{\partial m}$ and $\frac{\partial kBq/ml}{\partial c}$ are the partial derivatives of **Equation J - 7** with respect to m and c described by **Equation J - 9** and **Equation J - 10** respectively, u_m and u_c are the uncertainty in *m* and *c*.

$$ \frac{\partial\, {}^{kBq}/_{ml}}{\partial m} = CR $$

Equation J - 9

$$ \frac{\partial\, {}^{kBq}/_{ml}}{\partial c} = 1 $$

Equation J - 10

The standard error in **Table J - 4** were taken as u_m and u_c. The resulting uncertainties from **Equation J - 8** are the vertical error bars in **Figure 4-13**. The horizontal error bars are identical to that in **Figure J - 1** as the true activity concentration (kBq/ml) is the same. These uncertainties in **Figure 4-13** indicated it was reasonable to base a PVC on this data as described in section 4.3.2.1.

Lu-177 3D Flash $RC_{gradient}$ Uncertainty

The PVC again uses the $RC_{gradient}$, which is based on the gradients of the linear fits in **Figure 4-13**. The r-squared values for the Peak linear fits for **Figure 4-13** listed in **Table 4-8** are high (all ≥ 0.98), and there are 19 data points used to create each graph. Prism provides the standard error for each of its fitted parameters, those for the gradient are listed in **Table J - 5**, which is assumed reliable based on the r-squared and number of data points.

Table J - 5 *Prism provided standard errors for linear fits in* ***Figure 4-13****.*

Std. Error	a	b	c	d	e	f
Slope	0.003645	0.008492	0.01771	0.03202	0.05019	0.07055
Y-intercept	77.08	179.6	374.6	677.3	1061	1492

As with the XSPECT $PVC_{gradient}$, the standard error of the slope was entered as the standard deviation of each gradient value used to calculate the $RC_{gradient}$ as shown in **Table J - 6**.

Table J - 6 *Standard errors from* ***Table J - 5*** *entered into PRISM as standard deviation of each gradient.*

Sphere	Volume (cm^3)	Gradient	SD	N
a	0.52	0.126	0.00365	19
b	1.15	0.311	0.00849	19
c	2.57	0.665	0.0177	19
d	5.57	1.30	0.0320	19
e	11.5	2.08	0.0501	19
f	26.5	2.90	0.0706	19

This allowed follow through of the error from the true activity concentration (kBq/ml) values to the formulated $RC_{gradient}$. The $RC_{gradient}$ fit is displayed with error bars in **Figure J - 3**.

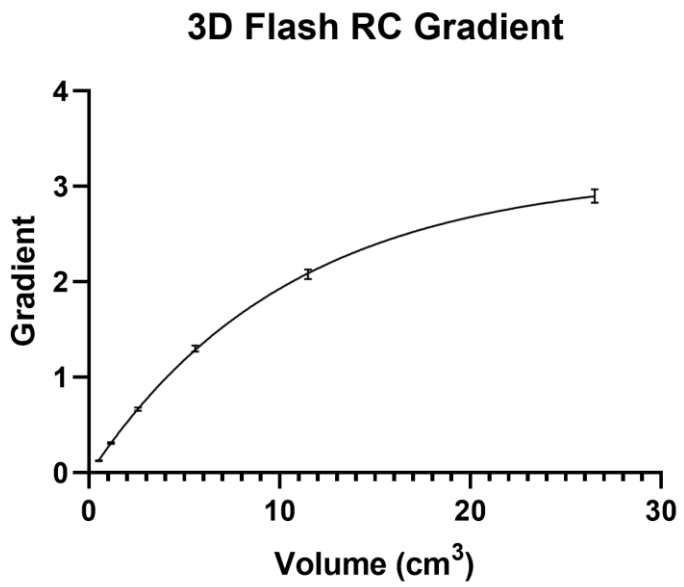

Figure J - 3 *The same as* ***Figure 4-14*** *Gradients from linear fits in Figure 4-13 plotted against the corresponding sphere volumes. Fitted with RC Equation 4-3. The 95% Confidence band is too close to the exponential fit to visualise but the 95% prediction band is visible and further indicates a good fit. with error bars instead of confidence and prediction bands.*

The resulting error bars in **Figure J - 3** are so small, they were not of concern and did not influence the use of the $RC_{gradient}$ for PVC. As with the XSPECT $RC_{gradient}$, the confidence band in **Figure 4-14** is so close to the fitted line it is difficult to see, which is not the case for the predication band. The prediction band reaffirms the validity of using the $RC_{gradient}$ for PVC. The prism reported standard error for each of the $RC_{gradient}$ fitted parameters is listed in **Table J - 7**.

Table J - 7 *Prism reported standard error for each* $RC_{gradient}$ *fitted parameter.*

Constant	Value	SEM
c	3.148	0.016
a	3.171	0.015
b	0.095	0.001

Lu-177 3D Flash PVC_{peak} Activity Concentration Uncertainty

Using the same method as for **Lu-177 XSPECT PVC_{peak} Activity Concentration Uncertainty**, the **Table J - 7** standard error for each fitted parameter and the partial derivatives method using **Equation J - 3**, the uncertainty for the PVC_{peak} was calculated. Identical to XSPECT, the resulting

$u_{PVC_{peak}}$ were entered as ± error of the $PVC_{gradient}$ into *PRISM* to create the vertical error bars in **Figure 4-15**. The horizontal error bars are the same as those in **Figure J - 1** as the true activity concentration (kBq/ml) is unchanged.

The uncertainties calculated for both XSPECT and 3D Flash $PVC_{gradient}$ data was propagated through the activity kBq results.

Lu-177 Activity Based Results Uncertainties

Lu-177 Activity Result Uncertainty

All activity-based result in kBq (**Equation J - 11**) uncertainties, as opposed all previously discussed which were concentration based in kBq/ml, were calculated using the partial derivative method in **Equation J - 12**.

$$Activity = kBq/ml \times Vol$$

Equation J - 11

where *Activity* is the activity in kBq in the object of interest, *kBq/ml* is the concentration and *Vol* the volume it is combined with (actual, 30% RECIST etc.).

$$u_{Activity} = \sqrt{\left(\frac{\partial Activity}{\partial\, kBq/ml}\right)^2 u_{kBq/ml}^2}$$

Equation J - 12

$$\frac{\partial Activity}{\partial\, kBq/ml} = Vol$$

Equation J - 13

where $u_{Activity}$ is the uncertainty in the activity, $u_{kBq/ml}$ is the uncertainty in the concentration and $\frac{\partial Activity}{\partial kBq/ml}$ is the partial derivative of **Equation J - 11** with respect to concentration as **Equation J - 13**. The entered $u_{kBq/ml}$ for partial volume corrected data are the $u_{PVC_{peak}}$s discussed in **3D Flash PVC_{peak} Activity Concentration Uncertainty** and **XSPECT PVC_{peak} Activity Concentration Uncertainty**. Those not partial volume corrected do not have a $u_{kBq/ml}$.

These $u_{Activity}$ uncertainties were entered into prism as the standard deviation of the Activity values discussed in section 4.3.3 to produce the vertical error bars in **Figure 4-18**.

The uncertainty of the residual from section 4.3.3 was also calculated.

Lu-177 Activity Residuals Uncertainty

The uncertainty in **Equation J - 14** was calculated using the partial derivative method in **Equation J - 15**.

$$Residual = True - Calculated$$

Equation J - 14

where *True* is the true activity in kBq quantity in the phantom and *Calculated* is the various Syngo.Via derived results (such as PVC XSPECT Actual or 3D Flash 30% RECIST results).

$$u_{residual} = \sqrt{\left(\frac{\partial Residual}{\partial True}\right)^2 u_{True}^2 + \left(\frac{\partial Residual}{\partial Calculated}\right)^2 u_{Calculated}^2}$$

Equation J - 15

where $u_{residual}$ is the uncertainty in the residual, $\frac{\partial Residual}{\partial True}$ and $\frac{\partial Residual}{\partial Calculated}$ are the partial derivatives of **Equation J - 14** with respect to *True* and *Calculated* described by **Equation J - 16** and **Equation J - 17** respectively, u_{True} and $u_{Calculated}$ are the uncertainty in *True* (still the same as the horizontal error bars in **Figure J - 1**) and *Calculated* ($u_{Activity}$ *results)*.

$$\frac{\partial Residual}{\partial True} = 1$$

Equation J - 16

$$\frac{\partial Residual}{\partial Calculated} = -1$$

Equation J - 17

These resulting uncertainties are displayed as the vertical error bars in **Figure 4-19**. The horizontal error bars are, again, unchanged from **Figure J - 1**.

While it is clear in **Figure 4-19** that the error on most 3D flash results is relatively larger than that of the XSPECT, **Figure J - 4** offers clearer visualisation of the three most accurate results, in which it becomes clearer why XSPECT 30% RECIST was the superior result.

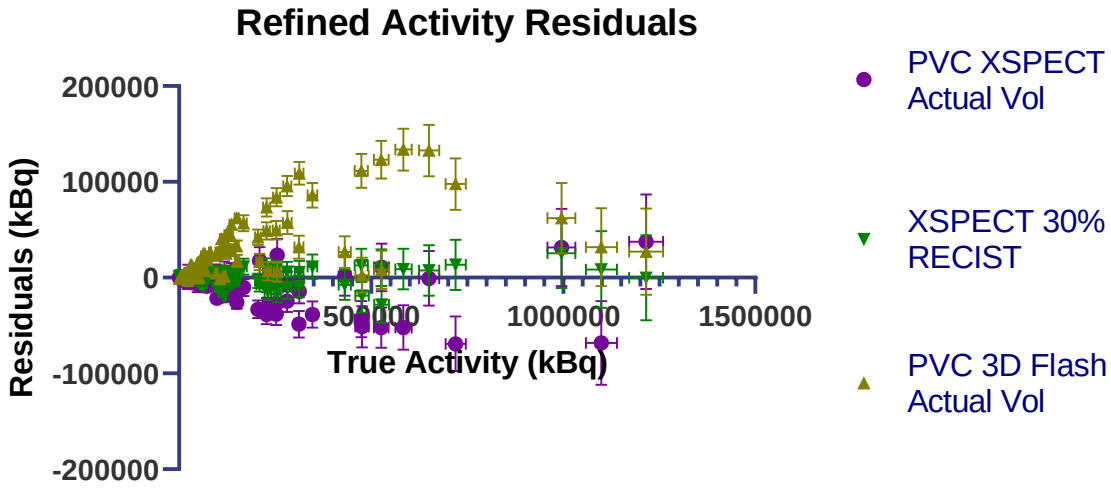

Figure J - 4 *Residuals of three most accurate results for clearer visualisation of single most accurate result.*

The included errors did not change the conclusions and advice derived. Based on linear equation fits, r-squared values and standard deviation of residuals, XSPECT results are still preferred and 30% RECIST is still suggested as the new RECIST threshold.

Lu-177 Planar Uncertainties

Lu-177 Planar Bottle Phantom

To create the error bars in **Figure 4-26**, the uncertainty for the known activity and average count rate were entered into *PRISM*. The known activity uncertainty was calculated using **Equation J - 1** using the absolute method with results from the well counter and volume measurements. The average count rate uncertainty was the standard deviation of the count rate for the anterior and posterior views. This data was entered as shown in **Table J - 8**.

Table J - 8 *PRISM entered data for* ***Figure 4-26*** *(planar bottle calibration curve).*

Average CR	Err. Bar	Activity (MBq)	SD	N
33854	271	6106	1.54	1
18828	113	3266	0.824	1
9192	64.9	1580	0.399	1
4888	33.9	843	0.213	1
2143	19.8	329	0.0830	1
1276	12.3	217	0.0547	1

The average count rate uncertainty formed the horizontal error bars of **Figure 4-26**, while the uncertainty in the activity formed the vertical error bars. The resulting error bars in were so small, they did not influence the decision to use the calibration curve.

These errors were carried through in *PRISM* to the uncertainties in the calibration curve in (the linear regression), listed as the slope and intercepts standard error in **Table J - 9**.

Table J - 9 *PRISM provided standard error of the slope and intercept of the linear fit for a calibration curve in* ***Figure 4-26***

	Std. Error
Slope	0.00230
Y-intercept	37.8

Lu-177 Planar NEMA Phantom

The uncertainty for the calibration curve (linear fit in **Figure 4-26**), **Equation J - 18**, was propagated through the calculated activity in the NEMA phantom using the partial derivative method in **Equation J - 19**.

$$MBq = m\,CR + c$$

Equation J - 18

where *m* is the gradient, *c* is the intercept and *CR* is the count rate.

$$u_{Planar\ kBq} = \sqrt{\left(\frac{\partial Planar\ kBq}{\partial m}\right)^2 u_m^2 + \left(\frac{\partial Planar\ kBq}{\partial CR}\right)^2 u_{CR}^2 + \left(\frac{\partial Planar\ kBq}{\partial c}\right)^2 u_c^2}$$

Equation J - 19

Where $u_{Planar\ kBq}$ is the uncertainty in the calculated planar activity, u_m u_{CR} u_c is the uncertainty in the gradient, count rate and intercept respectively. u_m and u_c were taken from the standard error of each provided by prism in **Table J - 9**, while u_{CR} was the standard deviation of the average. $\frac{\partial Planar\ kBq}{\partial m}$

$\frac{\partial Planar\ kBq}{\partial CR}$ $\frac{\partial Planar\ kBq}{\partial c}$ are the partial derivatives of **Equation J - 18** with respect to *m*, *CR* and *c* as represented by **Equation J - 20**, **Equation J - 21** and **Equation J - 22**.

$$\frac{\partial Planar\ kBq}{\partial m} = CR$$

Equation J - 20

$$\frac{\partial Planar\ kBq}{\partial CR} = m$$

Equation J - 21

$$\frac{\partial Planar\ kBq}{\partial c} = 1$$

Equation J - 22

The result is **Figure 4-27** vertical error bars which confirm the source of inaccuracy lies with the lack of applied corrections discussed in section 4.3.5.

Tc-99m Uncertainties

While the Tc-99m incorporated residuals, as discussed in Appendix G, the uncertainties calculations were identical to those described for XSPECT Lu-177.

Tc-99m Measured and True Values Uncertainty

The uncertainties in the Tc-99m data, prior to PVC, were calculated the same way as the description for **Lu-177 Physically Measured and True Values Uncertainty**. The uncertainties appear as the horizontal error bars for true activity concentration (kBq/ml) in **Figure G - 1**.

Tc-99m $RC_{gradient}$ Uncertainty

The PVC uses the $RC_{gradient}$ in the same manner applied to the Lu-177 data discussed in section 4.3.1.3.1, which is based on the gradients of the linear fits for the Peak graph in **Figure G - 1**. The r-squared values for the Peak linear fits for **Figure G - 1** listed in **Table G - 1** are high (all ≥ 0.94), and there are 15 data points used to create each graph. *PRISM* provides the standard error for each of its fitted parameters, those for the gradient are listed in **Table J - 10**, which is assumed reliable based on the r-squared and number of data points.

Table J - 10 *Standard error of gradients in* ***Figure G - 1*** *Peak from PRISM.*

Sphere	a	b	c	d	e	f
Slope SE	0.007373	0.01373	0.02328	0.03856	0.05360	0.05131

The standard error of the slope was entered as the standard deviation of each gradient value used to form the $RC_{gradient}$ in ***Figure G - 2***. This allowed follow through of the error from the true activity concentration values to the formulated $RC_{gradient}$.

The error bars in ***Figure G - 2*** were small enough to not influence the use of the $RC_{gradient}$ for PVC. The prediction band on the same graph reaffirms the reliability of using the RCgradient for PVC. The *PRISM* reported standard error for each of the $RC_{gradient}$ fitted parameters is listed in **Table J - 11**.

Table J - 11 *Prism reported standard error for each RCgradient fitted parameter for Tc-99m.*

Constant	Value	SEM
c	1.194	0.008
a	1.162	0.008
b	0.139	0.003

The parameters and their standard error in **Table J - 11** for $RC_{gradient}$ were used to determine the uncertainty in the Tc-99m PVC_{peak} activity concentration values.

Tc-99m PVC_{peak} Activity Concentration Uncertainty.

Calculation of the Tc-99m PVC_{peak} activity concentration values were performed the same way as those for XSPECT PVC_{peak} activity concentration when considering Lu-177. The partial derivative method in **Equation J - 3** was again used to calculate the uncertainty. This formed the vertical error bars in **Figure G - *3***. The horizontal error bars are the same as those in **Figure G - 1**, since the true activity concentration is unchanged.

Tc-99m Activity Based Results

The uncertainties in the Activity (kBq) results were calculated the same as that described for Lu-177 **Activity Result Uncertainties**. The $u_{Activity}$ uncertainties were entered into prism as the standard deviation of the Activity values to produce the vertical error bars in **Figure G - 4**. The horizontal error bars remain the same as those in **Figure G - 1** (the true activity remaining unchanged). The error bars are very small and did not change the validity of the results.

Tc-99m Activity Residuals Uncertainty

The uncertainties in the activity residual results were calculated the same as that described for Lu-177 **Activity Residuals Uncertainties**. These resulting uncertainties are displayed as the vertical error bars in **Figure G - 5**. The horizontal error bars are, again, unchanged from **Figure G - 1**.

Appendix K. Background concentrations

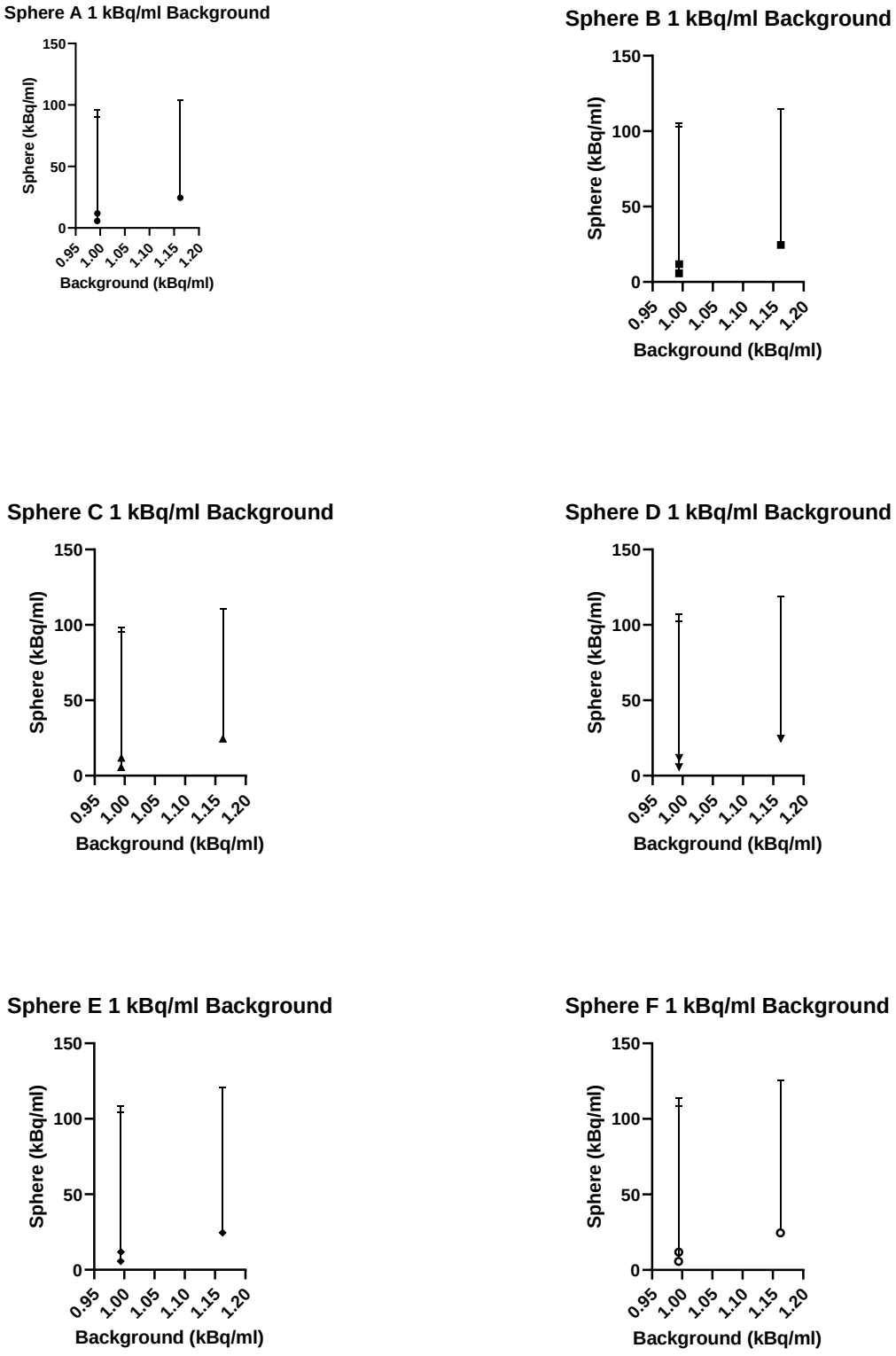

Figure K - 1 *Sphere concentration (MBq/ml) vs Background concentration (kBq/ml) for all spheres ('a' through 'f') for a 1 kBq/ml background concentration. Each graph represents a separate sphere and the error bars are the percentage error. As the Sphere concentration decreases, the error bars become longer.*

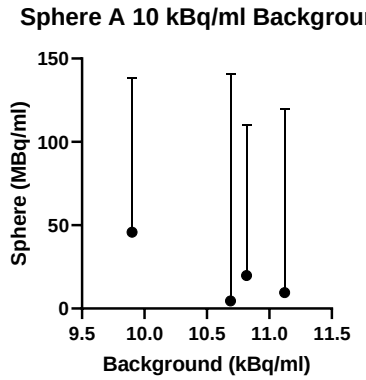

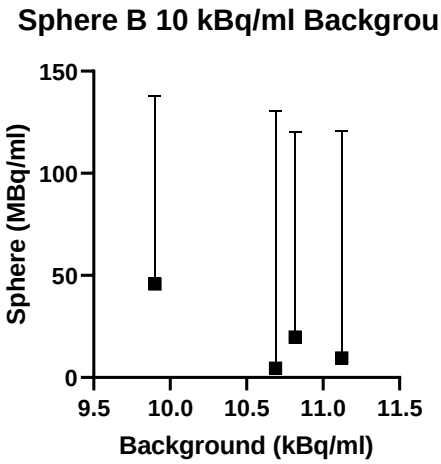

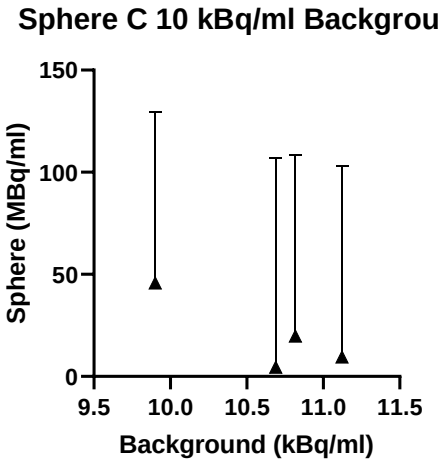

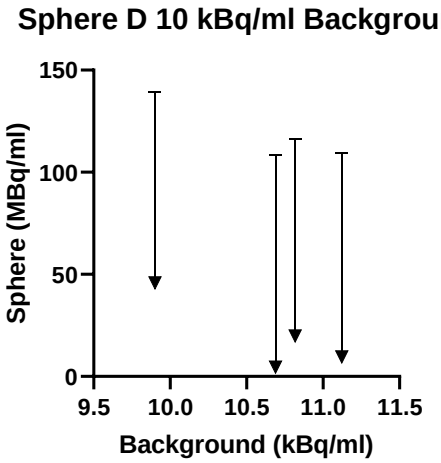

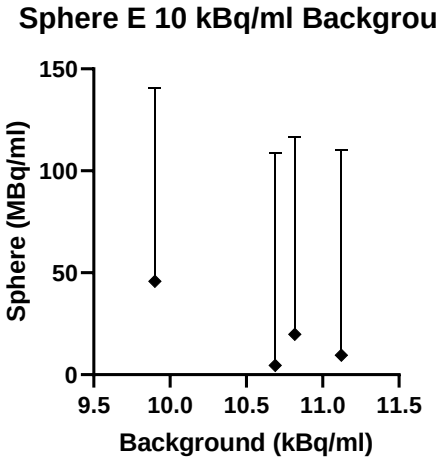

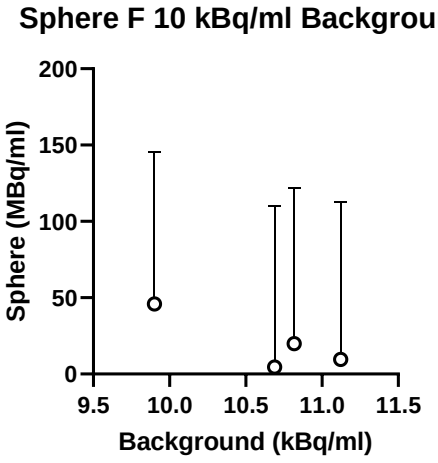

Figure K - 2 *Sphere concentration (MBq/ml) vs Background concentration (kBq/ml) for all spheres ('a' through 'f') for a 10 kBq/ml background concentration. Each graph represents a separate sphere and the error bars are the percentage error. As the Sphere concentration decreases, the error bars become longer.*

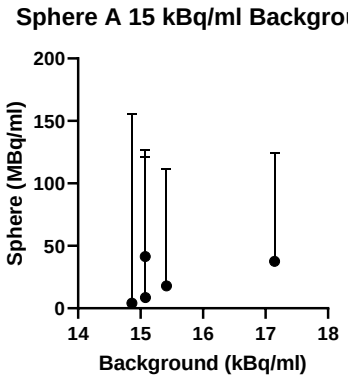

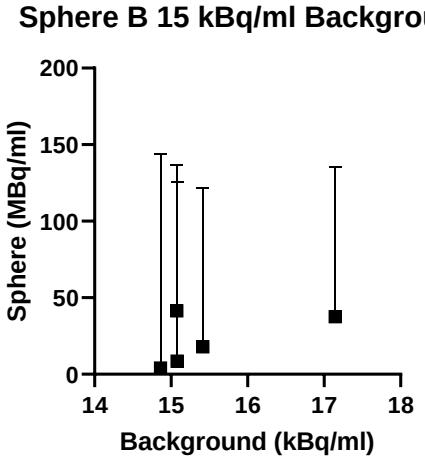

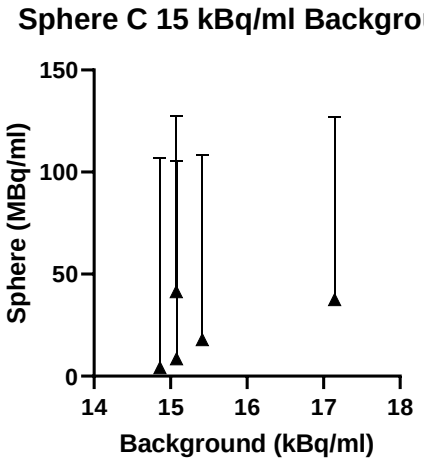

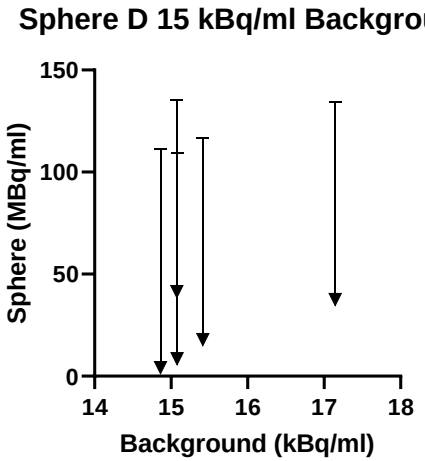

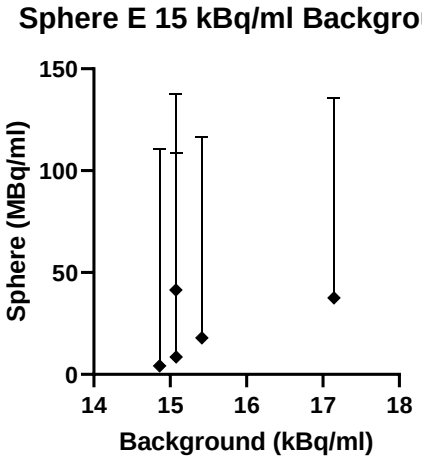

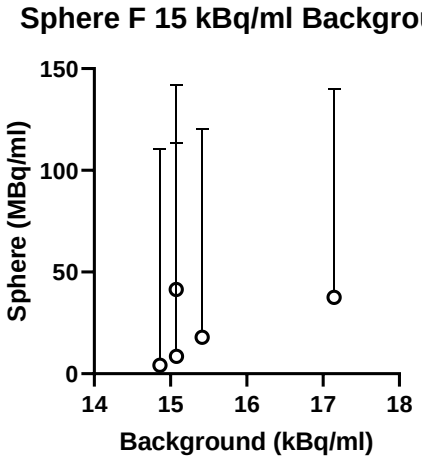

Figure K - 3 *Sphere concentration (MBq/ml) vs Background concentration (kBq/ml) for all spheres ('a' through 'f') for a 15 kBq/ml background concentration. Each graph represents a separate sphere and the error bars are the percentage error. As the Sphere concentration decreases, the error bars become longer.*

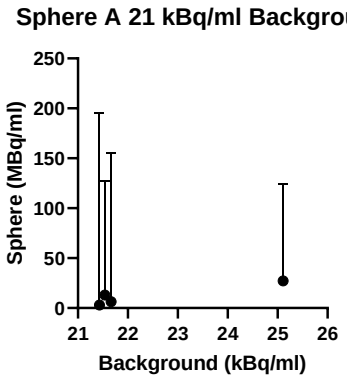

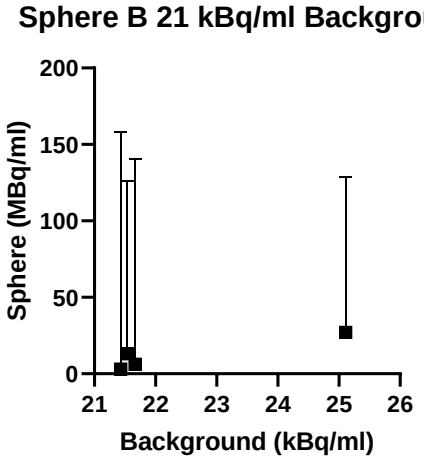

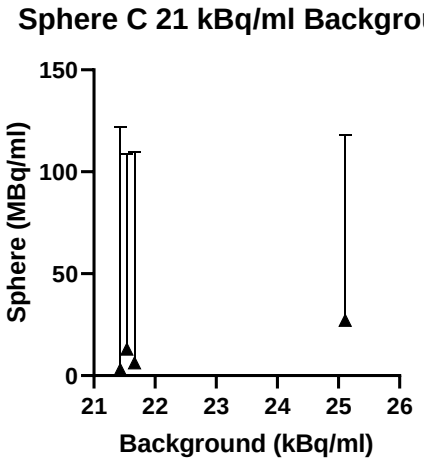

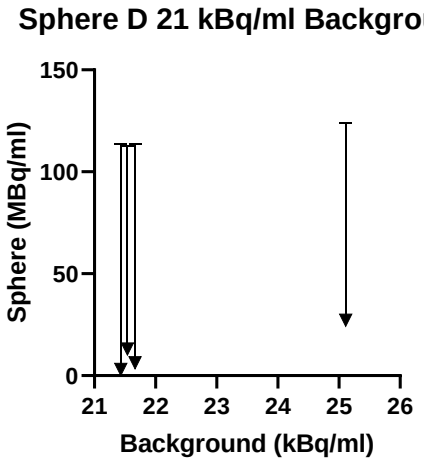

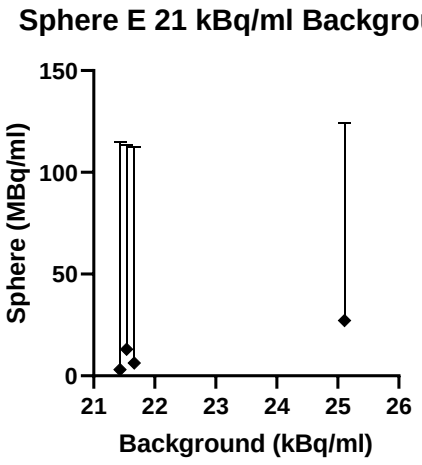

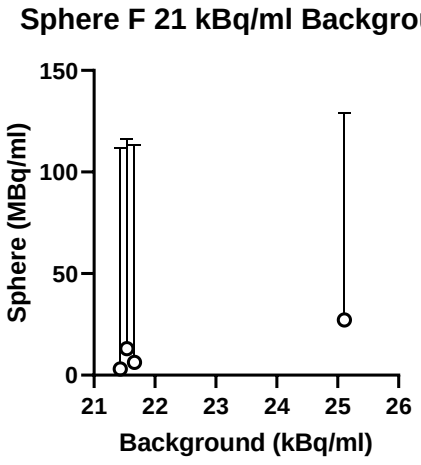

Figure K - 4 *Sphere concentration (MBq/ml) vs Background concentration (kBq/ml) for all spheres ('a' through 'f') for a 21 kBq/ml background concentration. Each graph represents a separate sphere and the error bars are the percentage error. As the Sphere concentration decreases, the error bars become longer.*

References

(NIST), NIoSaT 2018, *Radioactivity Standard Reference Material Program*, National Institute of Standards and Technology (NIST), 100 Bureau Drive

Gaithersburg, MD 20899

301-975-2000, viewed 5th December 2019, <https://www.nist.gov/programs-projects/radioactivity-standard-reference-material-program>.

AAPM-TG177 2019, *Acceptance Testing and Annual Physics Survey Recommendations for Gamma Camera, SPECT, and SPECT/CT Systems*, AAPM report No.177, American Association of Physicists in Medicine, 1631 Prince Street, Alexandria, VA 22314.

Abuqbeitah, M, Demir, M, Uslu-Beşli, L, Yeyin, N & Sönmezoğlu, K 2018, 'Blood clearance and occupational exposure for ¹⁷⁷Lu-DOTATATE compared to ¹⁷⁷Lu-PSMA radionuclide therapy', *Radiation and Environmental Biophysics*, vol. 57, no. 1, Mar 2018

2020-04-02, pp. 55-61.

ARPANSA 2019, *Code for the Safe Transport of Radioactive Material* Rev. 1, vol. Radiation Protection Series C-2

Bailey, DL, Hennessy, TM, Willowson, KP, Henry, EC, Chan, DL, Aslani, A & Roach, PJ 2015a, 'In vivo quantification of ^sup 177^Lu with planar whole-body and SPECT/CT gamma camera imaging', *EJNMMI Physics*, vol. 2, no. 1, Sep 2015

2015-09-24, pp. 1-17.

Bailey, DL, Hennessy, TM, Willowson, KP, Henry, EC, Chan, DLH, Aslani, A & Roach, PJ 2015b, 'In vivo quantification of (177)Lu with planar whole-body and SPECT/CT gamma camera imaging', *EJNMMI Physics*, vol. 2, no. 1, p. 20.

Bailey, DL & Willowson, KP 2013, 'An evidence-based review of quantitative SPECT imaging and potential clinical applications', *The Journal of nuclear medicine (1978)*, vol. 54, no. 1, pp. 83-89.

Barna, S, Haug, AR, Hartenbach, M, Rasul, S, Grubmüller, B, Kramer, G & Blaickner, M 2020, 'Dose Calculations and Dose-Effect Relationships in 177Lu-PSMA I&T Radionuclide Therapy for Metastatic Castration-Resistant Prostate Cancer', *Clinical Nuclear Medicine*, vol. 45, no. 9, pp. 661-667.

Beauregard, J-M, Hofman, MS, Pereira, JM, Eu, P & Hicks, RJ 2011, 'Quantitative (177)Lu SPECT (QSPECT) imaging using a commercially available SPECT/CT system', *Cancer Imaging*, vol. 11, no. 1, 06/15

03/30/accepted, pp. 56-66.

Beykan, S, Dam, JS, Eberlein, U, Kaufmann, J, Kjærgaard, B, Jødal, L, Bouterfa, H, Bejot, R, Lassmann, M & Jensen, SB 2016, '177Lu-OPS201 targeting somatostatin receptors: in vivo biodistribution and dosimetry in a pig model', *EJNMMI Research*, vol. 6, no. 1, 2016/06/13, p. 50.

Biodex Medical Systems, I 2016, *ATOMLAB 500 DOSE CALIBRATOR OPERATION AND SERVICE MANUAL*, Biodex Medical Systems, Inc., 20 Ramsey Rd, Shirley, New York, 11967-4704.

Bodei, L, Kidd, M, Paganelli, G, Grana, CM, Drozdov, I, Cremonesi, M, Lepensky, C, Kwekkeboom, DJ, Baum, RP, Krenning, EP & Modlin, IM 2014, 'Long-term tolerability of PRRT in 807 patients with neuroendocrine tumours: the value and limitations of clinical factors', *European Journal of Nuclear Medicine and Molecular Imaging*, vol. 42, no. 1, pp. 5-19.

Braat, AJAT, Snijders, TJ, Seute, T & Vonken, EPA 2019, 'Will 177Lu-DOTATATE Treatment Become More Effective in Salvage Meningioma Patients, When Boosting Somatostatin Receptor Saturation? A Promising Case on Intra-arterial Administration', *Cardiovascular and interventional radiology*, vol. 42, no. 11, pp. 1649-1652.

Bushberg, JT 2012, *The essential physics of medical imaging*, 3rd ed. edn, Wolters Kluwer/Lippincott Williams & Wilkins, Philadelphia.

CanadianCancerTrialGroup 2022, *RECIST. The Official Site of the RECIST Working Group*, viewed 24th June 2022, <https://recist.eortc.org/>.

CancerCouncilAustralia 2020, *Understanding Prostate Cancer*, Cancer Council Australia, Level 14, 477 Pitt Street, Sydney NSW 2000, <https://www.cancer.org.au/assets/pdf/understanding-prostate-cancer-booklet>.

Celler, A, Piwowarska-Bilska, H, Shcherbinin, S, Uribe, C, Mikolajczak, R & Birkenfeld, B 2014, 'Evaluation of dead-time corrections for post-radionuclide-therapy (177)Lu quantitative imaging with low-energy high-resolution collimators', *Nucl Med Commun*, vol. 35.

Cherry, SR, Sorenson, J, Phelps, ME & Methe, BM 2004, *Physics in nuclear medicine*, Elsevier Saunders, Philadelphia.

Cremonesi, M, Ferrari, M, Bodei, L, Tosi, G & Paganelli, G 2006, 'Dosimetry in Peptide Radionuclide Receptor Therapy: A Review', *The Journal of nuclear medicine (1978)*, vol. 47, no. 9, pp. 1467-1475.

D'Arienzo, M, Cozzella, ML, Fazio, A, De Felice, P, Iaccarino, G, D'Andrea, M, Ungania, S, Cazzato, M, Schmidt, K, Kimiaei, S & Strigari, L 2016, 'Quantitative 177Lu SPECT imaging using advanced correction algorithms in non-reference geometry', *Physica Medica*, vol. 32, no. 12, pp. 1745-1752.

Dash, A, Pillai, MRA & Knapp, FF 2015, 'Production of 177Lu for Targeted Radionuclide Therapy: Available Options', *Nuclear medicine and molecular imaging*, vol. 49, no. 2, pp. 85-107.

de Nijs, R, Lagerburg, V, Klausen, TL & Holm, S 2014, 'Improving quantitative dosimetry in 177Lu-DOTATATE SPECT by energy window-based scatter corrections', *Nucl Med Commun*, vol. 35.

Desy, A, Bouvet, GF, Frezza, A, Després, P & Beauregard, J-M 2020, 'Impact of dead time on quantitative 177Lu-SPECT (QSPECT) and kidney dosimetry during PRRT', *EJNMMI Physics*, vol. 7, no. 1, pp. 1-8.

Dewaraja, YK, Frey, EC, Sgouros, G, Brill, AB, Roberson, P, Zanzonico, PB & Ljungberg, M 2012, 'MIRD pamphlet No. 23: quantitative SPECT for patient-specific 3-dimensional dosimetry in internal radionuclide therapy', *The Journal of nuclear medicine (1978)*, vol. 53, no. 8, pp. 1310-1325.

Dhiantravan, N, Emmett, L, Joshua, AM, Pattison, DA, Francis, RJ, Williams, S, Sandhu, S, Davis, ID, Vela, I, Neha, N, Bressel, M, Murphy, DG, Hofman, MS & Azad, AA 2021, 'UpFrontPSMA: a randomized phase 2 study of sequential 177Lu-PSMA-617 and docetaxel vs docetaxel in metastatic hormone-naïve prostate cancer (clinical trial protocol)', *BJU international*, vol. 128, no. 3, pp. 331-342.

Ebbers, SC, Braat, AJAT, Moelker, A, Stokkel, MPM, Lam, MGEH & Barentsz, MW 2020, 'Intra-arterial versus standard intravenous administration of lutetium-177-DOTA-octreotate in patients with NET liver metastases: study protocol for a multicenter, randomized controlled trial (LUTIA trial)', *Trials*, vol. 21, no. 1, pp. 141-141.

Emmett, L, Subramaniam, S, Joshua, AM, Crumbaker, M, Martin, A, Zhang, AY, Rana, N, Langford, A, Mitchell, J, Yip, S, Francis, R, Hofman, MS, Sandhu, S, Azad, A, Gedye, C, McJannett, M, Stockler, MR & Davis, ID 2021, 'ENZA-p trial protocol: a randomized phase II trial using prostate-specific membrane antigen as a therapeutic target and prognostic indicator in men with metastatic castration-resistant prostate cancer treated with enzalutamide (ANZUP 1901)', *BJU international*, vol. 128, no. 5, pp. 642-651.

Erlandsson, K, Buvat, I, Pretorius, PH, Thomas, BA & Hutton, BF 2012, 'A review of partial volume correction techniques for emission tomography and their applications in neurology, cardiology and oncology', *Physics in medicine & biology*, vol. 57, no. 21, pp. R119-R159.

Fernandez, R, Allen, S & Lewington, V 2015, 'Ensuring Safe & Effective Delivery of Lutetium-177 Dotatate Therapy', *J. Nucl. Med.*, vol. 56, no. 3.

Finocchiaro, D, Berenato, S, Grassi, E, Bertolini, V, Castellani, G, Lanconelli, N, Versari, A, Spezi, E, Iori, M & Fioroni, F 2019, 'Partial volume effect of SPECT images in PRRT with 177Lu labelled somatostatin analogues: A practical solution', *Physica Medica: European Journal of Medical Physics*, vol. 57, pp. 153-159.

Forrer, F, Krenning, EP, Kooij, PP, Bernard, BF, Konijnenberg, M, Bakker, WH, Teunissen, JJM, de Jong, M, van Lom, K, de Herder, WW & Kwekkeboom, DJ 2009, 'Bone marrow dosimetry in peptide receptor radionuclide therapy with [177Lu-DOTA0,Tyr3]octreotate', *European Journal of Nuclear Medicine and Molecular Imaging*, vol. 36, no. 7, 2009/02/27, p. 1138.

Frezza, A, Desport, C, Uribe, C, Zhao, W, Celler, A, Després, P & Jean-Mathieu, B 2020, 'Comprehensive SPECT/CT system characterization and calibration for ¹⁷⁷Lu quantitative SPECT (QSPECT) with dead-time correction', *EJNMMI Physics*, vol. 7, no. 1, Dec 2020

2020-02-14.

Garkavij, M, Nickel, M, Sjögreen-Gleisner, K, Ljungberg, M, Ohlsson, T, Wingårdh, K, Strand, SE & Tennvall, J 2010, '177Lu-[DOTA0,Tyr3] octreotate therapy in patients with disseminated neuroendocrine tumors: Analysis of dosimetry with impact on future therapeutic strategy', *Cancer*, vol. 116, no. S4, pp. 1084-1092.

GraphPad 2009, *Why does Prism report the standard errors (SE) of best-fit parameters, while some other programs report standard deviations?*, 2022, <https://www.graphpad.com/support/faq/why-does-prism-report-the-standard-errors-se-of-best-fit-parameters-while-some-other-programs-report-standard-deviations/#:~:text=Prism%20reports%20the%20standard%20error,and%20intercept%20of%20linear%20regression).&text=The%20SD%20tells%20you%20about,you%20have%20determined%20the%20mean.>.

GraphPad 2015, *Standard deviation of the residuals*, 2022, <https://www.graphpad.com/guides/prism/latest/curve-fitting/reg_standard_deviation_of_the_resi.htm>.

GraphPad 2017, *Nonlinear regression when you entered error values directly*, 2022, <https://www.graphpad.com/support/faqid/2038/>.

GraphPad 2022a, *Confidence and prediction bands (linear regression)*, 2022, <https://www.graphpad.com/guides/prism/latest/curve-fitting/reg_confidence_and_prediction_linear.htm>.

GraphPad 2022b, *Runs test following linear regression*, Graphpad, 2022, <https://www.graphpad.com/guides/prism/latest/curve-fitting/runstestfollowinglinearregression.htm?q=runs>.

Gupta, SK, Singla, S, Thakral, P & Bal, C 2013, 'Dosimetric Analyses of Kidneys, Liver, Spleen, Pituitary Gland, and Neuroendocrine Tumors of Patients Treated With 177Lu-DOTATATE', *Clinical Nuclear Medicine*, vol. 38, no. 3, pp. 188-194.

Hippeläinen, E, Tenhunen, M, Mäenpää, H & Sohlberg, A 2016, 'Quantitative accuracy of 177Lu SPECT reconstruction using different compensation methods: phantom and patient studies', *EJNMMI Research*, vol. 6, no. 1.

Hofman, MS, Emmett, L, Violet, J, Y. Zhang, A, Lawrence, NJ, Stockler, M, Francis, RJ, Iravani, A, Williams, S, Azad, A, Martin, A, McJannett, M & Davis, ID 2019, 'TheraP: a randomized phase 2 trial of 177Lu-PSMA-617 theranostic treatment vs cabazitaxel in progressive metastatic castration-resistant prostate cancer (Clinical Trial Protocol ANZUP 1603)', *BJU international*, vol. 124, no. S1, pp. 5-13.

Iaea & Bailey, DL 2015, *Nuclear Medicine Physics : A Handbook for Teachers and Students*, Vienna: IAEA, Vienna.

Imaxeon 2017, *NEMA IEC PET Body Phantom Set*, Imaxeon, viewed 9th September 2020, <https://www.imaxeon.com.au/en/products/molecular-imaging/nuclear-medicine-and-pet-equipment/quality-assurance-phantoms/nema-iec-pet-body-phantom-set/>.

Johannes, T-G & Michael, L 2018, 'Optimizing Image Quantification for ^sup 177^Lu SPECT/CT Based on a 3D Printed 2-Compartment Kidney Phantom', *The Journal of nuclear medicine (1978)*, vol. 59, no. 4, p. 616.

King, M & Farncombe, T 2003, 'An overview of attenuation and scatter correction of planar and SPECT data for dosimetry studies', *Cancer biotherapy & radiopharmaceuticals*, vol. 18, no. 2, pp. 181-190.

Kirkup, L 2019, *Experimental methods for science and engineering students : an introduction to the analysis and presentation of data*, Second edition. edn, Cambridge University Press, Cambridge.

Kratochwil, C, Giesel, FL, Eder, M, Afshar-Oromieh, A, Benešová, M, Mier, W, Kopka, K & Haberkorn, U 2015, '[177Lu]Lutetium-labelled PSMA ligand-induced remission in a patient with metastatic prostate cancer', *European Journal of Nuclear Medicine and Molecular Imaging*, vol. 42, no. 6, pp. 987-988.

Kwekkeboom, DJ, Bakker, WH, Kooij, PP, Konijnenberg, MW, Srinivasan, A, Erion, JL, Schmidt, MA, Bugaj, JL, de Jong, M & Krenning, EP 2001, '[177Lu-DOTA0,Tyr3]octreotate: comparison with [111In-DTPA0]octreotide in patients', *European Journal of Nuclear Medicine*, vol. 28, no. 9, pp. 1319-1325.

Kwekkeboom, DJ, de Herder, WW & van Eijck, CHJ 2010, 'Peptide receptor radionuclide therapy in patients with gastroenteropancreatic neuroendocrine tumors', *Semin Nucl Med*, vol. 40.

Larsson, M, Bernhardt, P, Svensson, JB, Wängberg, B, Ahlman, H & Forssell-Aronsson, E 2012, 'Estimation of absorbed dose to the kidneys in patients after treatment with 177Lu-octreotate: comparison between methods based on planar scintigraphy', *EJNMMI Research*, vol. 2, no. 1, pp. 1-13.

Levart, D, Kalogianni, E, Corcoran, B, Mulholland, N & Vivian, G 2019, 'Radiation precautions for inpatient and outpatient 177Lu-DOTATATE peptide receptor radionuclide therapy of neuroendocrine tumours', *EJNMMI Physics*, vol. 6, no. 1, 2019/04/25, p. 7.

Ljungberg, M, Celler, A, Konijnenberg, MW, Eckerman, KF, Dewaraja, YK, Sjögreen-Gleisner, K, Bolch, WE, Brill, AB, Fahey, F, Fisher, DR, Hobbs, R, Howell, RW, Meredith, RF, Sgouros, G, Zanzonico, P, Bacher, K, Chiesa, C, Flux, G, Lassmann, M, Strigari, L & Walrand, S 2016, 'MIRD Pamphlet No. 26: Joint EANM/MIRD Guidelines for Quantitative 177Lu SPECT Applied for Dosimetry of Radiopharmaceutical Therapy', *The Journal of nuclear medicine (1978)*, vol. 57, no. 1, pp. 151-162.

Loser, A, Schwarzenbock, SM, Heuschkel, M, Willenberg, HS, Krause, BJ & Kurth, J 2018, 'Peptide receptor radionuclide therapy with 177Lu-DOTA-octreotate: dosimetry, nephrotoxicity, and the effect of hematological toxicity on survival.', *Nuclear medicine communications*, vol. 39, no. 3, pp. 236–246.

Mahidul Haque, P, Hasan, T, Fazlul, H & Zahid Hasan, M 2016, 'Study of the effect of energy window width and peak shift on SPECT images to evaluate false diagnosis', *Majallahī-i pizishk-i hastahī Īrān*, vol. 24, no. 2, p. 76.

Mair, C, Warwitz, B, Fink, K, Scarpa, L, Nilica, B, Maffey-Steffan, J, Buxbaum, S & Virgolini, IJ 2018, 'Radiation exposure after 177Lu-DOTATATE and 177Lu-PSMA-617 therapy', *Annals of Nuclear Medicine*, vol. 32, no. 7, 2018/08/01, pp. 499-502.

Marin, G, Vanderlinden, B, Karfis, I, Guiot, T, Wimana, Z, Flamen, P & Vandenberghe, S 2017, 'Accuracy and precision assessment for activity quantification in individualized dosimetry of ^sup 177^Lu-DOTATATE therapy', *EJNMMI Physics*, vol. 4, no. 1, Jan 2017

2017-10-30, pp. 1-15.

Mettler, FA & Guiberteau, MJ 2012, *Essentials of nuclear medicine imaging*, 6th ed. edn, Elsevier/Saunders, Philadelphia, Penn.

Nelson, A, Mirando, D, Nilman, R 2020, 'Dosimetry for Targeted Molecular Radiotherapy', *MIM White Paper*.

Nelson, KS, MA 2019, 'Radiation Safety Observations Associated with 177Lu Dotatate Patients.', *Health Physics*, vol. 177, no. 6, pp. 680–687.

Ogawa, K, Harata, Y, Ichihara, T, Kubo, A & Hashimoto, S 1991, 'A practical method for position-dependent Compton-scatter correction in single photon emission CT', *IEEE transactions on medical imaging*, vol. 10, no. 3, pp. 408-412.

Ozkan, A, Ucar, B, Seymen, H, Yildiz Yarar, Y, Falay, FO & Demirkol, MO 2020, 'Posttherapeutic Critical Organ Dosimetry of Extensive 177Lu-PSMA Inhibitor Therapy With Metastatic Castration-

Resistant Prostate Cancer: One Center Results', *Clinical Nuclear Medicine*, vol. 45, no. 4, pp. 288-291.

Peters, SMB, Meyer Viol, SL, van der Werf, NR, de Jong, N, van Velden, FHP, Meeuwis, A, Konijnenberg, MW, Gotthardt, M, de Jong, HWAM & Segbers, M 2020, 'Variability in lutetium-177 SPECT quantification between different state-of-the-art SPECT/CT systems', *EJNMMI Physics*, vol. 7, no. 1, 2020/02/11, p. 9.

Prism, G 1986, *Tests for Normal Distribution*, GraphPad Prism, 2022, <https://www.graphpad.com/guides/prism/latest/statistics/stat_choosing_a_normality_test.htm>.

Prism, G 2022, *Wilcoxon matched pairs test*, GraphPad Prism, 2022, <https://www.graphpad.com/guides/prism/latest/statistics/stat_how_to_do_an_unpaired_t_test_w_3_2.htm>.

Raharja, C, Sun, E, Gabrys, J & Wong, R 2018, 'Assessing Dose Administration of Lu-177 DOTATATE Therapy: Quantifying the Residual Dose', *Journal of Medical Imaging and Radiation Sciences*, vol. 49, no. 2, pp. 4-5.

Ramonaheng, K, van Staden, JA & du Raan, H 2021, 'The effect of calibration factors and recovery coefficients on 177Lu SPECT activity quantification accuracy: a Monte Carlo study', *EJNMMI Physics*, vol. 8, no. 1, pp. 27-27.

S.E. International, I 2019, *Instrument Geometry and Detection Efficiency: 2π vs. 4π*, S.E. International, Inc., S.E. International, Inc. P.O. Box 39, 436 Farm Rd. Summertown, TN 38483 1.931.964.3561 viewed 05/12/2019 2019, <https://seintl.com/instrument-geometry-and-detection-efficiency-2%CF%80-vs-4%CF%80/>.

Sanders, JC, Kuwert, T, Hornegger, J & Ritt, P 2014, 'Quantitative SPECT/CT Imaging of 177Lu with In Vivo Validation in Patients Undergoing Peptide Receptor Radionuclide Therapy', *Molecular imaging and biology*, vol. 17, no. 4, pp. 585-593.

Sandstrom, M, Garske-Roman, U, Granberg, D, Johansson, S, Widstrom, C, Eriksson, B, Sundin, A, Lundqvist, H & Lubberink, M 2013, 'Individualized Dosimetry of Kidney and Bone Marrow in Patients Undergoing Lu-177-DOTA-Octreotate Treatment', *The Journal of nuclear medicine (1978)*, vol. 54, no. 1, pp. 33-41.

Siemens 2016, *xSPECT Technology and Broad Quantification Technology Specifications*, Siemens Healthcare GmbH, Henkestr. 127, 91052 Erlangen, Germany.

Siemens 2019, '*xSPECT Quant Reliable SPECT/CT quantification for clinical routine*'.

Silva, CBdO, Ongaratti, BR, Trott, G, Haag, T, Ferreira, NP, Leães, CGS, Pereira-Lima, JFS & Oliveira, MdC 2015, 'Expression of somatostatin receptors (SSTR1-SSTR5) in meningiomas and its

clinicopathological significance', *International journal of clinical and experimental pathology*, vol. 8, no. 10, pp. 13185-13192.

Siman, W, Silosky, M & Kappadath, SC 2015, 'Arevised monitor source method for practical deadtime count loss compensation in clinical planar and spect studies', *Physics in medicine and biology*, vol. 60, no. 3, pp. 1199-1216.

Talukdar, M, Dewhirst, H & Paulsen, A 2019, 'Assaying Lutetium 177 in a Dose Calibrator', *The Journal of nuclear medicine (1978)*, vol. 60.

Uribe, CF 2016, 'SPECT/CT Quantification of 177Lu for Dosimetry in Radionuclide Therapy Treatments of Neuroendocrine Tumors', The Faculty of Graduate and Postdoctoral Studies (Physics), Doctorate of Philosophy thesis, The University of British Columbia

Uribe, CF, Esquinas, PL, Gonzalez, M & Celler, A 2016, 'Characteristics of Bremsstrahlung emissions of ¹⁷⁷Lu, ¹⁸⁸Re, and ⁹⁰Y for SPECT/CT quantification in radionuclide therapy', *Physica Medica: European Journal of Medical Physics*, vol. 32, no. 5, pp. 691-700.

Uribe, CF, Esquinas, PL, Gonzalez, M, Zhao, W, Tanguay, J & Celler, A 2018, 'Deadtime effects in quantification of 177 Lu activity for radionuclide therapy', *EJNMMI Physics*, vol. 5, no. 1, pp. 1-16.

Uribe, CF, Esquinas, PL & Tanguay, J 2017, 'Accuracy of 177Lu activity quantification in SPECT imaging: a phantom study', *EJNMMI Phys*, vol. 4.

Vija, A 2015, *Introduction to xSPECT* Technology: Evolving Multi-modal SPECT to Become Context-based and Quantitative White Paper*, White Paper, Siemens Healthcare GmbH, Henkestraße 127, 91052 Erlangen, Germany.

Vija, A, Von Gall, C & Ghosh, P 2018, 'Accurate, Reproducible, and Standardized Quantification', Siemens Medical Solutions USA, Inc. 40 Liberty Boulevard Malvern, PA 19355-9998.

Wehrmann, C, Senftleben, S, Zachert, C, Müller, D & Baum, RP 2007, 'Results of individual patient dosimetry in peptide receptor radionuclide therapy with 177Lu DOTA-TATE and 177Lu DOTA-NOC', *Cancer biotherapy & radiopharmaceuticals*, vol. 22, no. 3, pp. 406-416.

Willowson, K, Bailey, DL, Bailey, EA, Baldock, C & Roach, PJ 2010, 'In vivo validation of quantitative SPECT in the heart', *Clinical physiology and functional imaging*, vol. 30, no. 3, pp. 214-219.

Willowson, K, Bailey, DL & Baldock, C 2008, 'Quantitative SPECT reconstruction using CT-derived corrections', *Physics in medicine & biology*, vol. 53, no. 12, pp. 3099-3112.

Zhao, W, Esquinas, PL, Hou, X, Uribe, CF, Gonzalez, M, Beauregard, J-M, Dewaraja, YK & Celler, A 2018, 'Determination of gamma camera calibration factors for quantitation of therapeutic radioisotopes', *EJNMMI Physics*, vol. 5, no. 1, 2018/05/02, p. 8.